SEARCH AND DISCOVERY:
HIGH THROUGHPUT METHODS FOR FUEL CELL MATERIALS

A Dissertation

Presented to the Faculty of the Graduate School

of Cornell University

In Partial Fulfillment of the Requirements for the Degree of

Doctor of Philosophy

By

Abigail Rose Van Wassen

August 2016

SEARCH AND DISCOVERY:
HIGH THROUGHPUT METHODS FOR FUEL CELL MATERIALS

Abigail Rose Van Wassen, Ph. D.

Cornell University 2016

As global energy consumption has increased, there is an increasing demand for renewable energy solutions. Fuel cells represent an attractive and promising alternative, though some problems preventing their widespread implementation persist. Of particular importance are catalysts for the oxygen reduction reaction (ORR). Pt, the standard catalyst, is expensive and inefficient, leading to a high cost and loss in performance.

In order to address these issues, new lower-cost, durable, and high-performance materials are required. My work has focused on the use of sputter deposition methods to generate compositionally-graded thin films to screen compositions for both catalyst supports and for the ORR catalysts themselves. I employ a custom-built sputter deposition chamber for the generation of these composition spreads. For catalyst support libraries, I reactively co-sputter three transition metals along with N_2 to form ternary nitride spreads. A modified electrochemical cell was employed to non-destructively test the electrochemistry of different compositions in these libraries. Initial findings indicate that a Ti-rich composition of TaTiAl-N may be favorable as a catalyst support material.

Sputter-deposition can also be used to screen ORR catalysts by depositing

films on glassy carbon electrodes that can be subsequently used in a rotating disk electrode (RDE) setup to obtain mechanistic and kinetic information. For this work, I have screened binary metal compositions that contained combinations of Pd, Au, Ag, Cu, and Rh, and selected the most promising one-$Pd_{1-x}Cu_x$ for further study. There were several catalytically relevant compositions, notably alloyed $Pd_{0.5}Cu_{0.5}$ and $Pd_{0.1}Cu_{0.9}$.

BIOGRAPHICAL SKETCH

Abigail was interested in science from a very young age, when she wanted to be a geologist or a paleontologist or an astronaut. Her interest in chemistry, specifically, began in high school, when she took tenth grade and AP Chemistry. Her experiences, particularly in AP Chemistry, inspired her to take Honors General Chemistry when she began her undergraduate studies at Kenyon College in September of 2007. Her experiences in this class, particularly the professor, Dr. Simon Garcia (a fellow Cornell alumnus), inspired her to join the lab of Dr. Scott Cummings in the chemistry department in the spring of 2008. She would work in his lab on the photochemistry of $[Pt(terpy)X]^-$ complexes for five semesters. Her final summer and academic year at Kenyon, she joined the Garcia lab to work on modifying the growth of ZnO crystals using organic diacids. She graduated in May of 2011.

Although her undergraduate research topics varied, the unifying themes of her work involved the use of metals and a strong emphasis on instrumentation, both with the motivation for renewable energy systems. After beginning graduate school at Cornell, Abigail joined the research group of Héctor Abruña in the Chemistry and Chemical Biology Department, to continue to pursue her interests in renewable energy, metals, and instrumentation. As her research project developed, she joined the group of Bruce van Dover in the Materials Science and Engineering department, where she got to use even more exotic metals, and even more complicated instruments.

After she graduates, Abigail will be starting a job at ExxonMobil in Paulsboro, New Jersey, where she will be working on passenger vehicle lubricants.

To my parents, for giving me the confidence to pursue whatever path I wanted

ACKNOWLEDGMENTS

The amount of work that goes into a Ph.D. could never be accomplished by just one person, and the work on project that is as collaborative as mine has been took practically a whole village.

First and foremost, I need to thank both of my advisors, Héctor Abruña and Bruce van Dover. Prof. Abruña's trust in me and my work gave me the confidence to try unusual projects and helped me to grow as a scientist, challenging me sometimes and building me up others. Prof. van Dover was always available to help me, whether it was with troubleshooting (one of many) problems with Tubby, or with interpreting an unusual piece of data. His calm demeanor and positive attitude always cheered me on, even when I was frustrated or demoralized. Without the support and guidance of both of my advisors, I would not have made it through graduate school. Prof. Frank DiSalvo, who also served on my committee, and was always happy to sit down with me and discuss problems that I was having in my research.

I also need to thank the graduate students and postdocs that served as mentors, namely Dr. David Finkelstein, Anna Legard, and Dr. Eric Rus. All three were integral in helping me establish myself in the electrochemistry and thin films worlds.

Ryo Wakabayashi has helped me with giving me sanity checks and by having informed, intelligent discussions on my research. It is because of his work that the combi project has gone through a full cycle of screening and synthesis of nanoparticles. My REU student, Andrés Molina-Villarino was also a huge help. Marc Murphy helped with some of the physical characterization and helped with problems I

struggled with when fixing Tubby. Dr. James McKone gave me both helpful science advice and life advice.

Many other people have contributed to my work or have supported me over the years: Dr. Nicole Ritzert, Dr. James O'Dea, Dr. Raymond Burns, Dr. Maura Weathers, Dr. Jonathon Shu, Suzanne Koehl, Kelly Case, Dr. Thiago Almeida, Dr. María Encarnación Lorenzo.

My friends, both in the lab and out, have kept me grounded: James Pastore, Rebecca Potash, Katie Silberstein, Xinran Feng, Emily Perregaux, Erin Stephens, Jenny Valentine, and the friends I've made at the Finger Lakes Cancer Resource Center.

Finally, my parents, the rest of my family, and Linxiao Chen have been my biggest supporters in graduate school, and I couldn't have made it through without them.

TABLE OF CONTENTS

LIST OF FIGURES

LIST OF TABLES

CHAPTER 1

INTRODUCTION

1.1 Introduction to Fuel Cells

As the world's energy needs continue to increase and the average global temperature continues to rise, there has been a large effort to mitigate the environmental effects of CO_2. Beyond the greater incorporation of renewable energy sources into our energy landscape, we have also striven to improve the efficiency of our transportation, with one of these ways being the use of electric vehicles. Although battery-powered and hybrid battery-internal combustion engine (ICE) vehicles have dominated the market, fuel cell-powered vehicles (FCV) are becoming more commercialized, with the 2016 release of the Toyota Mirai and the projected 2017 releases of both Mercedes-Benz's and Honda's fuel cell vehicles,[1,2] which offer a more similar driving experience to the traditional ICE-powered vehicles. This is because FCV have a higher range and the refueling times for a FCV are a few minutes, rather than the hours commonly required to recharge the battery in a battery-powered EV.

Fig. 1.1 shows a general schematic of a fuel cell. The white sections on the left and right represent the gas flow fields and the gas diffusion layers, where the reactant gases enter the fuel cell. The light grey strips to either side represent the catalysts and the catalyst support. On the left is the anode, where the hydrogen oxidation reaction occurs. On the right, we find the cathode, where the oxygen reduction reaction (ORR) is carried out. In the center is the membrane that separates them. This general

schematic is true for most fuel cell types, and will be true for all those discussed in this dissertation.

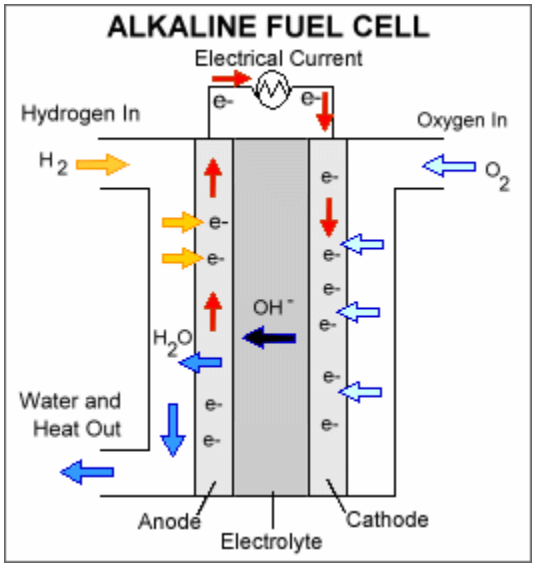

Figure 1.1. A diagram of an alkaline H_2/O_2 fuel cell. [3]

Despite their poor market penetration, fuel cells have existed in some form since the 1830s.[3] Although many designs and systems were explored by many different people, the first "modern" fuel cell was engineered by Francis Bacon in 1959.[3,4] The "Bacon cell" differed from many of its predecessors by using an alkaline system instead of an acidic one. He also modified the electrode, adding an impermeable polymer to prevent gas from leaking from one electrode to the other, where it could also react. The Bacon cell was also run at high temperatures (200 °C), high pressures (20-40 bar), and KOH concentration (37-50%). [3,4]

Early alkaline fuel cell (AFC) catalyst materials were based on non-platinum metals, such as Ag and Ni.[3,5–8] AFCs similar to the Bacon cell, though with even higher alkalinity (85% KOH) and lower gas pressure, were used on the Apollo space

missions. Eventually, improvements in engineering allowed for the alkalinity to be decreased to 35% KOH, which was also immobilized in a matrix. These fuel cells, however, contained a considerable amount of Pt in the catalysts.[3] Early AFC had problems, particularly with the formation of K_2CO_3 precipitates resulting from CO_2 in the cell. The K_2CO_3 precipitates lowered the effective OH^- concentration in the cell, which had a detrimental effect on the catalysis. Their formation could also negatively impact the structure of the fuel cell.[3,9]

The development of Nafion in the late 1970s, enabled a new type of fuel cell: proton-exchange membrane fuel cells (PEMFC). [10–12] Upon hydration, the Nafion membrane had bound sulfonate groups and mobile H^+ that could act as an electrolyte in lieu of acid, but was still solid enough to prevent the reactant gases from mixing.[3] Moving to these acidic conditions meant that the operating temperature of the fuel cell had to be lowered to prevent degradation of Nafion, but also decreased the overpotential at the anode.[3,13]

Unfortunately, oxidizing acidic conditions meant that less-noble metals such as Ag and Ni, previously used for the earlier alkaline fuel cells, were not stable and therefore could not be used as electrocatalysts. [14] Pt and Pt alloys have been used in both the anode and cathode of PEMFCs because they can withstand the harsh conditions—particularly at the cathode—and catalyze both reactions. Despite Pt's catalytic activity, however, it still has a high overpotential for catalyzing the ORR. Not only are the ORR's kinetics slower in acidic medium, but the cost of Pt is also very high, hovering around$1000/troy oz at the time of this writing (or around $32/g). Both the Pt in a fuel cell and the expensive Nafion membrane increase the cost of the fuel

cell, although the economies of scale favor the cost of the membrane rather than the catalyst (figure below): at 500,000 units a year, the catalyst accounts for 45% of the

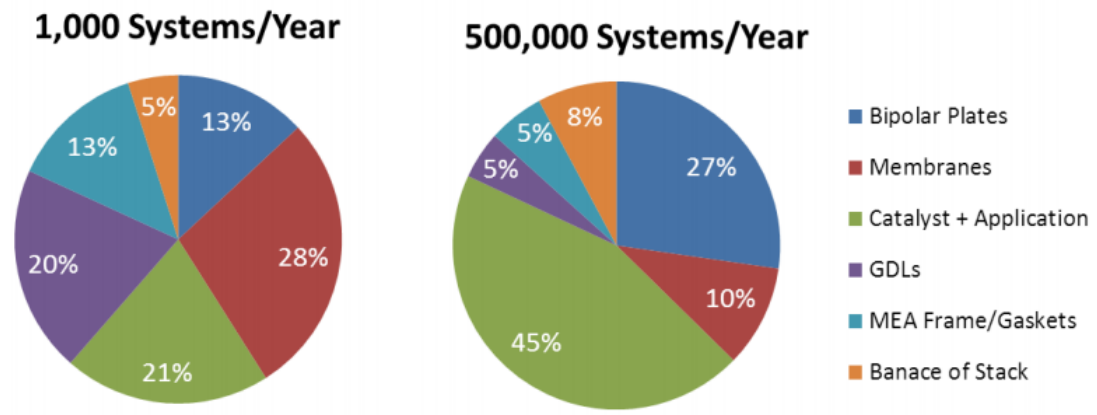

Figure 1.2. The cost breakdown of small-scale (left) vs mass-produced (right) fuel cell stacks. [15]

cost of the entire fuel cell, 4.5 times higher than the membrane.[15] The full cost breakdown can be found in Fig. 1.2.

A common approach to lower costs is to decrease the amount of Pt in a fuel cell. One way is to disperse Pt catalysts on a conductive carbon black support, to maximize the exposed surface area of the Pt (as only the surface of the nanoparticles is catalytic). Despite their use as a cost-saving measure, the degradation or ageing of Pt catalysts is actually exacerbated by the oxidation of the carbon black catalyst supports to CO_2, a reaction that is catalyzed by the Pt catalysts themselves. The oxidation of the carbon black leads to agglomeration (sintering) of the catalysts, resulting in a loss of Pt surface area (and then performance)as the particles agglomerate.[16]

Despite the advantages that PEMFC present, with the use of less corrosive conditions and the ability to achieve high current densities, the cost of Pt catalysts still

represents a major limitation to the widespread deployment of fuel cells. Until recently, the performance of alkaline anion exchange membranes (AEM) was limited. Recently, several promising candidates have been developed by the Coates group at Cornell, using different cation-functionalized (ammonium, imidazolium, phosphonium) polyethylene backbones.[17–19] Although the conductivity of these membranes was lower than that of Nafion—as high as 65mS/cm at best for the ammonium-functionalized polymer—it was still sufficient for fuel cell applications.[17,20] These AEM's had other benefits, including being easily solvent processable, being soluble in *n*-propanol. Not only were the AEM's solvent-processable, but the imidazolium-functionalized AEM showed excellent long-term stability under alkaline conditions.[19]

Because of the development of these better AEMs, AFCs have become an area of greater interest, though now in the form of anion-exchange membrane fuel cells (AEMFC). AEMFC have some advantages over PEMFC. Similar to the original AFC, their conditions are less oxidizing to metals. As a result, less noble metals—like the original Ag and Ni—could be used as cathodes in an AEMFC. AEMFCs also have fewer issues with electro-osmotic gradients and water management when compared to PEMFCs, where water causes fuel crossover, decreasing the fuel cell voltage.

1.2 Introduction to Oxygen Reduction Catalysts

Although both reactions in a fuel cell could be improved, the ORR has been especially problematic because of its slow reaction kinetics and resulting high overpotentials, which could reach 300 mV or more, or about 25% of the theoretical

1.23 V for a H_2/O_2 fuel cell. Beyond the overpotential, the ORR has two possible reaction pathways, shown below for alkaline reaction conditions:

$$O_2 + 2\ H_2O + 4\ e^- \rightarrow 4\ OH^- \quad (1)$$

$$O_2 + H_2O + 2e^- \rightarrow HO_2^- + OH^- \quad (2)$$

Ideally, the reaction shown in (1) (also known as the $4e^-$, or the direct mechanism) would occur, as it consumes the greatest number of electrons—making it more efficient. The reaction shown in (2), known as the series mechanism or the $2e^-$ mechanism, also produces the highly oxidizing species HO_2^- (or H_2O_2 in acidic medium), which can degrade the membrane in the fuel cell, leading to a decline of fuel cell performance.

When considering possible oxygen reduction catalysts, there are several figures of merit to be examined. The first is the E_{onset}, defined for the purposes of this thesis as the potential where the current reaches 10% of the maximum: in other words, near the potential where the reaction first begins to occur electrochemically. A 10% threshold ensured that background or double-layer currents were not dominant. To maximize the voltage of a fuel cell, for the ORR, the E_{onset} should be as positive as possible, meaning smaller overpotentials.

The second criterion involves the catalysis reaction mechanism. As mentioned above, for fuel cell purposes, direct mechanism (or $4\text{-}e^-$) catalysts are desired because they preclude the generation of deleterious products, and although reduction catalysts that generate HO_2^-/H_2O_2 may be desired for other industrial applications, it was not the focus of the work presented here.

The third metric is cost, which has driven much of the current work on oxygen reduction catalysts. Because of the high cost of Pt, much work has sought to increase the surface-area to volume ratio of the nanoparticle catalysts, because only Pt atoms on the surface of catalyst particles would be active in catalyzing the reactions. This can be done by making alloyed nanoparticles, where one of the metals is less noble (as well as considerably less expensive), and leaching out that less noble metal to leave behind a Pt skin with a higher surface area, and perhaps a strained lattice that can affect catalysis. This approach has been taken by many different researchers.[21–24]A similar but different tactic has been to use core-shell nanoparticles, where the core is either a Pt-alloy or a less-noble metal, with a Pt skin.[25–27] The interior of the nanoparticle had very little or no effect on the catalytic activity, but the exterior skin did, so active material was used there. This allowed for a drastic decrease in the amount of Pt used.

Beyond surface area arguments, researchers have tried to exploit electronic properties of catalysts, by the judicious choice of the metal alloyed with Pt, typically with one of two objectives. One is that the second metal can affect the d-band center of Pt.[28,29] The d-band center can affect the orbital overlap of the metal and the reactant O_2, modulating the binding strength. The catalytic activity depends on the binding strength of the O_2 molecules to the surface, and the presence of an alloying metal could enable a bi-functional catalyst mechanism.[30–32] Catalysts that bind O_2 too strongly would not let it desorb, which is important for certain steps of the ORR.[9,33] Conversely, catalysts that did not bind O_2 strongly enough could be poor catalysts because the O_2 did not remain on the surface long enough to react.

These approaches have largely been used for alkaline systems as well: high surface-area Pt-binary nanoparticles have been the focus of a great deal of the alkaline ORR literature.[34] Additionally, there have been "Pt-free" catalysts involving the use of some of the original metals used in AFC discussed above (Ag in particular).[35–38] Carbon-based catalysts have also been used as potential alkaline ORR catalysts because of the less-oxidizing alkaline conditions. Many of these materials included N-doped carbons ,[39,40] graphene or carbon nanotubes,[41,42] and metal-porphyrin-based catalysts.[43–45] Although these approaches had their merits, many of the carbon- and hetero-atom-based catalysts likely had metal impurities that contributed to their catalysis, as well as primarily generated HO_2^-.[46]

1.3 High-Throughput Methods to Study Electrocatalysts

Because the factors influencing ORR activity are difficult to predict, and the number of alkaline-stable metals is so large, it was valuable to have a way to generate and test catalyst compositions quickly. So-called "high-throughput" or combinatorial methods were useful for this, and have been used in several different ways, from thin films to nanoparticles. Although not all the work described below has been used to search for ORR catalysts, many of the principles could be applied.

Physical vapor deposition (PVD) techniques, sputtering in particular, are useful methods to quickly generate many different catalyst compositions. Not only would a sputtered sample take considerably less time to deposit than a nanoparticle sample would to synthesize, but depending on the type and geometry of sputtering, a broad composition library could be generated at one time. This composition library

could be generated, by sequentially sputtering layers or by co-sputtering different materials. When sequentially sputtering layers, different materials are sputtered, one after another, typically in very thin layers, seen in Fig. 1.3a, and then annealed after to homogenize the sample with respect to its depth.[47,48] When co-sputtering materials, the sputtering guns need to be located at different angles from each other, such that they each generate a gradient (Fig. 1.3b) that leads to a mixed composition in the more central part of the film (Fig. 1.3b).[49,50]

Beyond PVD samples, other samples could be generated using different high-throughput methods. A popular approach for this was to do combinatorial inkjet printing to generate different compositions. This was done by depositing metal salts

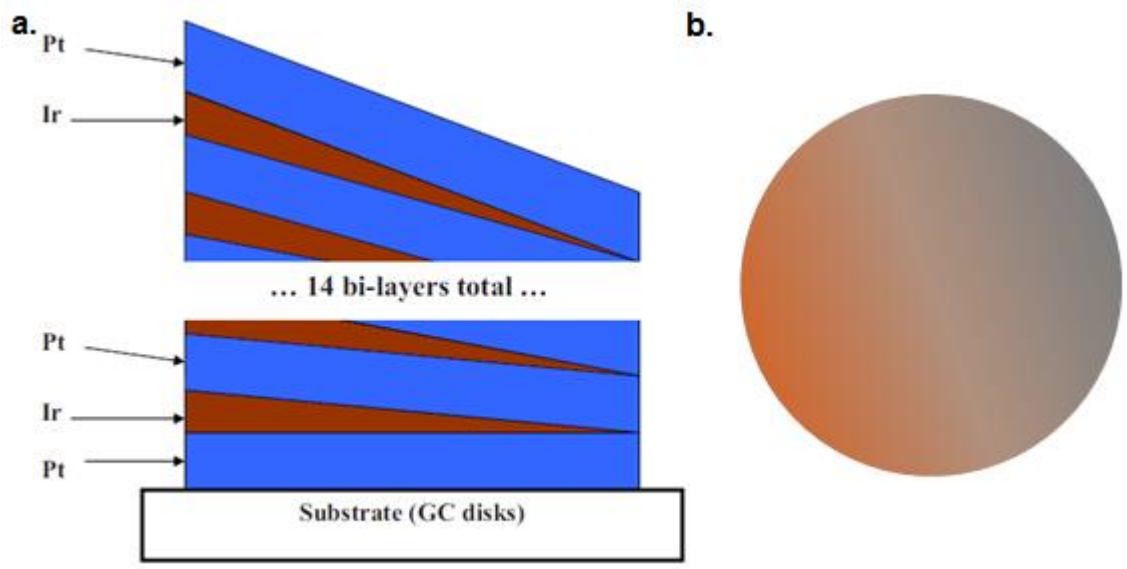

Figure 1.3. a.) The layered, sputtered approach taken by Dahn's group.[48] b.) the continuous gradient taken by van Dover's group.

and then reducing them using a reducing agent (varying from $NaBH_4$ to forming gas). This deposition was sometimes done using a literal printer,[51,52] or by pipetting the

amounts by hand[53] and varying the ratios of the salts involved. Both of these techniques yielded discrete spots with different compositions.

Because these compositions were intended to be used for electrochemical applications, they also needed to be able to be screened electrochemically in some way. Researchers have approached this problem in different ways, but they were generally broken down into two classes: indirect and direct probing of the electrochemistry or electrocatalytic activity. The direct and indirect methods each had their own advantages and disadvantages.

When indirectly probing the electrochemistry, there was generally an optical way to screen them, most commonly using a pH indicator, where there was either a color or fluorescence change. Under acidic conditions, the ORR consumed H^+ to produce H_2O, so there was a localized pH increase, and if an indicator was used with a pKa around that pH, then the fluorescence or color was either turned on or off with catalytic activity and could be mapped as a function of potential (functionally the E_{onset} as mentioned earlier).[52,54–56] As a result, this type of experiment was very easy to analyze, where brighter spots of fluorescence corresponded to greater catalytic activity. These methods have been extensively explored,[54] and are known to work best at near-neutral pH values. They have been used before in our group , but unfortunately, as Michele Tague discussed in her thesis, the number of pH indicators at alkaline pH's is very small—Acridine Orange and Naphthol AS, and both of those changed colors at relatively low alkalinity (maximum of pH 10).[57] Beyond that, no mechanistic information could be gained, so with our group's recent emphasis on

alkaline methods, I decided not to use an indirect method like our fluorescence assay to probe my oxygen reduction catalysts.

Direct methods are perhaps more challenging to develop in some ways, at least for certain systems. If samples are present as discrete compositions or spots, it is more straightforward, but determining how to analyze one composition electrochemically on a continuous composition gradient is more challenging. The wafer could be broken into pieces, but that destroyed the library as a whole. One solution to this, taken by the Dahn group, has been to use a mask during the sputtering process, which leaves individual spots, which can then be wire bonded (or connected electrically in some other way, such as soldering, etc) and connected to a special cell where the electrochemistry of each point can be monitored.[58] Similarly, Gregoire and coworkers used a scanning droplet cell on similar discrete compositions (ink jet-printed though, instead of sputtered) to essentially create a small electrochemical cell over each spot.[51]

For the oxygen reduction reaction, however, both of these techniques still made it difficult to get quantitative, mechanistic information. The Dahn group directly attacked this problem by using a more standard electrochemical technique for studying ORR catalysts: rotating disk electrode voltammetry (RDE).[21,48] By sputtering on inert glassy carbon electrodes, they were able to make discrete compositions but then gain mechanistic information by inserting the sputtered electrodes into an exchangeable RDE or rotating ring-disk electrode (RRDE) to electrochemically watch for the generation of H_2O_2.[48] This work has served as the inspiration for my ORR catalysis work, and will be discussed later in more depth in Chapters 5 and 6.

1.4 Summary of Chapter Contents

The following chapters will discuss much of the work that I have carried out during my time at Cornell. Chapter 2 discusses the experimental methods and methodologies I used in my work, both in terms of deposition of my thin films, and also a description of the electrochemical techniques I that employed to analyze them. Additionally, Chapter 2 also discussed the extensive modifications that I made to the sputter deposition chamber (known as "Tubby") that I used for generating thin films.

In Chapter 3, my work on catalyst supports is discussed. In particular, I screened quaternary metal nitrides for these purposes, with a special focus on Ta-Ti-Al-N. The electrochemical stability of Ta-Ti-Al-N was explored using electrochemical cycling in both H_2SO_4 and Nafion solutions. The MeOH oxidation activity of these films was explored, as well as the use of these films with a very thin Pt film. Additional nitride systems were also screened initially with conductive-probe AFM, and the results were compared with the electrochemistry results, to ascertain if any of those compositions would be interesting for future study.

The rest of my work dealt with ORR catalysts. Chapter 4 considers the oxygen reduction activity of different bulk, polycrystalline metals—specifically Pt, Au, Pd, and Ag—and systematically compares their activity under different pH conditions of 1, 13, and 14. Although Pt, unsurprisingly, displayed very "Nernstian" behavior—in other words, the potential scaled with the pH— some other metals had comparable if not faster reaction kinetics, showing that they may be more attractive options for alkaline ORR catalysts.

From the results in Chapter 4, I decided to explore combinations of these metals (with the omission of Pt) along with two others, to give a total of five metals: Au, Pd, Ag, Cu, and Rh. I deposited 1:1 ratios of each of these elements on a glassy carbon electrodes and explored their electrochemistry, looking for trends and tried to identify possible compositions for further study. A few looked particularly promising: PdAu, PdCu, and AgCu.

Using the electrochemistry data and other criteria including cost and feasibility of making nanoparticles of the material, PdCu was selected for further study. This work is presented in Chapter 6, which examines the relationship between the ratio of Pd to Cu and its effect on the catalytic activity over the composition space. Additionally, the surface composition and the Cu oxidation state of a few compositions were studied before and after electrochemical experimentation to help in the evaluation of the catalyst stability.

1.5 References

(1) Mercedes-Benz Developing Hydrogen Fuel Cell GLC For 2017 Release: Report http://www.techtimes.com/articles/125588/20160119/mercedes-benz-developing-hydrogen-fuel-cell-glc-for-2017-release-report.htm (accessed Apr 25, 2016).

(2) Muller, J. Honda's Alternative Trifecta: Clarity Will Be First Car To Offer Fuel Cell, Plug-In And Battery-Powered Versions http://www.forbes.com/sites/joannmuller/2016/04/21/honda-clarity-fuel-cell-will-add-plug-in-and-battery-powered-versions-in-2017/ (accessed Apr 25, 2016).

(3) Bagotsky, V. *Fuel Cells: Problems and Solutions*; John Wiley and Sons, Inc.: Hoboken, New Jersey, 2009.

(4) Bacon, F. T. *Ind. Eng. Chem.* **1960**, *52* (4), 301–303.

(5) Justi, E. Thermoelement, particularly for the electrothermic production of cold. US2685608 A, August 3, 1954.

(6) Wolf, V.; Eduard, J.; August, W. Process for using the decomposition energy of amalgams for electrolysis of metal salts by using reversible hydrogen electrodes. US3068157 A, December 11, 1962.

(7) Bagotzky, V. S.; Shumilova, N. A.; Samoilov, G. P.; Khrushcheva, E. I. *Electrochimica Acta* **1972**, *17* (9), 1625–1635.

(8) Shumilova, N. A.; Bagotzky, V. S. *Electrochimica Acta* **1968**, *13* (3), 285–293.

(9) Spendelow, J. S.; Wieckowski, A. *Phys. Chem. Chem. Phys.* **2007**, *9* (21), 2654.

(10) Yeo, R. S.; McBreen, J. *J. Electrochem. Soc.* **1979**, *126* (10), 1682–1687.

(11) Yeo, R. S. *J. Electrochem. Soc.* **1983**, *130* (3), 533–538.

(12) Hsu, W. Y.; Gierke, T. D. *J. Membr. Sci.* **1983**, *13* (3), 307–326.

(13) Sheng, W.; Gasteiger, H. A.; Shao-Horn, Y. *J. Electrochem. Soc.* **2010**, *157* (11), B1529–B1536.

(14) Pourbaix, M. *Atlas of Electrochemical Equilibria in Aqueous Solutions*, 2nd ed.; National Association of Corrosion Engineers: Houston, Texas, 1974.

(15) Marcinkoski, J.; Spendelow, J. S.; Wilson, A.; Papageorgopoulos, D. C. *Fuel Cell System Cost - 2015*; DOE Hydrogen and Fuel Cells Program Record 15015; 2015.

(16) Yu, Y.; Xin, H. L.; Hovden, R.; Wang, D.; Rus, E. D.; Mundy, J. A.; Muller, D. A.; Abruña, H. D. *Nano Lett.* **2012**, *12* (9), 4417–4423.

(17) Kostalik, H. A.; Clark, T. J.; Robertson, N. J.; Mutolo, P. F.; Longo, J. M.; Abruña, H. D.; Coates, G. W. *Macromolecules* **2010**, *43* (17), 7147–7150.

(18) Noonan, K. J. T.; Hugar, K. M.; Kostalik, H. A.; Lobkovsky, E. B.; Abruña, H. D.; Coates, G. W. *J. Am. Chem. Soc.* **2012**, *134* (44), 18161–18164.

(19) Hugar, K. M.; Kostalik, H. A.; Coates, G. W. *J. Am. Chem. Soc.* **2015**, *137* (27), 8730–8737.

(20) Sone, Y.; Ekdunge, P.; Simonsson, D. *J. Electrochem. Soc.* **1996**, *143* (4), 1254–1259.

(21) Liu, G. C. .; Stevens, D. A.; Burns, J. C.; Sanderson, R. J.; Vernstrom, G.; Atanasoski, R. T.; Debe, M. K.; Dahn, J. R. *J. Electrochem. Soc.* **2011**, *158*, B919.

(22) Yang, R.; Bian, W.; Strasser, P.; Toney, M. F. *J. Power Sources* **2013**, *222*, 169–176.

(23) Stevens, D. A.; Mehrotra, R.; Sanderson, R. J.; Vernstrom, G. D.; Atanasoski, R. T.; Debe, M. K.; Dahn, J. R. *J. Electrochem. Soc.* **2011**, *158*, B905.

(24) Wang, D.; Yu, Y.; Xin, H. L.; Hovden, R.; Ercius, P.; Mundy, J. A.; Chen, H.; Richard, J. H.; Muller, D. A.; DiSalvo, F. J.; Abruña, H. D. *Nano Lett.* **2012**, *12* (10), 5230–5238.

(25) Wang, D.; Xin, H. L.; Yu, Y.; Wang, H.; Rus, E.; Muller, D. A.; Abruña, H. D. *J Am Chem Soc* **2010**, *132* (50), 17664–17666.

(26) Yang, J.; Lee, J. Y.; Zhang, Q.; Zhou, W.; Liu, Z. *J. Electrochem. Soc.* **2008**, *155* (7), B776.

(27) Cai, J.; Zeng, Y.; Guo, Y. *J. Power Sources* **2014**, *270*, 257–261.

(28) Lima, F. H. B.; Zhang, J.; Shao, M. H.; Sasaki, K.; Vukmirovic, M. B.; Ticianelli, E. A.; Adzic, R. R. *J. Phys. Chem. C* **2007**, *111* (1), 404–410.

(29) Strasser, P.; Koh, S.; Anniyev, T.; Greeley, J.; More, K.; Yu, C.; Liu, Z.; Kaya, S.; Nordlund, D.; Ogasawara, H.; Toney, M. F.; Nilsson, A. *Nat. Chem.* **2010**, *2* (6), 454–460.

(30) Anderson, A. B.; Roques, J.; Mukerjee, S.; Murthi, V. S.; Markovic, N. M.; Stamenkovic, V. *J. Phys. Chem. B* **2005**, *109* (3), 1198–1203.

(31) Stamenkovic, V. R.; Mun, B. S.; Arenz, M.; Mayrhofer, K. J. J.; Lucas, C. A.; Wang, G.; Ross, P. N.; Markovic, N. M. *Nat. Mater.* **2007**, *6* (3), 241–247.

(32) Shao, M.; Liu, P.; Zhang, J.; Adzic, R. *J. Phys. Chem. B* **2007**, *111* (24), 6772–6775.

(33) Anastasijević, N. A.; Vesović, V.; Adžić, R. R. *J. Electroanal. Chem. Interfacial Electrochem.* **1987**, *229* (1–2), 305–316.

(34) Oezaslan, M.; Hasché, F.; Strasser, P. *J. Electrochem. Soc.* **2012**, *159* (4), B444–B454.

(35) Bidault, F.; Kucernak, A. *J. Power Sources* **2011**, *196* (11), 4950–4956.

(36) Liu, J.; Zhou, H.; Wang, Q.; Zeng, F.; Kuang, Y. *J. Mater. Sci.* **2011**, *47* (5), 2188–2194.

(37) Maheswari, S.; Sridhar, P.; Pitchumani, S. *Electrocatalysis* **2012**, *3* (1), 13–21.

(38) Ramaswamy, N.; Mukerjee, S. *ECS Trans.* **2010**, *33* (1), 1777–1785.

(39) Zhao, A.; Masa, J.; Muhler, M.; Schuhmann, W.; Xia, W. *Electrochimica Acta* **2013**, *98*, 139–145.

(40) Sa, Y. J.; Park, C.; Jeong, H. Y.; Park, S.-H.; Lee, Z.; Kim, K. T.; Park, G.-G.; Joo, S. H. *Angew. Chem. Int. Ed.* **2014**, *53* (16), 4102–4106.

(41) Ratso, S.; Kruusenberg, I.; Vikkisk, M.; Joost, U.; Shulga, E.; Kink, I.; Kallio, T.; Tammeveski, K. *Carbon* **2014**, *73*, 361–370.

(42) Vikkisk, M.; Kruusenberg, I.; Joost, U.; Shulga, E.; Kink, I.; Tammeveski, K. *Appl. Catal. B Environ.* **2014**, *147*, 369–376.

(43) Wu, G.; Zelenay, P. *Acc. Chem. Res.* **2013**, *46* (8), 1878–1889.

(44) Li, X.; Liu, G.; Popov, B. N. *J. Power Sources* **2010**, *195* (19), 6373–6378.

(45) Chung, H. T.; Won, J. H.; Zelenay, P. *Nat. Commun.* **2013**, *4*, 1922.

(46) Wang, L.; Ambrosi, A.; Pumera, M. *Angew. Chem. Int. Ed.* **2013**, *52* (51), 13818–13821.

(47) Bonakdarpour, A.; Löbel, R.; Atanasoski, R. T.; Vernstrom, G. D.; Schmoeckel, A. K.; Debe, M. K.; Dahn, J. R. *J. Electrochem. Soc.* **2006**, *153* (10), A1835.

(48) Liu, G. C.-K.; Sanderson, R. J.; Vernstrom, G.; Stevens, D. A.; Atanasoski, R. T.; Debe, M. K.; Dahn, J. R. *J. Electrochem. Soc.* **2010**, *157* (2), B207.

(49) Gregoire, J. M.; van Dover, R. B.; Jin, J.; DiSalvo, F. J.; Abruña, H. D. *Rev. Sci. Instrum.* **2007**, *78* (7), 072212–072212 – 6.

(50) Prochaska, M.; Jin, J.; Rochefort, D.; Zhuang, L.; DiSalvo, F. J.; Abruña, H. D.; van Dover, R. B. *Rev. Sci. Instrum.* **2006**, *77* (5), 054104–054104 – 8.

(51) Gregoire, J. M.; Xiang, C.; Mitrovic, S.; Liu, X.; Marcin, M.; Cornell, E. W.; Fan, J.; Jin, J. *J. Electrochem. Soc.* **2013**, *160* (4), F337–F342.

(52) Reddington, E.; Sapienza, A.; Gurau, B.; Viswanathan, R.; Sarangapani, S.; Smotkin, E. S.; Mallouk, T. E. *Science* **1998**, *280* (5370), 1735–1737.

(53) Almeida, T. S.; Van Wassen, A. R.; VanDover, R. B.; de Andrade, A. R.; Abruña, H. D. *J. Power Sources* **2015**, *284*, 623–630.

(54) Stöwe, K.; Dogan, C.; Welsch, F.; Maier, W. F. *Z. Für Phys. Chem.* **2013**, *227* (5), 561–593.

(55) Dogan, C.; Stöwe, K.; Maier, W. F. *ACS Comb. Sci.* **2015**, *17* (3), 164–175.

(56) Jin, J.; Prochaska, M.; Rochefort, D.; Kim, D. K.; Zhuang, L.; DiSalvo, F. J.; van Dover, R. B.; Abruña, H. D. *Appl. Surf. Sci.* **2007**, *254* (3), 653–661.

(57) Tague, M. E. A Combinatorial Approach for Exploring Fuel Cell Electrocatalysts, Cornell University, 2011.

(58) Fleischauer, M. D.; Hatchard, T. D.; Rockwell, G. P.; Topple, J. M.; Trussler, S.; Jericho, S. K.; Jericho, M. H.; Dahn, J. R. *J. Electrochem. Soc.* **2003**, *150* (11), A1465.

CHAPTER 2

METHODOLOGY AND EXPERIMENTAL SETUP

2.1 Sputtering

2.1.1 Features and Specifications of the Sputtering Chamber

In order to make thin film samples that could be used for combinatorial search experiments, a custom-built DC magnetron sputtering chamber ("Tubby"), which was optimized for the deposition of high-throughput combinatorial thin films, was used. Tubby had many attractive features, including the capability to deposit on up to three 3-in Si (or some other substrate material) wafers per pumpdown, as well as an array of four magnetron sputtering guns (Angstrom Sciences). The angles and placements of these guns determined the composition gradient that the resulting film would have. A large, 4-in DC magnetron gun (AJA, Inc.) allowed for the deposition of a uniform adhesion or diffusion-barrier layer. To measure the sputtering rate of each individual gun, or the overall rate while they cosputtered, a water-chilled quartz crystal thin-film thickness monitor (Inficon), or "XTM", was used. The substrates could be heated to around 500 °C by the use of small oblong halogen lamps situated inside the substrate holders. The chamber has been previously described in detail,[1] however, some modifications to the chamber were made, which are detailed below.

2.1.2 Installation of 5 mm Electrode Holder

Although Tubby had been previously optimized for high-throughput research, the samples that could be created in it were not ideal for oxygen reduction (ORR) studies, which typically rely on performing rotating disk electrode (RDE) voltammetry experiments in order to get quantitative, mechanistic information so that one could differentiate among possible reaction pathways. Consequently, an electrode holder was designed, by Dr. Raymond Burns, and was intended to hold substrates appropriate for rotating disk electrode experiments. This holder consisted of two aluminum disks with sixteen 5 mm holes drilled in a radial pattern, one in the center, with six spokes,

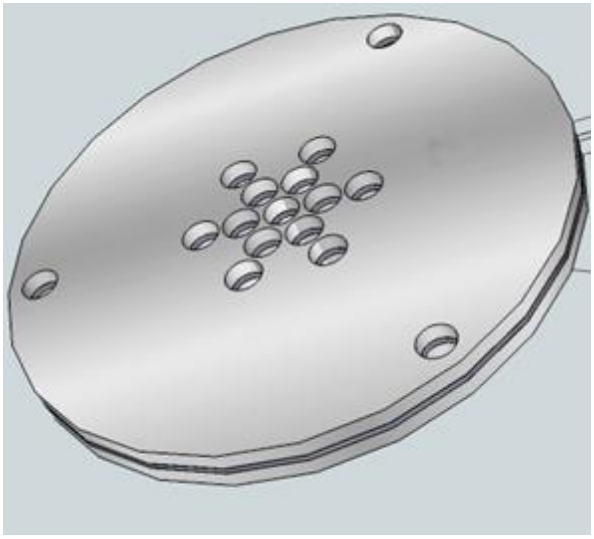

Figure 2.1. Bottom view of the RDE holder.

two holes on each spoke (Fig. 2.1). Additionally, three holes were drilled near the edges of the disks intended to have them near to the three sputtering guns. To keep the electrodes held in place, a vacuum-safe fluoropolymer rubber, Viton, was used as a gasket between the aluminum plates. An aluminum handle screwed into additional holes on the perimeter of the plates, and had a threaded hole in the top so that it could

screw into a long set screw on the aluminum ring of Tubby (Fig. 2.2). In this way, it could be rotated around the chamber, just as the regular substrate holders could be. An additional 3-mm electrode holder was made but not installed. Smaller electrodes

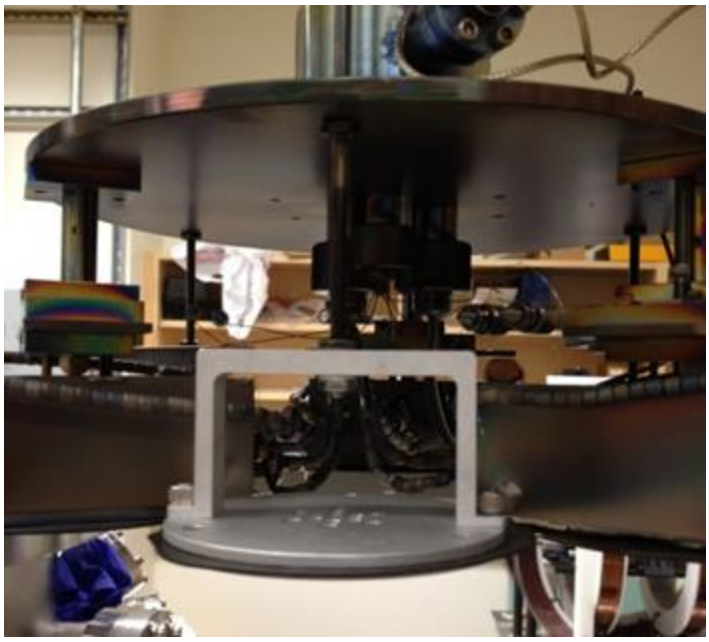

Figure 2.2. Side-view of the RDE holder on the set-screw in between two other substrate holders.

would give better composition resolution, but a special custom rotating disk holder would have to be constructed to accommodate the smaller electrodes, and so it was not used.

2.1.3 Installation of a New Feedthrough System

After a large leak was discovered in the wire and water tubes feedthrough on the lid of Tubby, it was determined that the leak could not be fixed without major changes to the lid and the feedthrough system. The wires to power the substrate

heaters, to house the thermocouples to detect the temperatures of the substrates, and to hold the water tubes (to cool the XTM) came up through the top of the chamber, and were held in place and sealed from the atmosphere to the vacuum with a vacuum-safe epoxy. This rubber, over time, had cracked, allowing air to get into the sealed chamber. In order to prevent the same problem from occurring again in the future, it was determined that a new, more robust feedthrough system would need to be constructed.

The new feedthrough used a custom-built stainless steel piece, shown in Fig. 2.3. Once installed, the wires and tubes would come up through the bottom of the piece, where there was a Quick-Connect valve to attach it to the top of the chamber.

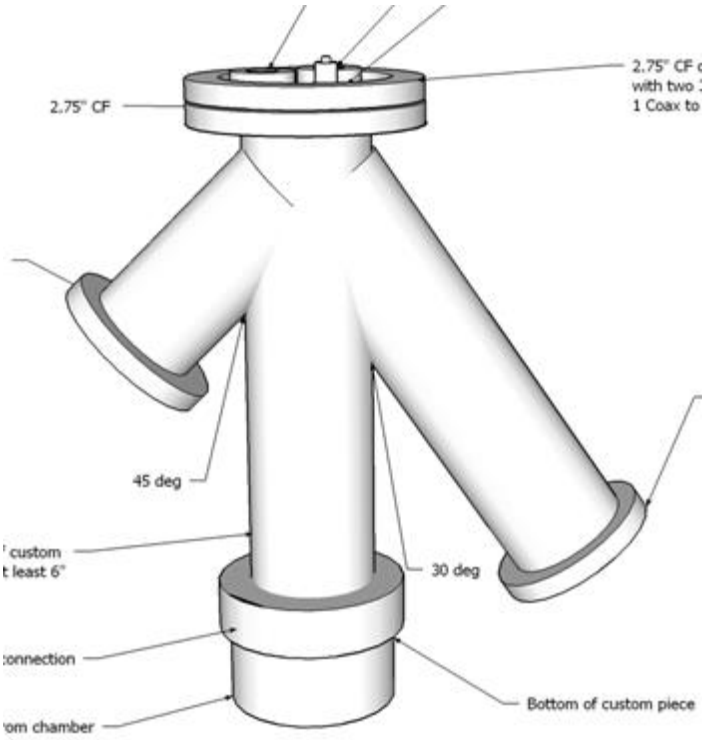

Figure 2.3 CAD drawing for the custom feedthrough piece.

Two arms came out from the sides, a wide, long arm at 30° and a shorter, narrower one at 45°. The large arm had a KF flange with the connecting piece holding spaces for four sets of thermocouples, three next to the existing wafer substrate holders (one each), and a fourth, that would be able to connect to the new 5 mm electrode holder within the chamber, should we (or future students) decide to install heaters. The small arm had a conflat flange with spaces for four sets of wires. These wires would be used, again, to power the three substrate heaters, as well as a possible fourth substrate heater that could be installed later.

In order to prevent these wires from shorting each other inside the narrow

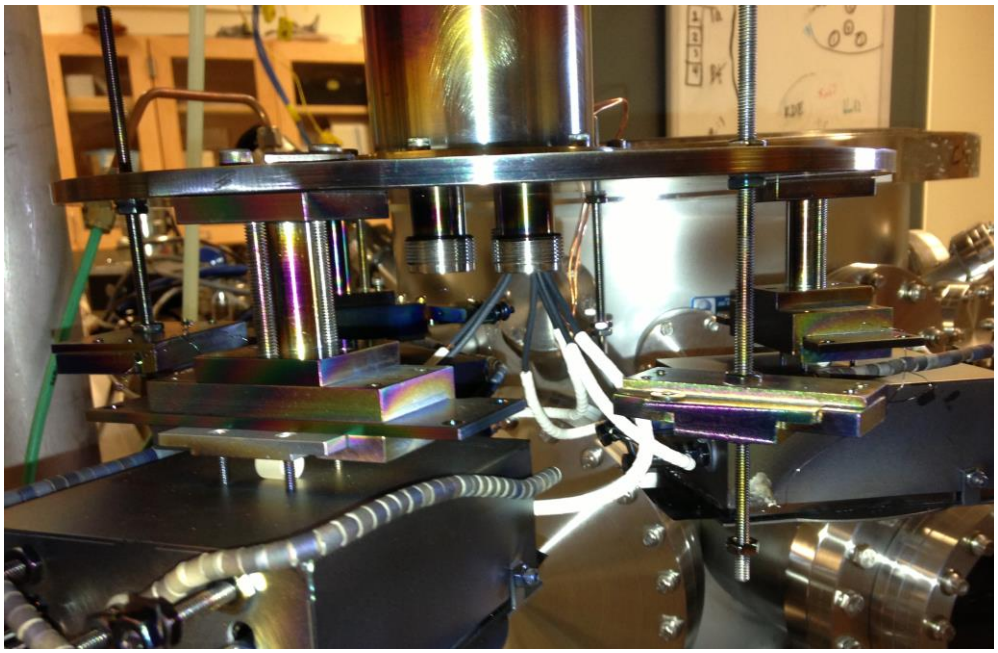

Figure 2.4. Heater wires covered with heat-shrink tubing (black) and ceramic beads (white.)

feedthrough piece, lengths of heat-shrink tubing were used to insulate the wires until they fed out of the neck, into the open part of the chamber, where they were protected with ceramic beads (Fig. 2.4). The top of the feedthrough would be used for the

cooling water tubes for the XTM, as well as the coaxial cable for the XTM. A new XTM, with longer steel water tubes was installed, and the tubes fit into the top of the piece. The top had another conflat flange to connect the feedthrough piece, allowing the steel tubes to be fitted with Quick-Connects on the top and bottom so that reinforced (nylon-wrapped) flexible tubing could be connected and held in place.

The installation of this new piece added around 2 kg of mass to the top of the chamber. This piece then had to be rotated along with the aluminum ring inside the chamber to prevent wires and tubes from twisting. Thus, the stepper motor had to move an additional 2.2 kg of mass. Hence, it no longer had enough torque to rotate the new piece plus the aluminum ring, and the motor burned out. It was then replaced with a higher-torque version. Although the same size model was ordered, the dimensions were slightly larger, so slits were filed into the motor's aluminum stage and fitted with wing nuts, so that the height of the stepper-motor could be adjusted to prevent the screws on the rotating feedthrough from scraping against the top of the motor.

2.1.4 Future Modifications

Although the electrode holder allowed for the additional capability of depositing samples for RDE, it did not allow for samples to be heated during deposition. Any heating would have to be performed as a post-anneal. A possible useful future modification would be to replace the electrode holder in Tubby with a box similar to the wafer substrate holders (although it might need to be slightly narrower to fit in with the space allowance), with a radiative heating element (halogen lamp) inside. When the feedthroughs were re-done, extra wires and thermocouples

were placed inside to prepare for this, but the heater installation project was never finished. It was determined that an effective method to hold the electrodes would be to have small screws in holes near the electrode holes. A small length of rather stiff Nb wire (or some other metal with a high melting point) could be looped around the electrode and anchored on the screw. Tightening and loosening the screw would ensure that the electrode had a tight fit in the hole.

2.1.5 Sputtering Parameters

Tubby was equipped with a mechanical pump to provide rough pumping, as well as a cryopump, to take it into the high-vacuum regime. Typical low pressures for Tubby were around 1.2×10^{-7} Torr. In practice, during sputtering a "cryoshroud", which sat on top of the sputtering guns, could be used to decrease the effective pressure (and increase the purity) even more.[1] The cryoshroud (see the red D-shape in the figure), allowed for liquid N_2 to be flowed through, so that it could condense impurity gases (particularly H_2O and O_2) to prevent oxidation of the deposited films. It was, therefore, particularly important to use when sputtering oxophilic materials, such as nitrides or base metals. The gas flow controller, allowed for the use of four different gases: Ar, CH_4, O_2, and N_2, to make a variety of classes of materials, although the O_2 was primarily used for post-deposition heating to form surface oxides. Gas flow rates were typically 75 sccm, and sputtering pressures were typically between 5-7.5 mTorr, depending on the application.

2.2 Electrochemistry

2.2.1 Electrochemical Instrumentation

Electrochemical measurements were all performed on one of two potentiostats. For measurements on the nitride catalyst support work using the electrochemical "mini-cell" (explained below) a BAS CV-27 was used. Oxygen reduction experiments were carried out on a Pine AFRDE5 bipotentiostat and used in conjunction with a Pine Instruments AFMSRX analytical rotator to perform rotating disk electrode (RDE) voltammetry. Data were recorded using in-house LabVIEW programs.

2.2.2 Working Electrodes: Disk Electrodes

For experiments using bulk electrode materials (such as glassy carbon, gold, platinum, etc.) without a thin film on top, the electrodes were home-built and constructed by drilling 2 differently-sized holes in to a Teflon rod. The electrode material was inserted into one side, and into the other side of the tube, graphite felt was inserted to make electrical contact with the electrode material. To make contact with the rotator, a stainless steel cap with a metal probe was pressed into the carbon felt and epoxied in place. This steel cap fitted the rotator shaft, which was held in place by a set screw. These electrodes were used for stationary and rotating disk experiments.

2.2.3 Working Electrodes: Thin Film Electrodes

To carry out electrochemical experiments—namely RDE voltammetry—with

glassy carbon electrodes (although these could be some other electrode material, if desired) with thin films deposited on them, the sputtered electrodes were inserted into Pine Instruments' ChangeDisk tip, shown in Fig. 2.5a. The ChangeDisk tip fit into an electrode holder with a gold-coated spring-loaded contact. This holder was attached to a rod that fit inside the AFMSRX rotator shaft. Although initial experiments allowed

a. 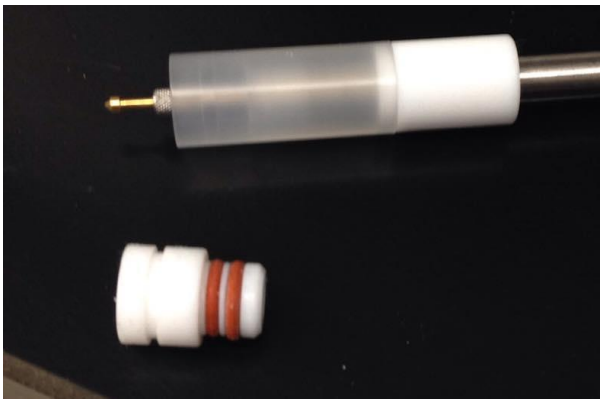 **b.** 

Figure 2.5. a.)The Pine ChangeDisk tip and holder, without an electrode. b.) the tip with a sputtered electrode, wrapped in Teflon tape.

for the insertion of the glassy carbon slugs into the tip holder without the tension in the back contact pushing out the electrode, the uniformity between different glassy carbon slugs, as well as the plastic deformation of the Teflon ChangeDisk top holder meant that even initially a very small subset of glassy carbon slugs were large enough to stay in the tip, and over time even those were pushed out. To combat these issues, a small (~2 cm) piece of Teflon tape was cut, a corner of it stretched to be thinner, and that was wound around the side of the electrode a few times, as seen in Fig 2.5b. This prevented the electrode from popping out when the tip was connected to the electrode holder.

2.2.4 Working Electrodes: Ring-Disk Electrodes

In order to corroborate mechanistic data obtained by Levich analysis, a rotating ring-disk electrode (RRDE) was used to detect H_2O_2 or HO_2^- electrochemically. The RRDE consisted of a disk electrode, a small plastic spacer, and then a thin ring electrode. The ring was held at a potential, in this case a potential to oxidize the formed H_2O_2 or HO_2^-, and the disk was cycled—in other words, "collection" experiments. Redox-active species generated at the disk would diffuse away to the ring, where they would be detected, and in that way it can be seen under which potentials the electroactive species were generated, or if they were generated at all.

Two RRDE's were used in this work. The first was a Pt-Pt RRDE (Pt ring and Pt disk). The second was a Au-interchangeable RRDE (Au ring, interchangeable disk), which could be used with any of the sputtered glassy carbon electrodes, as well as some other disk electrode. Both were manufactured by Pine Instruments. Typical potentials to hold the ring were around 1.2 V vs RHE.

2.2.5 Reference Electrode

A Ag/AgCl reference electrode was used for all experiments. For experiments using the electrochemical "mini-cell", a BASi electrode was used, and during experimentation it was housed in a separate scintillation vial filled with the electrolyte/analyte solution and connected to the working electrode chamber via a long, plastic capillary. For RDE experiments, we employed a home-built Ag/AgCl electrode housed in a separate compartment of the electrochemical cell, separated by a glass frit to prevent Cl^- contamination from affecting the electrode. For many figures,

these potentials were normalized to a reversible hydrogen electrode (RHE), a pH-normalized reference electrode. The RHE potential was determined by the equilibrium of the reduction of H^+ to H_2. This equilibrium shifts with pH, according to the following equation:

$$E_{RHE} = E_{SHE} - \frac{RT}{F} \ln \left[\frac{a_{H^+}}{(P_{H_2})^{\frac{1}{2}}} \right] \approx E_{SHE} + 0.059V \cdot pH$$

The potential of the SHE (or standard hydrogen electrode), a pH-independent reference electrode, is related to a saturated Ag/AgCl electrode by 0.197 V.

2.2.6 Counter Electrode

Different counter electrodes were used for different experiments. In the electrochemical mini-cell, a wound Grafoil counter electrode was used so as not to contaminate the surface/working electrode with any catalytic precious or platinum-group metal ions. For rotating disk experiments, a high surface area Pt mesh electrode was used, unless experiments were designated as "Pt-free", also meaning that the glassware had either never been used with a Pt-containing electrode, or had been thoroughly cleaned with aqua regia to remove any metal impurities. In the experiments designated as "Pt-free", a graphite rod was used as the counter electrode, with the top filed to an angle to provide a suitable place for the alligator clips to fasten.

2.2.7 The Electrochemical "Mini-Cell"

The electrochemical "mini-cell," so named because its working/counter electrode compartment was small (holding roughly 1 mL) was used to test the

electrochemical behavior of thin films deposited on wafers (Fig. 2.6). The mini-cell consisted of a plastic stage with grooves cut into the sides. These groves allowed spade-head thumb screws to sit in them, and they screwed into a plastic base. By loosening the thumb screws, the plastic bases could be moved to provide y-resolution. These plastic bases held up each side of a metal bar with a cutout in the middle. In the cutout sat a metal tab that could slide to provide x-resolution. From the tab, a set screw with two screw handles held a hollowed-out Teflon tube that served as the working

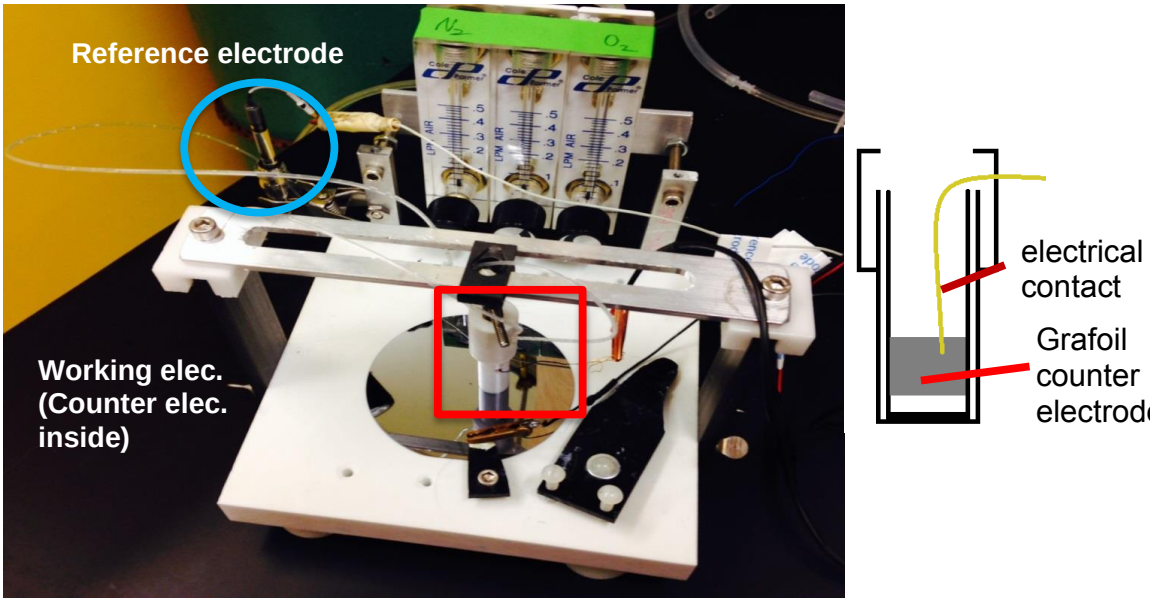

Figure 2.6. Electrochemical mini-cell with cutaway of working electrode chamber.

electrode. The height of the Teflon tube could be adjusted using the set screw, and this allowed the tube to form a water-tight seal against the wafer, with the aid of an O-ring. Inside the Teflon tube, a Grafoil counter electrode sat with a hole in the side of the tube allowing a gold wire (coated in black wax), to exit the tube to make an electrical connection with the potentiostat. Out of another hole drilled into the side of the tube came three other tubes: one to connect the reference electrode, one to fill the cell, and

one to drain the cell. Although the solution only came into contact with a small part of the wafer, because of the O-ring, the current was not conducted through a wire in the Teflon tube, but instead was conducted either through the film or down through the doped Si substrate to a small spring-loaded lever with two metal teeth. Alligator clips connected to the potentiostat could then be clipped to the tops of those teeth.

2.2.8 Corrosion Experiments

To look for electrochemical evidence of corrosion in the nitride thin films, first the stable potential window of the films was initially determined by doing a window-opening cyclic voltammogram (CV). These were performed by first starting with a very narrow potential range, and then gradually increased negative by 100-200 mV at a time, until H_2 evolution was reached. In order to prevent the formation of H_2 bubbles on the surface of the film (as the opaque Teflon cell does not allow for the surface of the film to be seen), the lower potential limit was moved to slightly less reducing potentials in order to prevent H_2 evolution. After the determination of a stable lower potential range, the upper potential limit was determined by slowly increasing the potential 100 mV at a time until a large oxidation current, which would not decrease with increasing potential (indicating that the sample was either oxidizing irreversibly or that water was being oxidized),was reached.

After the window-opening CV, the time-dependent response of the materials was monitored electrochemically by cycling over the stable potential window for prescribed periods of time. These specific times are discussed in more depth in Chapter 3. Although the Department of Energy benchmarks specified holding a

sample at a high potential for long periods of time, because the potential conditions in a fuel cell will vary,[2] it was determined that potential cycling would be more stressful and provide more accurate conditions than just holding the electrode at high potential. Additional experiments are described in Chapter 3.

2.2.9 Oxygen Reduction Experiments

Oxygen reduction experiments were conducted in a three-neck specially-built RDE cell, with an inner compartment used to prevent cavitation (whirlpool/eddy formation). The RDE cell had a special glass cap that was used to maintain a specified atmosphere over the solution, while still allowing the rod to rotate in the middle. Electrodes were first placed in an electrolyte solution, which was subsequently deoxygenated. To deoxygenate the solution, it was purged with N_2 for 15 min. After purging, the electrode was cycled electrochemically to clean it, with N_2 blowing over the surface of the solution (to maintain a N_2 atmosphere without perturbing the solution), until the CV remained constant from cycle to cycle. At that point, the N_2 was exchanged for O_2, and the solution was saturated with oxygen for 15 min. while continuing to cycle the potential to keep the surface of the electrode clean.

After the 15 min. had elapsed, the O_2 tube was pulled from the solution to blow over it, the rotator was switched on, and two complete potential cycles were recorded. Rotation rates from 50 – 3000 rpm were used, depending on the type of electrode. Bulk RDE electrodes were able to be used over the entire range, generally with 13 different rotation rates, whereas the Change Disk electrode could not be used above 2000 rpm. The thin films often used on those electrodes, generally could not withstand

the extra duration of the full set of rotation rates, and so were only used for around 7 different rates. In between each rotation rate, the solution was purged with O_2 for 6-7 min, which was particularly important at higher rotation rates when the surface of the solution was agitated more, causing some of the O_2 to come out of solution. The electrolyte solution affected the concentration and diffusion coefficients of O_2, and different values were used for each, as shown in Table 2.1.

Table 2.1. Table of constants used for different electrolyte solutions.

Electrolyte	**D_{O2} (cm^2/s)**	**C_{O2} (mM)**
$HClO_4$, 0.1 M	1.63×10^{-5}	1.27×10^{-3}
NaOH, 1.0 M	8.00×10^{-6}	1.70×10^{-3}
NaOH, 0.1 M	1.93×10^{-5}	1.26×10^{-3}

2.3 References

(1) Gregoire, J. M.; van Dover, R. B.; Jin, J.; DiSalvo, F. J.; Abruña, H. D. *Rev. Sci. Instrum.* **2007**, *78* (7), 072212–072212 – 6.

(2) Crowtz, T. C.; Stevens, D. A.; Sanderson, R. J.; Harlow, J. E.; Vernstrom, G. D.; Atanasoska, L. L.; Haugen, G. M.; Atanasoski, R. T.; Dahn, J. R. *J. Electrochem. Soc.* **2014**, *161* (10), F961–F968.

CHAPTER 3

Screening of Nitrides as Catalyst Supports

Work in this chapter was done in collaboration with Dr. James O'Dea, Anna Legard, Dr. Raymond Burns, and Megan Holtz.

The following section constitutes a submitted manuscript titled:

3.1 "Electrochemical Characterization of Ta-Ti-Al Nitride Thin Films"

Authors: Abigail R. Van Wassen, Anna E. Legard, James R. O'Dea, Samuel D. Young, Raymond G. Burns, Francis J. DiSalvo, John A. Marohn, R. Bruce van Dover, and Héctor D. Abruña

3.1.1 Abstract

Ta-Ti-Al nitride composition spread thin films have been prepared and characterized by conductive-probe atomic force microscopy (cp-AFM), and four compositions in the spread were selected for further electrochemical characterization and testing. These compositions corresponded to one spot with approximately stoichiometrically equal nitride ratios (equal parts Ti, Ta, and Al) and three spots with each enriched in one of the metal nitrides. Each spot was found to have a wide electrochemical stability window of at least 1.4 V in 0.1 M H_2SO_4 with an upper potential limit of at least +0.9 V vs Ag/AgCl (or +1.13 V vs NHE). Each of the tested compositions was more stable, over extended time periods of electrochemical cycling,

than the parent nitrides. While the cyclic voltammograms (CVs) of the quaternary films showed little change over eight hours, those of the single-metal nitrides exhibited significant changes in double-layer capacitance. Cp-AFM, performed at each position, yielded results that are consistent with surface oxidation upon extended electrochemical cycling. Electrochemical measurements confirmed that beneath the oxidized surface, sufficient conductivity was preserved, albeit lowered, ostensibly under a protective oxidized shell. Based on the electrochemical and cp-AFM results, we find that the compositions with approximately 33% Ti and higher are the most promising as catalyst support materials in terms of durability/stability and conductivity.

3.1.2 Introduction

A significant impediment to the wide-spread deployment of fuel cells is degradation of the carbon black catalyst support, and subsequent agglomeration of the catalysts nanoparticles, as mentioned in previous work.[1,2] This degradation results from the oxidation of the carbon black to CO_2, which is catalyzed by Pt under fuel-deficient ("hydrogen starvation") or resulting from oxygen-rich conditions.[3] There have been several approaches to solve or mitigate this problem, and ours has been to replace the carbon support with (non-carbon) materials that are less susceptible to oxidative degradation.[1] Using non-carbon support materials additionally allows for the potential to introduce, and take advantage of, potential co-catalytic activity from the support,[4] which could enable a decrease in the amount of Pt (and other PGM; platinum group metals) and thus overall expense, as well as an increase in their efficiency.

Several classes of materials have been proposed as catalyst supports to replace carbon black, including organic nanostructured whiskers,[5,6] carbides,[7–9] oxides,[10–12] and nitrides.[13–15] Desired support characteristics include high electrical conductivity,[16] durability under fuel cell operating conditions, and sufficient porosity to allow gases to diffuse to the catalyst nanoparticles. Co-catalytic (enhanced) activity is also desirable for economic reasons and for the efficient use of the Pt electrocatalysts. In our work, we have chosen to study nitrides as catalyst supports. Nitrides have high electrical conductivity,[4,17] are chemically durable under acidic conditions,[18,19] can be synthesized as porous nanoparticle aggregates,[17,20] and may also exhibit some catalytic activity by themselves.[4,21] Their oxidation is generally self-limiting at temperatures below 200°C,[22,23] so that even with a thin, protective oxidized coating, nitrides can be sufficiently conductive to serve as catalyst supports. We previously showed that Ta-Ti-Al nitrides with at least 20 at% Ti are highly conductive when prepared with a 2 nm thick protective oxide shell.[1]

Nitrides have been previously studied for use as catalyst supports, primarily because of their superior resistance to corrosion. TiN is deposited on drill bits and other cutting tools as a protective coating. Bipolar plates for fuel cells, have also been coated with TiN to impart corrosion resistance.[24] In addition to being highly durable, many nitrides are highly conductive ($\approx 10^4$ S/cm). TiN or TiN-containing materials, in particular, have been the focus of studies of nitrides as catalyst supports.[4,14,17,20,21] TiN is especially conductive and may catalyze the oxygen reduction reaction (ORR) on its own;[4,21] although at potentials lower than desirable for an ORR catalyst in fuel cell applications. While some nitrides are conductive and corrosion-resistant,

thermodynamics favor their oxidation,[25–27] so temporal studies of the through-surface conductivity as well as the conductivity along the film (parallel to, but under the surface) are essential.

Based on our earlier work, we chose to examine the Ta-Ti-Al-N system in detail since we previously found it to be sufficiently conductive for consideration as catalyst supports. In addition, Ti-rich compositions retained their conductivity under oxidizing conditions, and, in fact were the best among those tested.[1]

Here, we explore the electrochemical stability of this system in greater detail under acidic conditions and over a wide potential range. We sought to explore the properties of the component nitrides in a class of new materials that might exploit increased stability imparted by having mixed cation sizes. We chose TiN as one component because it is highly conductive and has been shown to exhibit some catalytic activity.[4,21] Additionally, it might help to mitigate degradation of the underlying carbon steel substrate under corrosive conditions.[28] AlN is an insulator, although its conductivity can be improved through the addition of impurities or dopants.[1,29] Nevertheless, it is quite durable, oxidizing in bulk at elevated (700°C) temperatures and dissolving in harsh conditions, such as boiling in 50% HCl.[30] Doping TiN with Al could shift the onset of corrosion to more oxidizing potentials, inhibiting corrosion.[31,32] Finally, the addition of Ta to Ti-Al-N imparts mechanical strength and improved oxidation resistance.[33,34] Ta can form three different nitrides: the conductive TaN (5.55×10^4 S/cm)) and Ta_2N (4.3×10^4 S/cm), and the insulating Ta_3N_5 ($<10^{-4}$ S/cm).[16,35,36] Careful choice of reactive sputtering conditions (especially Ar/N_2 mole ratio in the sputter gas mix) allows for selection of the conducting nitrides over the

insulating nitride, allowing the integration of the benefits of TaN without compromising the conductivity of the material.

In this work, we go beyond our initial study[1] of the conductivity, microstructure, and local oxidation of sputter-deposited thin films of Ta-Ti-Al nitrides to electrochemically explore the kinetically-limited surface stability of these materials. We first used electrochemical cycling to determine the potential range within which the combinatorial films remained electrochemically stable. We then used electrochemical cycling experiments followed by cp-AFM measurements to screen the conductivity of the combinatorial films before and after being subjected to oxidizing conditions.

3.1.3 Methods

3.1.3.1 Film deposition

Films were prepared in a custom-built combinatorial sputter deposition system[37] following the previously described method for generating sputtered nitride films at 400 °C with a subsequent oxygen anneal at 250 °C to form a thin protective oxide layer.[1] A 3-inch diameter Si wafer, with a native oxide layer, was first covered with a 12 nm Ti adhesion layer in 0.67 Pa of Ar (99.999%). Three-component combinatorial libraries were then deposited while radiatively heating the substrate to 400 °C. Libraries were co-sputtered using elemental targets of Al, Ta, and Ti (Angstrom Sciences, >99.99% purity) in a 1.0 Pa Ar/N_2 (13 vol. % N_2) atmosphere at a rate of 3 nmol/s, to form a nitride film 50 nm thick. Single-element nitride films were sputtered from each target separately using the same deposition procedure and

parameters. Films were cooled in vacuum, held at 250 °C for one hour in a 0.13 Pa O_2 (99.994%) atmosphere, and finally cooled to room temperature before being removed from the deposition chamber.

3.1.3.2 Electrochemical Mini-cell

To maintain the integrity of the deposited thin-film samples, an electrochemical testing apparatus ("mini-cell" Fig. 3.1a) was developed that allows for electrochemical isolation of selected areas of the thin film libraries, enabling testing without mechanically fracturing the sample and thus maintaining its integrity. The apparatus was used in earlier work.[38] The mini-cell primarily consists of a 2.5 cm tall, 0.8 mL movable Teflon tube (Fig. 3.1a). The mouth of this cell features a 6 mm inner diameter Viton (fluoroelastomer) O-ring that defines and electrochemically isolates the testing area (0.32 cm^2) of each site. Electrical contact to the sample wafer was made through two spring-loaded gold-plated probes (Mouser Electronics, GSS-8-7-G) at the edge of the sample. The counter electrode was a coiled strip of Grafoil contained within the Teflon cell, held in solution approximately 2 cm above the substrate surface. A Ag/AgCl reference electrode (BASi, RE-5B) was connected to the cell via a capillary, enabling it to move with the working electrode. The potential of the sample was controlled using a BAS CV-27 potentiostat.

3.1.3.3 Electrochemical Testing

Four areas of interest in the quaternary composition spread film were selected for electrochemical characterization with the mini-cell (Fig. 3.1b). Three of these

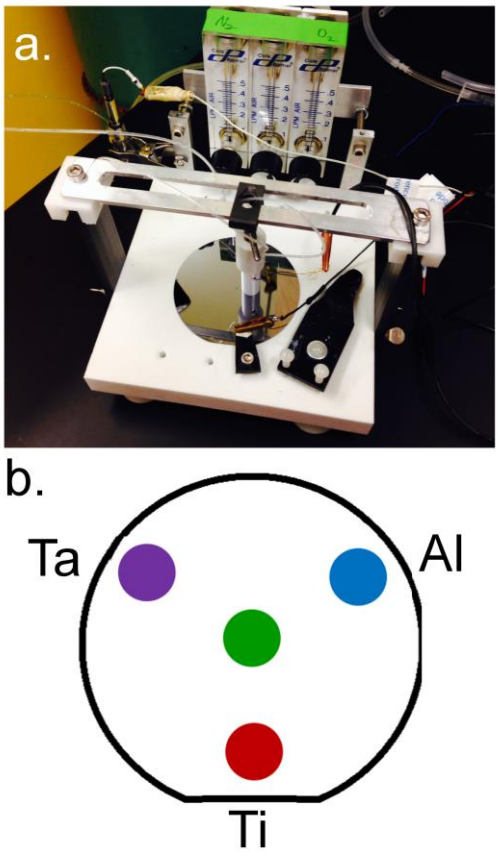

Figure 3.1 a.) Photograph of the electrochemical mini-cell. The Teflon tube contains the counter electrode, and makes a seal with an area of the film that then serves as the working electrode. The reference electrode is not shown**.** **b.)** Diagram of the four areas of the film that were tested. Four spots not to scale.

regions corresponded to compositions rich in each individual metal nitride. The positions form a triangle with vertices aligned with the orientation of the sputter guns during deposition.[37] The fourth location, at the center of the wafer, corresponded to a nitride with approximately equal ratios of each metal. Each location was initially

conductive enough that a blank cyclic voltammogram (CV) could be readily obtained. Because of the initially uniform morphology, as previously shown by AFM[1], and the very small currents being passed, differences in conductivity were manifest as differences in the electrical double layer current, wherein more conductive nitrides passed more current and had larger double layer capacitances. Single metal nitride films (TaN, AlN, and TiN) were also electrochemically tested to compare and contrast their behavior to the composition-spread film.

To ascertain a stable potential range for the materials, "window-opening" CVs were collected in 0.1 M H_2SO_4 (Sigma-Aldrich, 99.999%) at each of the four positions and on the single-element nitride samples. CVs were obtained at a sweep rate of 50 mV/s. Some of the data were noisy due to the setting of the current amplifier (Ta and Al in particular) and were smoothed in order to better compare them to other samples (Fig. 3.2 insets). Data were smoothed using an adjacent averaging profile (20 adjacent points for each point) for each smoothed data set.

3.1.3.4 Electrochemical Stability Testing Conditions

Based on the window-opening CVs, a potential range was selected over which all four positions (compositions) on the sample were stable (-0.5 to 0.9V vs. Ag/AgCl). This range was subsequently used for extended cycling. In an effort to simulate the conditions experienced in a PEM fuel cell stack, each position of the film was electrochemically cycled in 0.1 M H_2SO_4 over this potential range at 50 mV/s initially for 2 hours (approximately 120 cycles) and then for a total of 8 hours (over 500 cycles). The same tests were carried out on the single-element nitride samples.

To further mimic the conditions of an operating fuel cell, a Ti-rich area of the quaternary film was selected for electrochemical testing in a freshly prepared 5 wt % solution of Nafion, diluted with water (Fuel Cell Store, DE1021, 10 wt %). After establishing that the film was stable in the Nafion solution over the potential range used for the extended cycling in H_2SO_4, a CV was obtained (50 mV/s). The setup then sat for 24 hours without electrochemical cycling. After 24 hours, the solution was removed and replaced with a fresh Nafion solution and a CV was obtained.

The following section was written by Dr. James O'Dea.

3.1.3.5 Scanned Probe Microscopy

Conductive probe atomic force microscopy (cp-AFM) images were taken with Pt-coated cantilevers (MikroMasch, DPE17, <40 nm tip radius) with a +50 mV sample bias and a tip-sample force of 10 nN (Veeco, D3100). Current-amplifier gains of 1 nA/V and 100 nA/V were used to image regions with a current response below and above 10 nA, respectively. For comparison, images of the pristine film were taken 6 mm outside the area exposed to the electrochemical testing. Images taken on areas of the film subjected to electrochemical cycling were acquired directly in the center of the well's footprint.

3.1.4 Results & Discussion

3.1.4.1 Stability Range & Extended Cycling

In order to maintain uniformity in electrochemical testing among all areas of the film, a potential range of -0.50 to 0.90 V vs Ag/AgCl was used for all electrochemical testing, as described in the methods section, although some regions

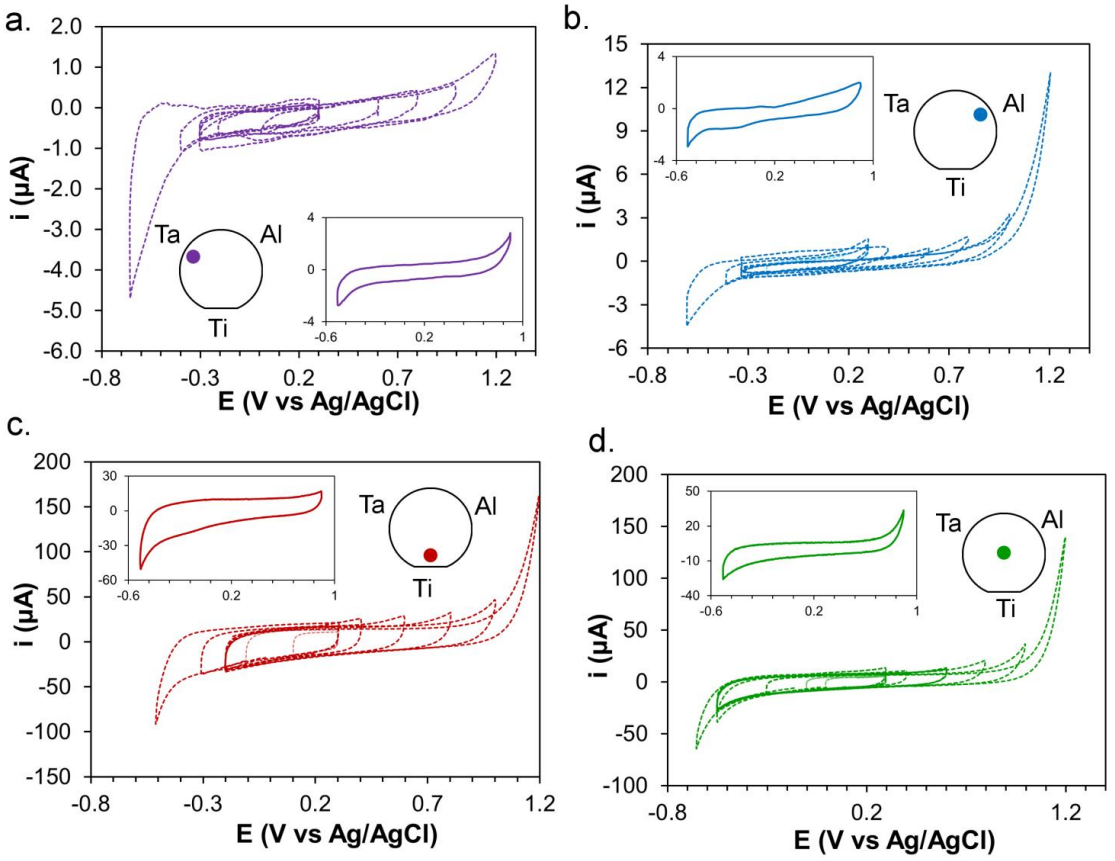

Figure 3.2. Window-opening CVs for each area of the films tested in 0.1 M H_2SO_4. Mock wafers indicate which section of the film was tested, corresponding to a.) Ta-rich, b.) Al-rich, c.) Ti-rich, and d.) mixed composition. Inset CV's show the final range chosen (-0.5 to 0.9 V) with curve smoothing. (ν = 50 mV/s).

exhibited stability over an even wider potential range (Fig. 3.2). To ensure that the measured electrochemical properties were characteristic (representative) of the mixed-cation film, and not of the individual components, single-metal nitride films (TiN, TaN, AlN) were also examined (Fig. 3.3). As expected, AlN was insulating and passed no current. TaN oxidized at lower potentials than the Ta-rich region of the quaternary film. This decrease in oxidative current suggests that the pure TaN also formed a passivating oxide after a few cycles. This is consistent with our previous microscopy data that showed a 2 nm-thick oxide layer on the surface of the quaternary film.[1] The behavior of TiN was very similar to the Ti-rich area of the quaternary film, although it demonstrated less anisotropy at reducing potentials relative to the Ti-rich regions of the film.

To mimic fuel cell operating conditions, we cycled each of the four selected areas for eight hours. As shown in Fig. 3.4, the shapes of the CVs after cycling remained very similar to those of the original CVs in each region. In each CV, after

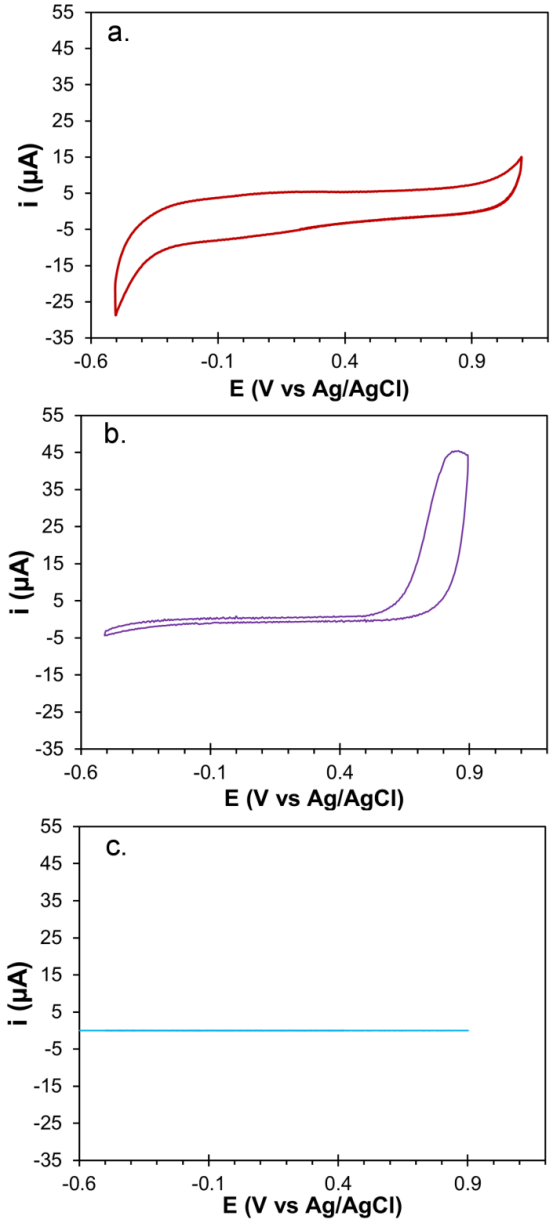

Figure 3.3. CV's of a.) TiN, b.) TaN, c.) AlN. ν = 50 mV/s, 0.1 M H_2SO_4

eight hours, there was a decrease in the oxidation current that may indicate that while

the film initially oxidizes, after a few cycles, a passivating layer develops and appears to prevent deeper or corrosive oxidation of the film while maintaining some through-surface conductivity. The CV profiles changed very little after approximately fifteen cycles (15 min), suggesting that the films passivate and stabilize quickly. The Ta- and Al-rich regions of the film showed a slight slant in the CVs after eight hours, suggesting that the films are more resistive in those areas than they were initially. The

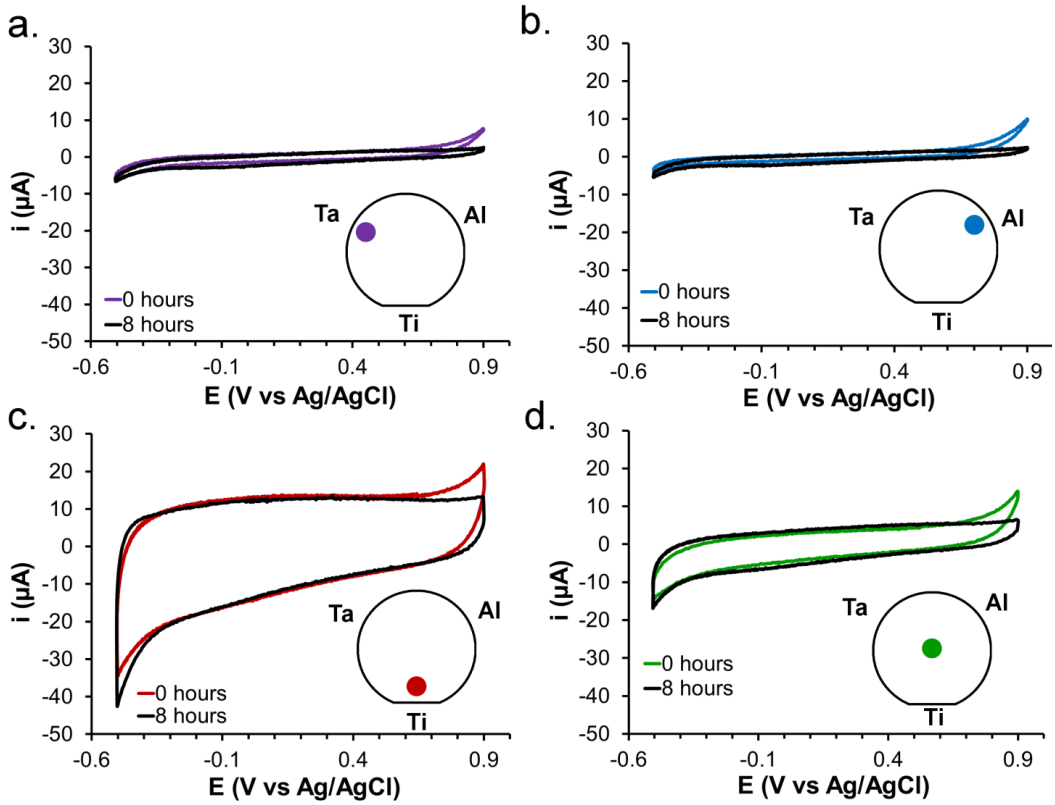

Figure 3.4. CVs before and after eight hours of cycling at each of the four indicated spots in 0.1 M H_2SO_4. The insets indicate which areas of the film were tested. (ν = 50 mV/s)

Ti-rich region and the mixed composition (center) spot exhibited very little change in their double layer current or in the slant of the voltammetry after eight hours, other than the initial decrease in the oxidation current.

The eight-hour test of TiN revealed very different behavior. Although the CV of TiN initially appeared to be very similar to that of the Ti-rich area of the quaternary film, (Fig. 3.5) the double-layer current decreased by about a factor of three after the eight hours of electrochemical cycling. This decrease in current was likely caused by a decrease in the electrochemically active surface area of TiN as it was oxidized. We also observed a large decrease in the conductivity of the TiN film with cp-AFM (vide infra) after eight hours of electrochemical cycling (Fig. 3.6).

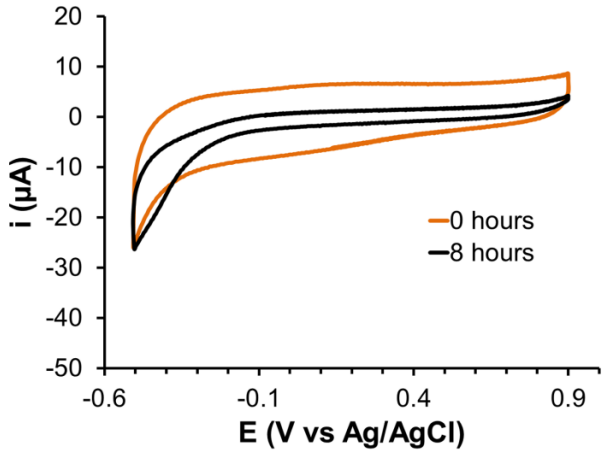

Figure 3.5. CVs of TiN before and after eight hours of electrochemical cycling in 0.1 M H_2SO_4 . (ν = 50 mV/s).

As shown below, conductive probe AFM measurements taken over areas subjected to extended electrochemical cycling revealed that the Ti-rich regions remained the most conductive and that the surface conductivity (compared to the pristine condition) decreased with electrochemical cycling at all compositions, an effect attributed to growth of an oxidized layer. Ti-rich regions maintained the highest conductivity overall.

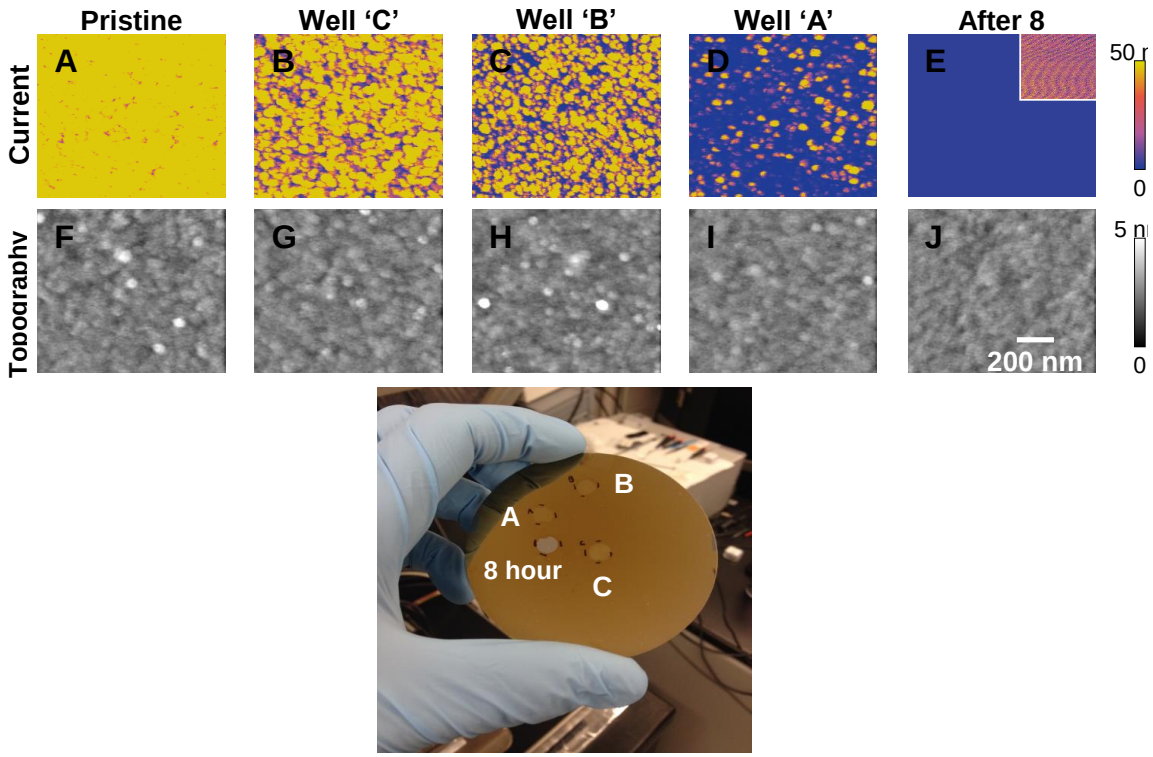

Figure 3.6. Current (A-E) and corresponding topography (F-J) images of TiN taken as a function of electrochemical cycling in 0.1M H_2SO_4 from -0.5 V to 0.9 V vs Ag/AgCl (ν = 50 mV/s). The pristine film (A) showed the highest conductivity. Electrochemical cycling of the film decreased the film's conductivity until no current was measured in a film cycled for 8 hours (E). The inset in (E) shows the image plotted on a color bar ranging from 0 to 50 pA, showing that the 8 hour cycling eliminated all conductive regions of the film, leaving an image consisting only of noise from the current amplifier. Each electrochemical cycling event was performed on a fresh TiN sample. No dramatic differences in topography are seen in TiN as a function of cycling. The average roughness of the images in (F-J) is 0.49±0.05 nm. The same Pt coated AFM tip was used to image all five samples and a constant tip-sample force of ~10 nN was used for each image.

3.1.4.2 Stability in Nafion Solution

In order to more closely mimic the conditions found in a fuel cell and to compare the results to the somewhat harsher H_2SO_4 studies, part of the Ti-rich

composition of the film was soaked in 5% Nafion solution for 24 hours. CVs obtained on a pristine Ti-rich area of the film were qualitatively similar to those obtained after soaking the film in a 5 wt % Nafion solution for 24 hours, (Fig. 3.7), with the same general shape and very similar currents. There was a small increase in the double layer

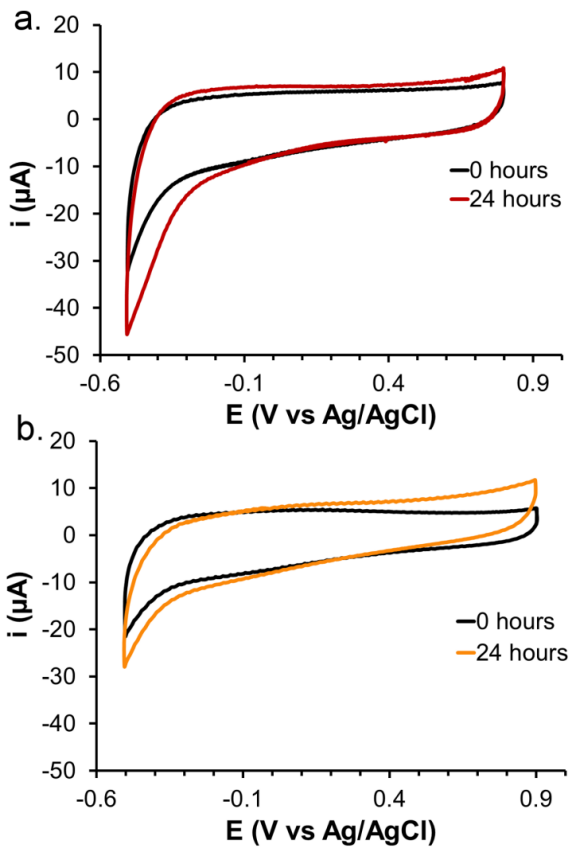

Figure 3.7. a.) CVs of Ti-rich region of a quaternary film and b.) TiN film, before and after 24 hours of soaking in 5 wt. % Nafion solution. (ν = 50 mV/s).

capacitance at all potentials as illustrated by the increase in current by about 2µA. This may be caused by an increase in surface area, possibly due to dissolution of some of the thin film. Because the change in the double layer capacitance was so small, however, this suggested a negligible difference in the surface area. We conclude that under these test conditions, the Ti-rich region of the quaternary film is stable,

especially when compared to the performance of a TiN film tested under the same conditions (Fig. 3.7b).

Like the Ti-rich quaternary composition that was tested, the TiN had very few changes in its double layer current, indicating that there was very little change in the surface area. Unlike the quaternary film, however, the TiN film developed a pronounced slant, indicating that the resistance is increasing after exposure to Nafion solution, likely caused by an insulating oxide shell.

The following section was written by Dr. James O'Dea.

3.1.4.3 Conductive Probe AFM

In the extended bulk electrochemical measurements, the current decreased with successive scans in all but the Ti-rich regions, indicating ongoing oxidation of the thin film (Fig. 3.8A–D). The decrease in conductivity of the Al-rich, Ta-rich, and center regions was confirmed with cp-AFM. The morphology of the films remained unchanged after 2 and 8 hours of electrochemical cycling (Fig. 3.8). Qualitatively, the 8 hour results agree with the 2 hour results in that the Ti-rich remained the most conductive after cycling and the Ti-rich > Ta-rich > Al-rich before cycling. (Images of films cycled for 2 hours and 8 hours were taken with different AFM tips and scan conditions, allowing for qualitative but not quantitative comparisons.) Much lower currents were measured at areas subjected to bulk electrochemical cycling (8–L) compared to pristine areas (Fig. 3.8E–H). The high sensitivity of cp-AFM

measurements, compared to bulk measurements, also revealed a decrease in conductivity of the Ti-rich regions after cycling. Interestingly, however, highly conductive islands (current >3 nA) remained present in Ti-rich regions after electrochemical cycling. As shown in local oxidation experiments,[1] these islands showed little to no decrease in current compared to pristine areas of the film that were rich in Ti. The highly conductive islands cover ~35% of the image in Fig. 3.8L which roughly corresponds to the Ti content (30 to 45 atomic %) measured at this region of

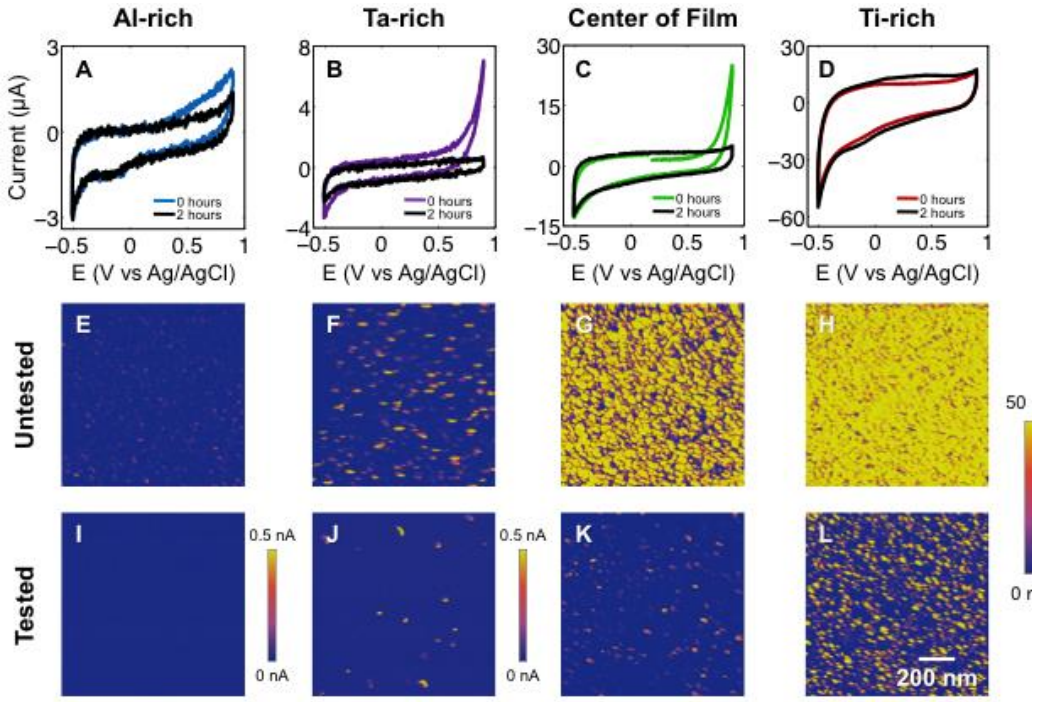

Figure 3.8. (A-D) Cyclic voltammograms taken over four different 0.32 cm^2 areas of the Ta-Ti-Al nitride thin film. Each location of the film was cycled continuously for 2 hours from -0.5 to 0.9 V vs Ag/AgCl in 0.1M H_2SO_4 (v = at 50 mV/s). Current is shown for the initial sweep after 2 hours of cycling. 1 μm × 1 μm cp-AFM images taken on areas untested (E-H) and tested (I-L) with bulk electrochemical cycling. Current in (I) and (J) was plotted using a colorbar ranging from 0 to 0.5 nA due to the low signal in these measurements.

the film.[1] We emphasize that even the most Ti-rich compositions of the film still had ~55 at.% of Ta and Al, which are non-conductive because AlN, Al_2O_3, Ta_3N_5, and Ta_2O_5 are insulators. The highly conductive islands in Ti-rich compositions are presumably the ~5 nm diameter Ti-rich columns seen in high-resolution elemental mapping in our previous study.[1]

cp-AFM revealed that the Ti-rich compositions remained the most conductive after electrochemical cycling, followed by the area at the center of the film and Ta- and Al-rich compositions. The conductivity of Ta-rich and Al-rich regions after cycling was extremely low. The measured current in both regions was at, or only slightly above, the noise floor of the current amplifier. The faint, left-to-right streaks in the current images in Fig. 3.6I and J (plotted on a color bar from 0 to 0.5 nA) correspond mostly to background noise of the current amplifier. The low conductivity of pristine Al- and Ta-rich compositions seen here (Fig. 3.8 E and F) agrees with that seen in our previous work[1] and is associated with the formation of non-conducting surface oxides at these compositions.

3.1.5 Conclusions

While Ta-Ti-Al_N films have a composition-dependent conductivity, all compositions tested were found to be stable over a potential range of at least 1.4 V (between -0.50 to 0.90 V vs Ag/AgCl at pH = 1), a potential range sufficiently wide to enable use in fuel cells. The $Ta_{.33}Ti_{.33}Al_{.33}N$ composition (at the center of the composition spread) and Ti-rich compositions passed the highest currents and

exhibited the lowest degradation in performance after continuous electrochemical cycling. cp-AFM measurements are consistent with these findings, showing that the Ti-rich and $Ta_{.33}Ti_{.33}Al_{.33}N$ regions of the film retained the highest conductivities after cycling, while Al- and Ta-rich areas of the film become significantly more resistive. Long-term exposure to Nafion had little effect on the Ti-rich area of the film, indicating that the typical fuel cell electrolytes are not corrosive to the material. Additionally, the quaternary nitride showed better oxidation tolerance and long-term stability than any of the individual metal nitrides. Considering the protection from oxidation and its good conductivity, we find that materials in the Ta-Ti-Al-N system are promising for use as a fuel cell catalyst supports.

3.2 Choice of nitride materials

Degradation or ageing of Pt (or other metal) catalysts in a fuel cell can lead to a decline in the fuel cell performance. This decline can also be facilitated by the corrosion of the catalyst support which can allow for aggregation of the catalyst, and a concomitant loss in surface area. A way to improve long-term fuel cell performance without developing better catalysts, therefore, can be to improve the durability of the catalyst support. Typical catalyst supports in a fuel cell are graphitic carbon black, as it is inexpensive, conductive, and durable, though is able to be oxidized by Pt catalysts. In this chapter, we have investigated the use of other abundant, transition-metal nitrides (or oxy-nitrides) to replace the carbon black in a fuel cell as the catalyst support.

Although nitrides are kinetically stable at room temperature, thermodynamically, they form oxides. If the metals in the nitride are not in their highest oxidation state, they can form conductive nitride materials, notably TiN, which has many industrial applications, including as protective coatings for tools. TiN's conductivity and its durability made it an interesting choice as one of three metals to be included in a ternary spread. Although we have studied Ta-Ti-Al-N (see above) in the greatest detail, we have studied other systems. Many of the metals were chosen for these other compositions spreads because they formed stable, conductive nitrides, such as vanadium, and niobium. Chromium was chosen because of the glassy oxide that it can form (and is what makes steel "stainless"), which we hoped would have a protective effect on the underlying nitride.[39,40]

3.3 Using conductive-probe AFM to screen nitride composition spreads

(This section represents conductive-probe AFM work done by Dr. James O'Dea.)

When evaluating potential catalyst supports, conductivity was an important characteristic to screen in order to reduce ohmic losses in the resulting fuel cell. Nitrides have been proposed for catalyst supports for this very reason: their conductivity—especially compared to oxides— and mechanical durability (see above). Because sputter deposition could be used to quickly generate a great number of compositions (see above), it was also helpful to have a way to quickly evaluate the relevant properties of catalyst support applications to prevent a backlog of samples. Because the compositions were generated as thin films, however, the analytical methods traditionally used for nanoparticles were generally not applicable.

For nanoparticles, four-point probe measurements would typically be used to evaluate conductivity. The films had a thin (approximately 2 nm) oxide shell [1]which could be punctured by the probes, and, instead of probing the entire thickness of the film, only looked at the interior nitride. Because only the interior nitrides was probed, then, the four-point probe data did not correlate to actual conductivity of the film as it was seen by the electrochemical solution. Four-point probe measurements also provided us with measurements with less-resolved composition-conductivity information. As a result, we sought an alternative: a method to probe the conductivity of these films, and with help of Dr. James O'Dea decided on conductive-probe AFM (cp-AFM), as it allowed for analysis of the surface conductivity, which was relevant for catalyst support applications, as any chemistry in those systems would be occurring on the surface of the nitride.

Cp-AFM involved the generation of a current map. This was done by scanning a Pt-coated AFM tip (in contact mode, with constant force) over the surface of the film while providing a small bias (50 mV) to the substrate. This allowed current to flow and generated a current-map. The current could be loosely correlated to the conductivity of the sample, where areas with greater current corresponded to areas with greater conductivity.[41] The raster allowed for spatial resolution of the conductivity, and, because in the sputtered films, the spatial orientation was related to the composition, we were, therefore, able to get composition-dependent conductivity data from the cp-AFM.

Before electrochemical testing, compositions were initially screened using

cp-AFM. Beyond the work detailed above, we examined a few other composition spreads by cp-AFM with different nitrided elements. Because Nb was known to have a stable and conductive nitride,[42,43] we used it in a couple different composition spreads: Ta-Ti-Nb-N and Cr-Ti-Nb-N. Fig. 3.9a shows the sixteen different current-maps on the Ta-Ti-Nb-N wafer. Despite the conductive oxide of Nb, the Nb-rich regions of the quaternary spread showed that initially the Nb-rich regions had areas that passed the least current of any of the film. After sitting in air for one week (Fig. 3.9b) there was an overall decrease in the currents, particularly notable in the Nb-rich regions, again, although an entire line of cp-AFM images seemed to have lower currents in this area. Even so, the Nb-rich regions had the most dark-blue in the images, corresponding to the least current passed. Similarly, in Fig. 3.10, the Nb-rich areas of the Cr-Ti-Nb-N film passed the least current.

The Ta-rich compositions in both cases also passed less current than the Ti-rich, likely because its surface oxides were very insulating compared to TiO_2 or TiO_xN_y. The lower current observed in the Ti-rich composition space was consistent with work on Ta-Ti-Al-N, discussed below in the manuscript. Because of the overall poor conductivity, this material was not studied beyond its electrochemistry.

Another element of interest for these nitride composition spreads was Cr, as it can not only form a stable nitride,[39,40] but it is also known to form a passivating, protecting layer used in some types of stainless steel.[44,45] A couple Cr compositions were studied—Cr-Ti-Nb-N and Al-Ti-Cr-N.

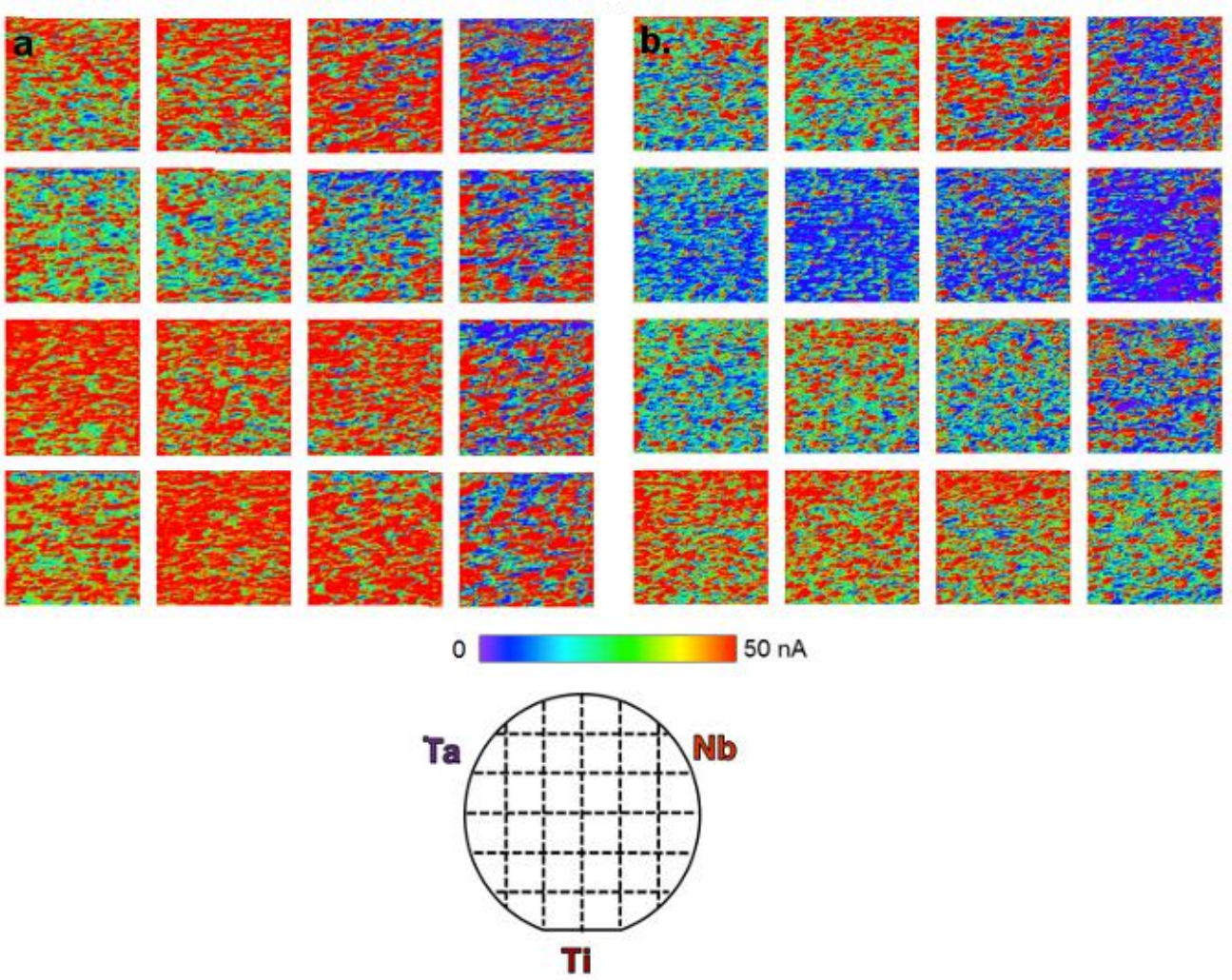

Figure 3.9. Conductive-probe AFM data for the Ta-Ti-Nb-N composition spread, a. after deposition, and b. after exposure to air for 1 week. The mocked-up wafer at the bottom shows where the cp-AFM images are on the wafer.

The cp-AFM data for Cr-Ti-Nb-N are shown in Fig. 3.10. Aside from the Nb-rich areas of the film as mentioned above, the rest of the film was relatively uniform with respect to the amount of current passed. Both the Ti- and Cr-rich

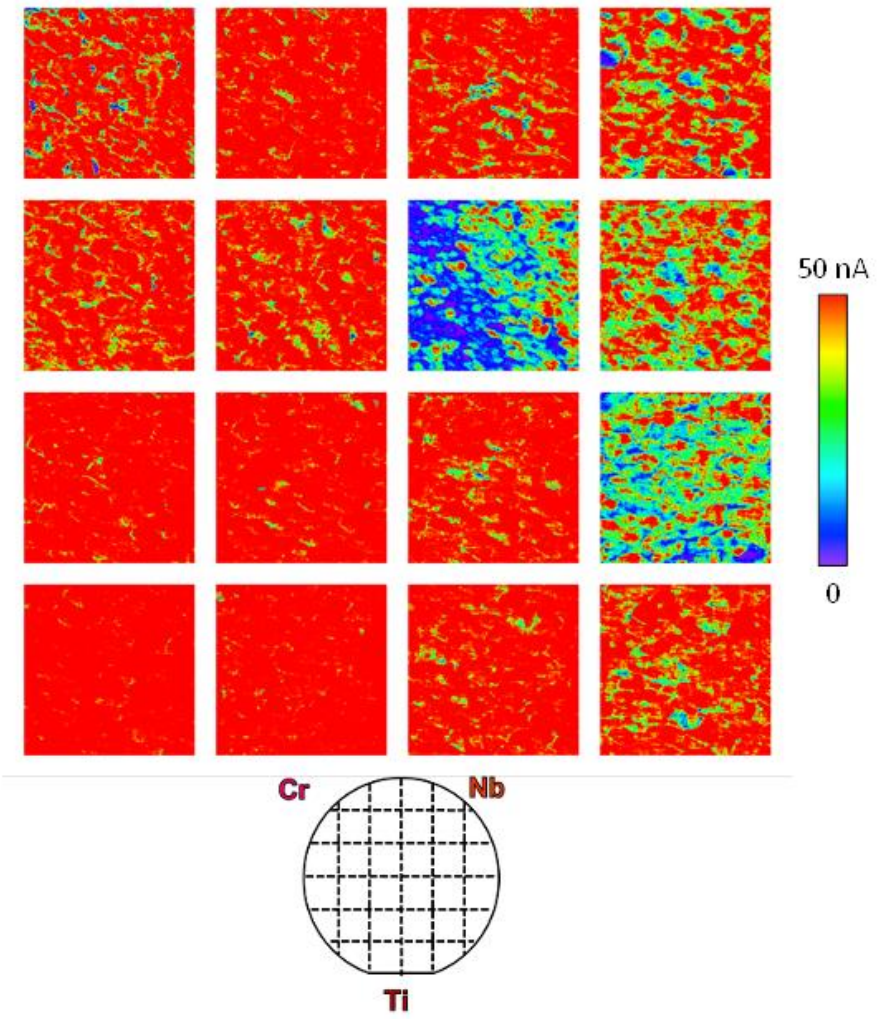

Figure 3.10. Cp-AFM data for a Cr-Ti-Nb-N composition spread.

areas of the film were very conductive, with little discernible differences between them. In Fig. 3.11, on the other hand, which shows the composition spread of Al-Ti-Cr-N, we saw a much larger disparity between the conductivity

performance from the Ti to the Cr, probably as a result of the addition of Al, which, previously, was shown to be the most insulating of the three metal nitrides of the quaternary composition. Examining the lower left and right

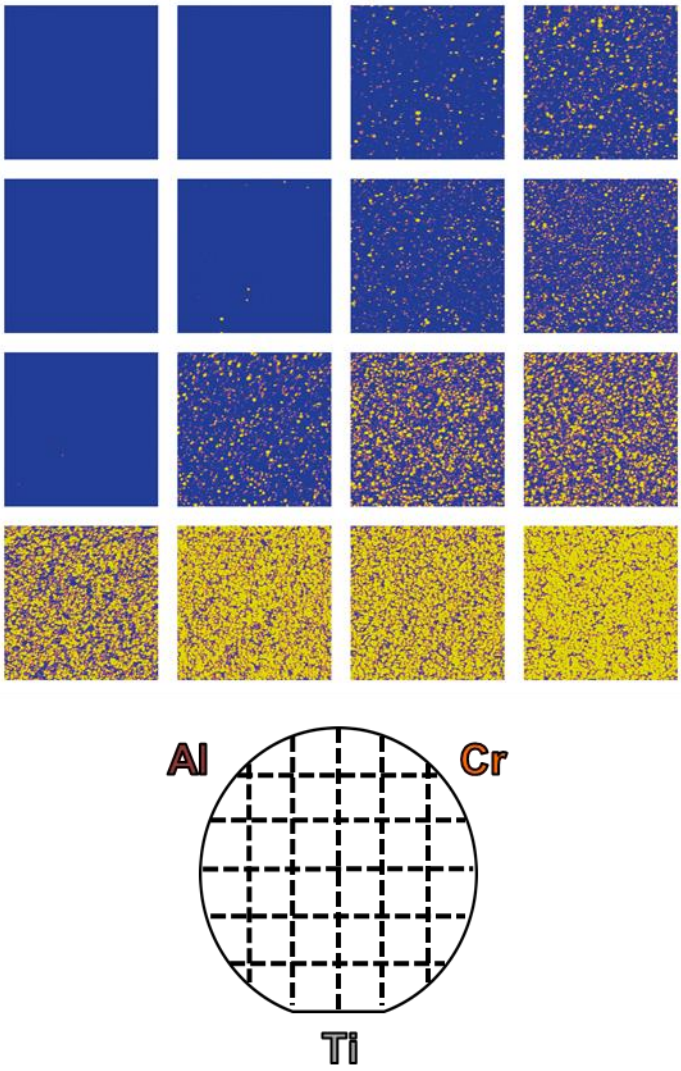

Figure 3.11. The cp-AFM images for Al-Ti-Cr-N.

corners, which should correspond to the same fraction of Ti, but with more Al on the left, and with more Cr on the right, the right side showed significantly more current being passed.

3.4 Electrochemical characterization of the nitride thin films

In order to achieve conditions closer to those found in a fuel cell, we determined the electrochemical responses of the thin films in acidic solution, as described above in the Experimental section.

3.4.1 Cyclic voltammetry of Ta-Ti-Nb-N, Cr-Ti-Nb-N, and Al-Ti-Cr-N

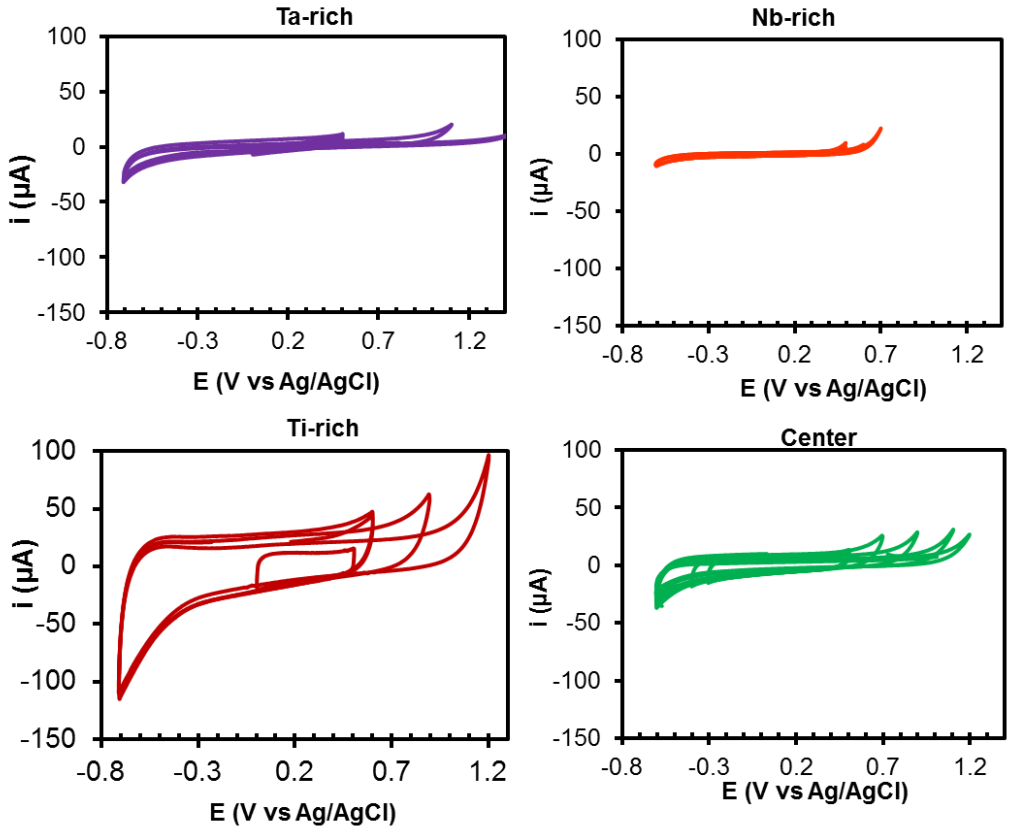

Figure 3.12. The window-opening CVs of Ta-Ti-Nb-N in 0.1 M H_2SO_4, ν = 50 mV/s, 0.1 M H_2SO_4.

Similar to the cp-AFM data shown in Fig. 3.9, the electrochemistry showed responses that were quite dependent on composition. The Ta-rich composition had a very wide stable potential range, and although the currents were small, indicating a low electrochemical surface area (ECSA), the data did not display much of a resistive response. The center, along with the Ti-rich compositions, seemed to have more oxidative current than the Ta-rich, but their ECSAs were also likely to be higher, particularly in the case of the Ti-rich, which showed the largest double-layer current. The Nb-rich region of the film,

however, showed a comparatively narrow potential range, as well as a resistive, canted CV. Although it might be difficult to see in Fig. 3.12 because all the CVs are plotted on the same scale, as the film was cycled to more oxidizing potentials, the slope of the CV increased, indicating that the film was probably oxidizing significantly enough to make it more resistive. Considering that the Nb-rich areas of the film in Fig. 3.9 showed the greatest drop in current from the current maps after just sitting in air for a week, this was an unsurprising result.

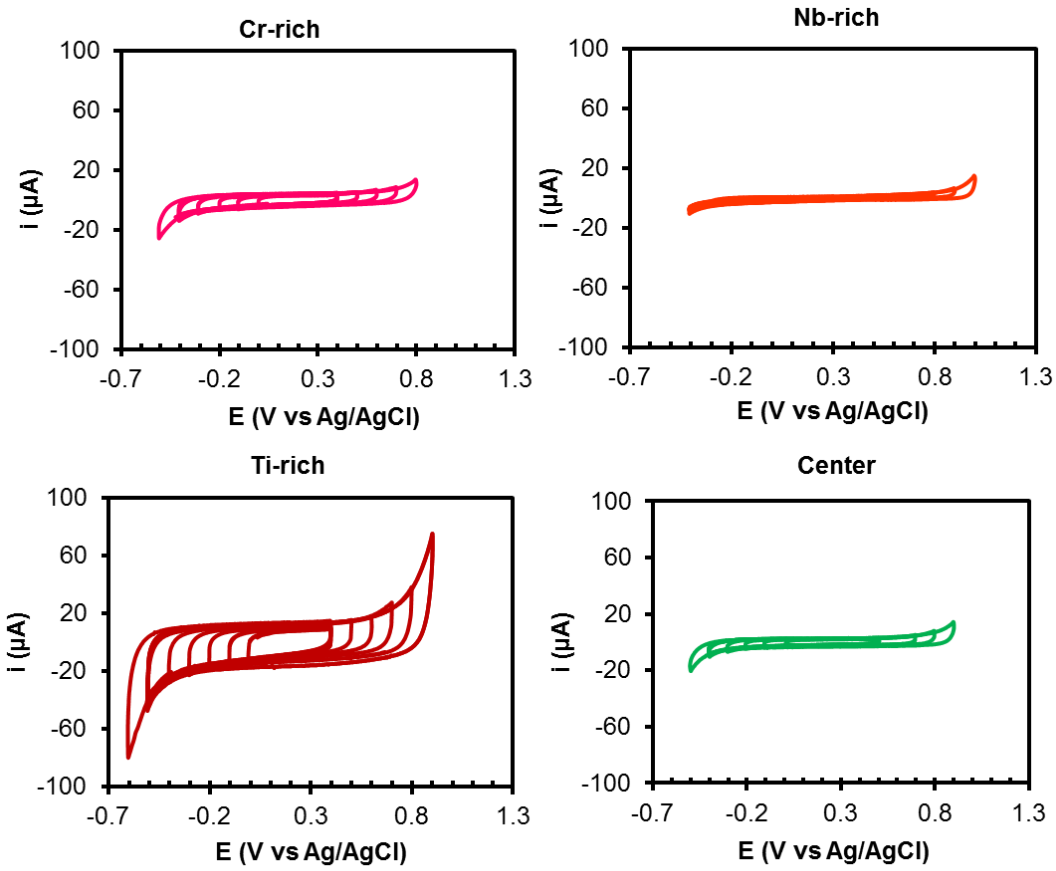

Figure 3.13. The window-opening CVs of Cr-Ti-Nb-N in 0.1 M H_2SO_4, ν = 50 mV/s

The Nb-rich area of the Cr-Ti-Nb-N did not show the same electrochemical response (Fig. 3.13) as in Ta-Ti-Nb-N: it had a wider stable potential window, and although the ECSA was clearly low, the CV was not as canted, and did not seem to shift over time, unlike the Nb-rich region of the Ta-Ti-Nb-N. From these observations, the film probably oxidized but also passivated. Aside from the Nb-rich areas of the Cr-Ti-Nb-N, the remaining three tested areas displayed more favorable electrochemistry. All seemed to have bigger ECSA's than the Nb, especially the Ti, which we saw with other composition spreads, as well. The center composition and Cr-rich showed very similar voltammetric profiles, although the Cr-rich had slightly larger double-layer current. This composition did have promising initial electrochemical properties, and it might be an interesting future research direction for this project.

The electrochemistry for the Al-Ti-Cr-N film (Fig. 3.14), on the other hand, generally looked very resistive, with the exception of the center composition. Even the Ti-rich area of the film looked resistive, and for the other films tested, the Ti-rich areas always had favorable properties. Although the Ti-rich are of the film did have a higher ECSA than the other compositions, it also looked more resistive. Even the Cr-rich, which passed very little current, had a noticeable slant, indicating that that area of the film was very resistive. The overall greater resistance in the different areas of these films can probably be attributed to the inclusion of Al, as not only is Al_2O_3 insulating, but so is AlN.[18] The Al-rich area of the Ta-Ti-Al-N film discussed below was also

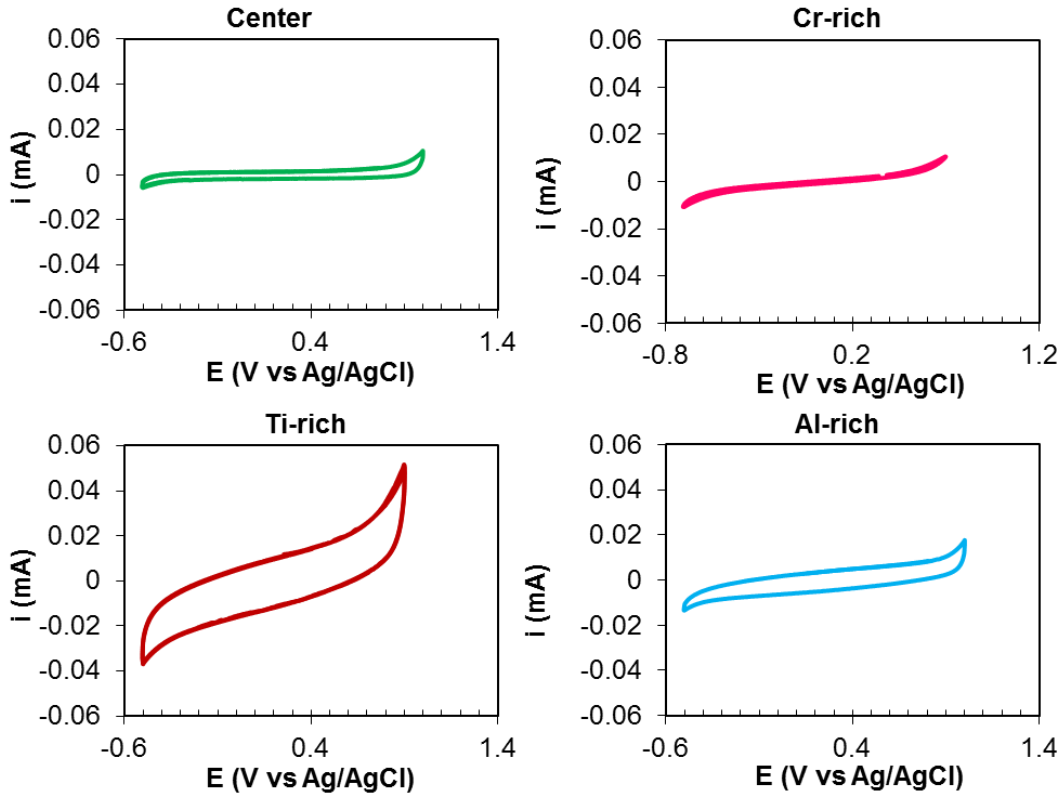

Figure 3.14. The window-opening CVs of AlTiCrN in 0.1 M H_2SO_4, ν = 50 mV/s

resistive. Because of the high apparent resistance of this film, this composition was not considered to be a good candidate for further study.

3.4.2 Methanol oxidation testing of Ta-Ti-Al-N

All of the electrochemistry figures shown above and below used solutions that were not deoxygenated. Even so, we saw no evidence of oxygen reduction occurring in these films. We, therefore, assumed that the nitrides are not capable of performing oxygen reduction, though we tested for methanol oxidation activity. Using a 1 M MeOH solution in 0.1 M H_2SO_4, we cycled each

of the four test compositions and compared them to the same composition without MeOH. The results are shown in Fig. 3.15, which showed that there were very few changes in the CV when MeOH was added. Many of the cycles in solutions with methanol actually seemed to have less oxidation current than the sulfuric acid scans, probably due to the fact that the sulfuric acid cycles were

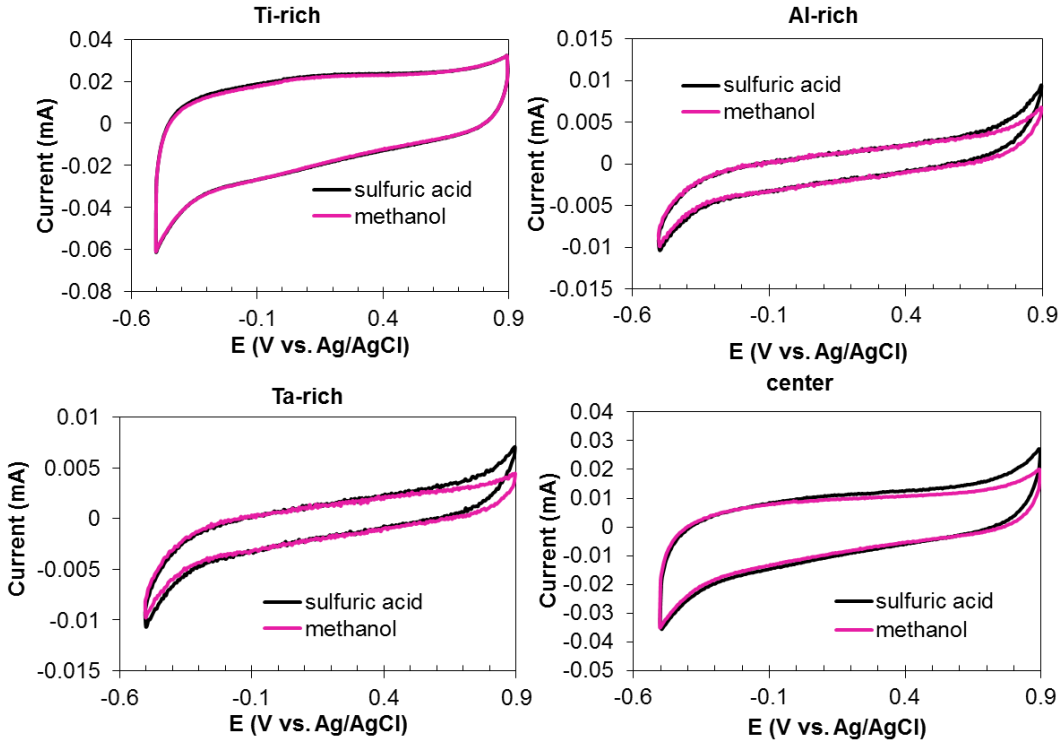

Figure 3.15. CVs of each composition tested in 0.1 M H_2SO_4 and in a mixture of 0.1 M H_2SO_4 and 1.0 M MeOH. ν = 50 mV/s

recorded first, and the passivating oxide layer was formed, whereas by the time we had begun the methanol oxidation cycles, the oxide layer had already formed.

Because the nitrides were intended as catalyst supports for Pt fuel cell catalysts, however, we decided to examine the methanol oxidation of a thin (2.5

nm) Pt film deposited on the nitride composition using gun 4 (i.e. the center gun of the 4-gun assembly) in Tubby. As such, the Pt film was not uniform across the film. Fig. 3.16 shows the first scan of each spot in a MeOH solution. The current for each of the Pt-covered nitrides was lower than the continuous Pt film, shown for reference. This was expected, considering that the Pt film on the nitrides was very thin initially, and on the outside edges of the film where much of the electrochemistry was recorded, the Pt film there was even thinner. Even so, the Pt-covered Ti-rich area of the film performed well, with a maximum current about 50% that of the Pt film. Examining the E_{onset} also showed that while none of the Pt-covered nitrides performed as well as Pt, the Ti-rich area still had the best performance as well. The Al-rich area of the film performed the worst, with respect to both its E_{onset} and its maximum current. The mixed or center composition and the Ta-rich areas performed comparably in both metrics.

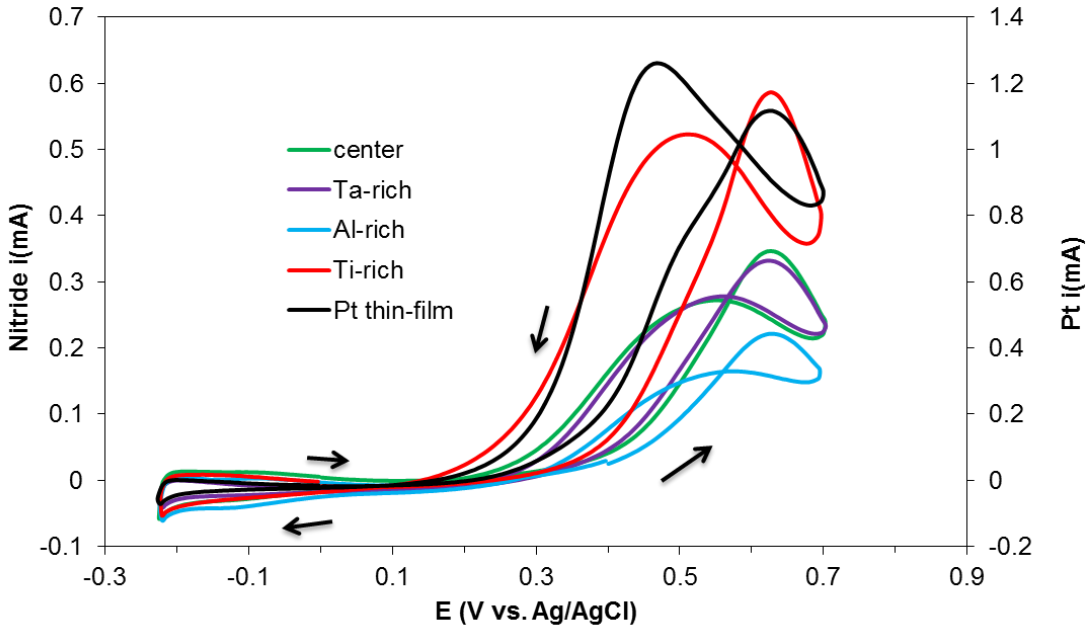

Figure 3.16. First scan of each composition with 2.5 nm thick Pt film in MeOH solution. A separate, 50 nm thick Pt film is shown for comparison. 0.1 M H_2SO_4 and 1.0 M MeOH. ν = 50 mV/s

After determining that Pt deposited on the nitride would indeed oxidize MeOH, we wanted to see how the catalysts would hold up over repeated electrochemical cycling in the presence of MeOH. Pt catalysts can be poisoned by CO, one of the reaction intermediates and products of incomplete MeOH oxidation. CO bonds very strongly to the Pt surface, resulting in fewer available Pt sites where catalysis can take place. Over time, therefore, the oxidation

current will drop. We saw this drop in Fig. 3.17a, which showed the maximum anodic current for each composition tested as a function of scan number. Pt started and ended with the highest currents, but its drop in current was also much more significant than the other compositions tested. Looking at Fig. 3.17a can make that difficult to see, especially as the currents of the Pt/nitride films are much less, so the currents were each normalized in Fig. 3.17b to facilitate comparison between them. Pt showed the steepest initial decline in the current, dropping about 25% in around 5 cycles, although at that point, the current

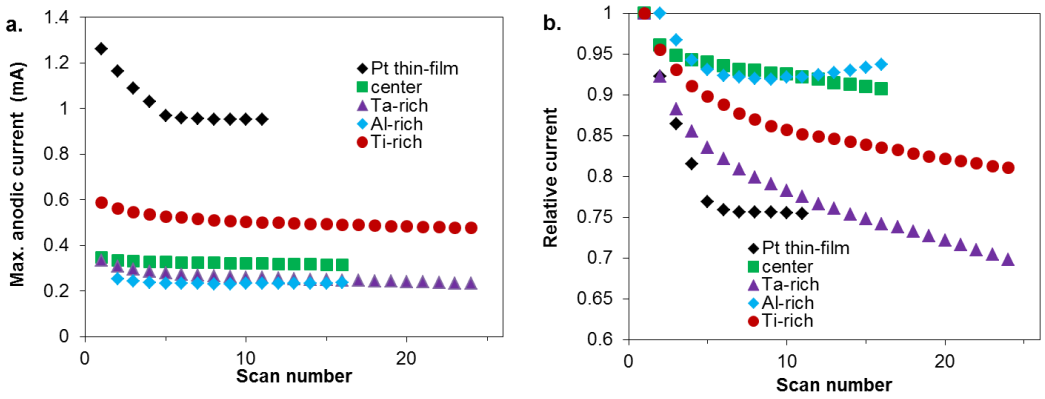

Figure 3.17 a.) The current as a function of scan number for the different films tested and b.) the normalized currents for the same experiments. 0.1 M H_2SO_4, 1.0 M MeOH, ν = 50 mV/s

remained constant. The drop for the nitride compositions tended to be more gradual, with the exceptions of the Al-rich composition, which dropped about 7% within a few cycles but then stayed relatively constant. The Ti-rich, Ta-rich, and center compositions all declined more slowly over time, with the Ta-rich seeing the largest decline in current. We should note, however, that unlike the Pt, the currents of these three compositions did not seem to stabilize over the

course of 26 cycles, so over time, they may drop below Pt, or at the very least, end up at the same current with Pt. Because the amount of Pt on the nitride was less than that of the pure Pt film, perhaps less CO was generated, which may have caused the poisoning process to take longer. While none of these supports then seemed to act as a co-catalyst with Pt to give them superior properties to Pt, it was possible that they could help mitigate CO poisoning, although more experiments would be needed to state this with any certainty.

3.5 Future directions for the nitride project

The next logical step in the nitride work was to make nanoparticles of the compositions. This work has been done by Ryo Wakabayashi, and is discussed in his dissertation and manuscript. Although I believe that this project has reached a logical conclusion with his work (and with the lackluster performance of most of the other nitrides that we tested). If continuation of this project were desired, I believe that the Cr-Ti-Nb-N spread had some interesting areas, particularly in a Nb-poor composition. The ternary Cr-Ti-N may also have interesting properties.

3. 6 Acknowledgements

This work was supported by the Energy Materials Center at Cornell (emc^2), an Energy Frontier Research Center funded by the U.S. Department of Energy, Office of Science, Office of Basic Energy Sciences (DESC0001086). This work made use of the Cornell Center for Materials Research Shared Facilities, which is supported through

the NSF MRSEC program (DMR-1120296).

3.7 References

(1) O'Dea, J. R.; Holtz, M. E.; Legard, A. E.; Young, S. D.; Burns, R. G.; Van Wassen, A. R.; Muller, D. A.; Abruña, H. D.; DiSalvo, F. J.; van Dover, R. B.; et al. Conductivity and Microstructure of Combinatorially Sputter-Deposited Ta-Ti-Al Nitride Thin Films. *Chem. Mater.* **2015**.

(2) Liu, Z. Y.; Zhang, J. L.; Yu, P. T.; Zhang, J. X.; Makharia, R.; More, K. L.; Stach, E. A. Transmission Electron Microscopy Observation of Corrosion Behaviors of Platinized Carbon Blacks under Thermal and Electrochemical Conditions. *J. Electrochem. Soc.* **2010**, *157* (6), B906–B913.

(3) Reiser, C. A.; Bregoli, L.; Patterson, T. W.; Yi, J. S.; Yang, J. D.; Perry, M. L.; Jarvi, T. D. A Reverse-Current Decay Mechanism for Fuel Cells. *Electrochem. Solid-State Lett.* **2005**, *8* (6), A273–A276.

(4) Ohnishi, R.; Katayama, M.; Cha, D.; Takanabe, K.; Kubota, J.; Domen, K. Titanium Nitride Nanoparticle Electrocatalysts for Oxygen Reduction Reaction in Alkaline Solution. *J. Electrochem. Soc.* **2013**, *160* (6), F501–F506.

(5) Gancs, L.; Kobayashi, T.; Debe, M. K.; Atanasoski, R.; Wieckowski, A. Crystallographic Characteristics of Nanostructured Thin-Film Fuel Cell Electrocatalysts: A HRTEM Study. *Chem. Mater.* **2008**, *20* (7), 2444–2454.

(6) Debe, M. K.; Schmoeckel, A. K.; Vernstrom, G. D.; Atanasoski, R. High Voltage Stability of Nanostructured Thin Film Catalysts for PEM Fuel Cells. *J. Power Sources* **2006**, *161* (2), 1002–1011.

(7) Yang, X. G.; Wang, C. Y. Nanostructured Tungsten Carbide Catalysts for Polymer Electrolyte Fuel Cells. *Appl. Phys. Lett.* **2005**, *86* (22), 224104.

(8) Ganesan, R.; Lee, J. S. Tungsten Carbide Microspheres as a Noble-Metal-Economic Electrocatalyst for Methanol Oxidation. *Angew. Chem. Int. Ed.* **2005**, *44* (40), 6557–6560.

(9) Nie, M.; Shen, P. K.; Wu, M.; Wei, Z.; Meng, H. A Study of Oxygen Reduction on Improved Pt-WC/C Electrocatalysts. *J. Power Sources* **2006**, *162* (1), 173–176.

(10) Subban, C. V.; Zhou, Q.; Hu, A.; Moylan, T. E.; Wagner, F. T.; DiSalvo, F. J. Sol−Gel Synthesis, Electrochemical Characterization, and Stability Testing of Ti0.7W0.3O2 Nanoparticles for Catalyst Support Applications in Proton-

Exchange Membrane Fuel Cells. *J. Am. Chem. Soc.* **2010**, *132* (49), 17531–17536.

(11) Zhang, P.; Huang, S.-Y.; Popov, B. N. Mesoporous Tin Oxide as an Oxidation-Resistant Catalyst Support for Proton Exchange Membrane Fuel Cells. *J. Electrochem. Soc.* **2010**, *157* (8), B1163–B1172.

(12) Bonakdarpour, A.; Tucker, R. T.; Fleischauer, M. D.; Beckers, N. A.; Brett, M. J.; Wilkinson, D. P. Nanopillar Niobium Oxides as Support Structures for Oxygen Reduction Electrocatalysts. *Electrochimica Acta* **2012**, *85*, 492–500.

(13) Kakinuma, K.; Wakasugi, Y.; Uchida, M.; Kamino, T.; Uchida, H.; Deki, S.; Watanabe, M. Preparation of Titanium Nitride-Supported Platinum Catalysts with Well Controlled Morphology and Their Properties Relevant to Polymer Electrolyte Fuel Cells. *Electrochimica Acta* **2012**, *77*, 279–284.

(14) Avasarala, B.; Murray, T.; Li, W.; Haldar, P. Titanium Nitride Nanoparticles Based Electrocatalysts for Proton Exchange Membrane Fuel Cells. *J. Mater. Chem.* **2009**, *19* (13), 1803–1805.

(15) Halalay, I. C.; Merzouqui, B.; Carpenter, M. K.; Swathirajan, S.; Garabedian, G. C.; Mance., A. M.; Cai, M. Supports for Fuel Cell Catalysts. U.S. Patent 7,622,216, November 24, 2009.

(16) Choi, D.; Kumta, P. N. Synthesis, Structure, and Electrochemical Characterization of Nanocrystalline Tantalum and Tungsten Nitrides. *J. Am. Ceram. Soc.* **2007**, *90* (10), 3113–3120.

(17) Yang, M.; Van Wassen, A. R.; Guarecuco, R.; Abruña, H. D.; DiSalvo, F. J. Nano-Structured Ternary Niobium Titanium Nitrides as Durable Non-Carbon Supports for Oxygen Reduction Reaction. *Chem. Commun.* **2013**, *49* (92), 10853–10855.

(18) Vacandio, F.; Massiani, Y.; Gravier, P.; Rossi, S.; Bonora, P. L.; Fedrizzi, L. Improvement of the Electrochemical Behaviour of AlN Films Produced by Reactive Sputtering Using Various under-Layers. *Electrochimica Acta* **2001**, *46* (24), 3827–3834.

(19) Dimitrova, V.; Manova, D.; Djulgerova, R. Element Composition and Electrochemical Behaviour of Polycrystalline AlN Thin Films. *Surf. Coat. Technol.* **2000**, *123* (1), 12–16.

(20) Cui, Z.; Burns, R. G.; DiSalvo, F. J. Mesoporous $Ti_{0.5}Nb_{0.5}N$ Ternary Nitride as a Novel Noncarbon Support for Oxygen Reduction Reaction in Acid and Alkaline Electrolytes. *Chem. Mater.* **2013**, *25* (19), 3782–3784.

(21) Youn, D. H.; Bae, G. H.; Han, S.; Kim, J. Y.; Jang, J.-W.; Park, H.; Choi, S. H.; Lee, J. S. A Highly Efficient Transition Metal Nitride-Based Electrocatalyst for Oxygen Reduction reaction:TiN on CNT-Graphene Hybrid Support. *J. Mater. Chem. A* **2013**, No. 1, 8007–8015.

(22) Gallagher, P. K.; Sinclair, W. R.; Bacon, D. D.; Kammlott, G. W. Oxidation of Sputtered Niobium Nitride Films. *J. Electrochem. Soc.* **1983**, *130* (10), 2054–2056.

(23) Frankenthal, R. P.; Siconolfi, D. J.; Sinclair, W. R.; Bacon, D. D. Thermal Oxidation of Niobium Nitride Films at Temperatures from 20°–400°C I . The Surface Reaction. *J. Electrochem. Soc.* **1983**, *130* (10), 2056–2060.

(24) Qi, Z.; Kaufman, A. Low Pt Loading High Performance Cathodes for PEM Fuel Cells. *J. Power Sources* **2003**, *113* (1), 37–43.

(25) Milošv, I.; Strehblow, H.-H.; Navinšek, B.; Metikoš-Huković, M. Electrochemical and Thermal Oxidation of TiN Coatings Studied by XPS. *Surf. Interface Anal.* **1995**, *23* (7-8), 529–539.

(26) Brady, D. P.; Fuss, F. N.; Gerstenberg, D. Thermal Oxidation and Resistivity of Tantalum Nitride Films. *Thin Solid Films* **1980**, *66* (3), 287–302.

(27) Dutta, I.; Mitra, S.; Rabenberg, L. Oxidation of Sintered Aluminum Nitride at Near-Ambient Temperatures. *J. Am. Ceram. Soc.* **1992**, *75* (11), 3149–3153.

(28) Souto, R. M.; Alanyali, H. Electrochemical Characteristics of Steel Coated with TiN and TiAlN Coatings. *Corros. Sci.* **2000**, *42* (12), 2201–2211.

(29) Francis, R. W.; Worrell, W. L. High Temperature Electrical Conductivity of Aluminum Nitride. *J. Electrochem. Soc.* **1976**, *123* (3), 430–433.

(30) Taylor, K. M.; Lenie, C. Some Properties of Aluminum Nitride. *J. Electrochem. Soc.* **1960**, *107* (4), 308–314.

(31) Grips, V. K. W.; Ezhil Selvi, V.; Barshilia, H. C.; Rajam, K. S. Effect of Electroless Nickel Interlayer on the Electrochemical Behavior of Single Layer CrN, TiN, TiAlN Coatings and Nanolayered TiAlN/CrN Multilayer Coatings Prepared by Reactive Dc Magnetron Sputtering. *Electrochimica Acta* **2006**, *51* (17), 3461–3468.

(32) William Grips, V. K.; Barshilia, H. C.; Selvi, V. E.; Kalavati; Rajam, K. S. Electrochemical Behavior of Single Layer CrN, TiN, TiAlN Coatings and Nanolayered TiAlN/CrN Multilayer Coatings Prepared by Reactive Direct Current Magnetron Sputtering. *Thin Solid Films* **2006**, *514* (1-2), 204–211.

(33) Pfeiler, M.; Fontalvo, G. A.; Wagner, J.; Kutschej, K.; Penoy, M.; Michotte, C.; Mitterer, C.; Kathrein, M. Arc Evaporation of Ti–Al–Ta–N Coatings: The Effect of Bias Voltage and Ta on High-Temperature Tribological Properties. *Tribol. Lett.* **2008**, *30* (2), 91–97.

(34) Pfeiler, M.; Scheu, C.; Hutter, H.; Schnöller, J.; Michotte, C.; Mitterer, C.; Kathrein, M. On the Effect of Ta on Improved Oxidation Resistance of Ti–Al–Ta–N Coatings. *J. Vac. Sci. Technol. A* **2009**, *27* (3), 554–560.

(35) Willmott, D. J. Effect of Nitrogen on the Electrical and Structural Properties of Triode-sputtered Tantalum Films. *J. Appl. Phys.* **1972**, *43* (12), 4865–4871.

(36) Riekkinen, T.; Molarius, J.; Laurila, T.; Nurmela, A.; Suni, I.; Kivilahti, J. K. Reactive Sputter Deposition and Properties of TaxN Thin Films. *Microelectron. Eng.* **2002**, *64* (1–4), 289–297.

(37) Gregoire, J. M.; Dover, R. B. van; Jin, J.; DiSalvo, F. J.; Abruña, H. D. Getter Sputtering System for High-Throughput Fabrication of Composition Spreads. *Rev. Sci. Instrum.* **2007**, *78* (7), 072212.

(38) Gregoire, J. M.; Tague, M. E.; Cahen, S.; Khan, S.; Abruña, H. D.; DiSalvo, F. J.; van Dover, R. B. Improved Fuel Cell Oxidation Catalysis in Pt1−xTax†. *Chem. Mater.* **2010**, *22* (3), 1080–1087.

(39) Chiba, Y.; Omura, T.; Ichimura, H. Wear Resistance of Arc Ion-Plated Chromium Nitride Coatings. *J. Mater. Res.* **1993**, *8* (05), 1109–1115.

(40) Ehiasarian, A. P.; Hovsepian, P. E.; Hultman, L.; Helmersson, U. Comparison of Microstructure and Mechanical Properties of Chromium Nitride-Based Coatings Deposited by High Power Impulse Magnetron Sputtering and by the Combined Steered Cathodic Arc/unbalanced Magnetron Technique. *Thin Solid Films* **2004**, *457* (2), 270–277.

(41) Burns, R. G. Materials for Energy: Complex Oxides and Nitrides for New Polymer Electrolyte Membrane Fuel Cell Catalysts and Supports. Ph.D., Cornell University: United States -- New York, 2013.

(42) Orilall, M. C.; Matsumoto, F.; Zhou, Q.; Sai, H.; Abruña, H. D.; DiSalvo, F. J.; Wiesner, U. One-Pot Synthesis of Platinum-Based Nanoparticles Incorporated into Mesoporous Niobium Oxide−Carbon Composites for Fuel Cell Electrodes. *J. Am. Chem. Soc.* **2009**, *131* (26), 9389–9395.

(43) Yang, M.; Van Wassen, A. R.; Guarecuco, R.; Abruña, H. D.; DiSalvo, F. J. Nano-Structured Ternary Niobium Titanium Nitrides as Durable Non-Carbon Supports for Oxygen Reduction Reaction. *Chem. Commun.* **2013**, *49* (92), 10853–10855.

(44) Brooks, A. R.; Clayton, C. R.; Doss, K.; Lu, Y. C. On the Role of Cr in the Passivity of Stainless Steel. *J. Electrochem. Soc.* **1986**, *133* (12), 2459–2464.

(45) Olsson, C.-O. A.; Landolt, D. Passive Films on Stainless Steels—chemistry, Structure and Growth. *Electrochimica Acta* **2003**, *48* (9), 1093–1104.

CHAPTER 4

A COMPARISON OF ACIDIC AND ALKALINE OXYGEN REDUTION ACTIVITY AT BULK METALS

Work in this chapter was done in collaboration with Dr. David Finkelstein and Dr. Eric Rus.

4.1 Introduction

With slow kinetics and a high overpotential, the oxygen reduction reaction (ORR) continues to be a hindrance to the widespread deployment of fuel cells, particularly with the current standard of costly Pt and Pt-alloys as the catalysts. As such, there is a great deal of research on ways to improve ORR catalysts and maximize Pt use. Traditionally, this approach has been to reduce the cost of the cathode by alloying the Pt with another, less expensive metal such as Ni[1,2] or Co[2,3], reducing the amount of Pt in the cathode.

Acidic fuel cells have been traditionally used because of the development of Nafion as a proton exchange membrane. With the recent development of anion exchange membranes, however, alkaline fuel cells now seem like a feasible alternative.[4–6] Alkaline fuel cells offer some promising advantages over their acidic counterparts. Under alkaline conditions, water generated at the cathode moves to the anode, reducing fuel crossover, a problem with PEMFC's.[7] In addition to fuel

crossover, metals tend to have poorer stability (more soluble) under acidic conditions. Additionally, some metals have better ORR catalytic activity under alkaline conditions, for example silver, which has been shown to have faster kinetics in alkaline solution.[8] These advantages may be able to overcome the disadvantages associated with alkaline fuel cells, including the adsorption of OH^- on the surface.[9,10]

Various metals have shown promising ORR activity under alkaline conditions. Adzic studied the electrochemical activity of the (111)-crystal face of various metals platinum-group metals (PGM) in 0.1 M NaOH, and found that Ag, Au, Pt, and Pd had the best (lowest) overpotentials for oxygen reduction of the seven metals tested in bulk. Nanoparticles gave almost the same result, with Rh performing slightly better. The low natural abundance of Rh, as well as its high price, however, make it a poor candidate for fuel cell materials. Although this paper examined several metals under the same conditions, the use of single-crystal electrodes seems impractical as a model system for bulk materials for fuel cells, as they are expensive to produce and hard to make on a large scale. Examining bulk, polycrystalline electrodes, then, with a well-defined surface would allow for more quantitative data than using nanoparticles and would provide more relevant information than single-crystal electrodes.

Adzic showed that Au has an onset potential that is about 50 mV less (more positive) than Pt or Pd, and although the current cost of gold exceeds that of Pt and Pd, its price is more volatile. Despite having an onset potential that is about 100 mV more positive than Ag, Au has also been shown to proceed through a 2-electron pathway to H_2O_2 under both acidic and alkaline conditions, with some of the oxygen also

proceeding through a 4-electron pathway to H_2O.[11–13] Because H_2O_2 can lead to membrane degradation, Au alone may not be the best material for fuel cell anodes. It has found success, however, when alloyed with other metals, Pt in particular. PtAu has been used in fuel cells on space shuttles[14,15] and Li-Air batteries.[16]

Pt, the traditional fuel cell catalyst, is expensive, but, under acidic conditions, has fairly facile kinetics as well as good stability. In acidic medium, oxygen reduction at Pt proceeds primarily through a 4-electron pathway to H_2O,[17] but in alkaline medium, the primary mechanism is less clear. Adzic and Lima *et al.* studied nanoparticles and Pt single crystals and saw that not only do the nanoparticles produce some H_2O_2, but that two low-index faces of Pt [(100) and (111)] proceed through a 4-electron mechanism, under at least some conditions.[11,17] Markovic also studied three low-index faces of Pt and saw that Pt(100) and, in particular, (111) produce significant amounts of HO_2^- in 0.1 M KOH, in addition to HO^-.[17] Ramaswamy and Mukerjee also studied the ORR at Pt under alkaline conditions and found that it proceeds through the 2-electron and 4-electron pathways at different potentials, due to differences in inner sphere vs outer sphere mechanisms, with an outer sphere mechanism leading to HO_2^- at low overpotentials, and an inner sphere mechanism leading to OH^- at high overpotentials.[18] They also note that because of this diminished efficiency at low overpotentials and its near-prohibitive cost, Pt is not a catalyst that should be used in alkaline fuel cells.

From Adzic's work in alkaline medium, however, Pd is a reasonable alternative to Pt, both in terms of kinetics and mechanism. Although Pt has slightly

more favorable kinetics, the two are nearly indistinguishable electrochemically, and when the lower cost of Pd is considered, it becomes even more favorable. Both have been shown to produce both OH^- and HO_2^- under alkaline conditions,[19] but Pd has also been shown to yield less HO_2^- than Pt does.[20] Under acidic conditions, compared to single crystalline Pt, Pd(100) has been shown to have a greater current density at 0.90 V, a Department of Energy metric.[21]

Ag, at less than $20/troy oz. is relatively inexpensive, when compared to the cost of metals like Pt and Pd. According to its Pourbaix diagram, however, it shows a limited stability range under acidic, but is quite stable under alkaline conditions.[22] Not only is Ag stable under alkaline conditions but it also primarily produces OH^- instead of HO_2^-, producing only about 3% HO_2^-.[23] Even under acidic conditions, while the O_2 is reduced to HO_2^- at low overpotentials, at higher overpotentials, it proceeds to OH^-. Markovic explains this in terms of the surface coverage of adsorbed oxygen species. Under acidic conditions there are few adsorbed OH^- and the adsorbed O_2 and O_2^- are weakly bound, allowing for the OH^- pathway only at high overpotentials, whereas under alkaline conditions the interaction is stronger, leading to a more facile four-electron pathway. [23] Even so, Markovic only studied Ag(111), and no systematic study has been done on oxygen reduction at bulk, polycrystalline Ag. Not only is Ag more stable under alkaline conditions, but our work shows that there is also a gain in the E_{onset} when moving from acid to base: the onset potential occurs at about 160 mV vs RHE in acid and at about 820 mV vs RHE in base, resulting in a net gain of 660 mV by switching from acidic to alkaline conditions.

One of the benefits of alkaline fuel cells is that they allow the use of some of these other metals in cathodes.[7] Ag may result in an overall larger cell voltage, and Pd offers a more inexpensive alternative to Pt under alkaline conditions. For the anode, even carbon-supported Ni has been shown to have some activity towards methanol oxidation.[24] In a direct methanol fuel cell (DMFC), the methanol kinetics may also be more facile, and the searches or a methanol-tolerant ORR catalyst can begin to prevent poisoning by the residual methanol that is resistant to the electro-osmotic currents.[7] Unfortunately, one of the problems with alkaline fuel cells currently is the anion exchange membrane (AEM). During operation, the AEM may degrade as K_2CO_3 or Na_2CO_3 precipitate in the pores of the membrane, blocking mass transport through it and mechanically destroying the membrane itself.[25]

Electrochemists have studied pure metal catalysts for oxygen reduction in the past, in both acidic and alkaline conditions, but most of these studies were done using single-crystal electrodes or nanoparticles. Although single-crystals have the advantage of well-defined surfaces, they are unlikely to be used in fuel cells because they are difficult to produce in bulk, and faceted nanoparticles rapidly lose their distinct faces with electrochemical cycling.[26] To do a very systematic, reproducible study of catalysts, therefore, a bulk, polycrystalline metal electrode is a sensible choice, because it can be manually polished, requires no carbon support, and no ionomer. It allows for greater consistency between the electrodes, as there will be no issues with electrical contact or resistance with any nanoparticles and the electrode, and when going to a new material, there is no need to worry about differences in ink preparation. Bulk, polycrystalline electrodes may not perfectly replicate the conditions within an

MEA, however, their well-defined surface and surface area allow for a better understanding of what catalytic trends may be occurring because of this greater control of varaibles. Additionally, with a controlled surface, "reaction phase diagrams", in other words, an analog to an experimental Pourbaix diagram, can be constructed to help to look for reactivity trends. These trends may include whether the different processes on a particular metal follow the predicted Nernstian behavior—in other words, shifting by 59 mV for each pH unit (which would also be seen as the potentials at different pHs, when referenced to a pH-corrected reference electrode, such as RHE). In this chapter, we present a survey of the oxygen reduction activity of bulk, polycrystalline metals—platinum, palladium, gold, and silver—under acidic and alkaline conditions.

4.2 Experimental Methods

4.2.1 Electrochemical Setup and Electrode Cleaning

The electrolyte solutions used in this chapter consisted of perchloric acid (0.1 M, JT Baker) and sodium hydroxide (0.1 and 1.0 M, Malinckrodt). All solutions were prepared with deionized water that was purified with a ThermoScientific Barnstead Nanopure system (18.2 MΩ· cm) to prevent metal ion contamination.

Experiments were carried out in a three-chambered electrochemical RDE cell, using a home-built Ag/AgCl reference electrode and a large surface area Pt-mesh counter electrode. A Pine bipotentiostat (Model AFRDE5) and analytical rotor (Model

AFMSRX) were used to perform the rotating disk electrode voltammetry experiments. After electrochemical cleaning, the electrolyte solution was bubbled with O_2 (ultra-high purity, 99.994%, Airgas) while sweeping the potential for 15 minutes, before the experiment began, to saturate it with oxygen. Rotation rates between 50 and 3000 rpm were used, with a greater number of slower rotation rates (where the oxygen reduction reaction was less kinetically limited) used to obtain more accurate Levich plots. The voltage sweeps were carried out at 20 mV/s to decrease the time that oxygen had to escape the solution. Additionally, in between each rotation rate, the solution was again bubbled with oxygen for 6-7 minutes while electrochemically cycling, in order to keep its concentration high.

Electrode pretreatments were unique to each different metal. γ-alumina (0.05 μm particle size) was used with Buehler Microcloth and water to mechanically polish Au, Pd, and Ag. The Pt electrode, instead, was polished with diamond paste (1 μm, Buehler Metadi) and lubricating fluid (Buehler Metadi) on a Microcloth. All electrodes were then cycled electrochemically until their characteristic cyclic voltammetric profiles were achieved. After that, the electrodes were cycled until the CVs stopped changing (no peak or current shifts or changes). Each metal had its own particular potential range, which was also used for the ORR experiments.

4.2.2 Levich Equation

To differentiate between different oxygen reduction mechanisms, rotating disk electrode (RDE) voltammetry can determine the number of electrons involved in a

reaction by using the Levich equation:

$$i_l = -0.62nFAD^{2/3}\omega^{1/2}\nu^{-1/6}C^b$$

where i_l is the limiting current, and n is the number of electrons involved in the reaction. Further variables are: A, or the electrode's geometric surface area (cm^2) (as opposed to the more conventional electrochemical surface area used in CV measurements); D, the diffusion coefficient of the analyte (O_2 here) (cm^2/s); ω, the electrode rotation rate (rad/s), though also used in this and subsequent chapters as rotations per minute (rpm), and C^b is the concentration of the analyte (mol/cm^3). For our analyses of O_2 (aq), we have used the diffusion coefficient for O_2 (aq) of 1.63×10^{-5} cm^2/s for pH = 1. For pH = 14, the diffusion coefficient of O_2 (aq) was 0.80×10^{-5}, and for pH = 13, the value of 1.93×10^{-5} cm^2/s, determined by Blizanac *et al*.[23] Only those rotation rates which reached a mass-transport limited current were used to generate Levich plots, as the Levich equation is not valid under conditions which are not transport-limited.

4.3 Results and Discussion

4.3.1 RDE and RRDE in acid and base

Pt has long been the preferred catalyst for oxygen reduction in fuel cells because of its stability and kinetics. Not only is it stable, but under acidic conditions, Pt reduces O_2 primarily through the 4-electron pathway to H_2O.[17,18] The RDE results obtained for O_2 reduction in an O_2-saturated 0.1 M $HClO_4$ solution (pH 1) are shown in Figure 4.1. From Levich analysis shown in the inset, the reduction proceeds through a $4e^-$ process, consistent with results that have been presented in the literature. Despite the Levich analysis, the increase in current at +0.1 V in Fig. 4.1 (in other words, a decrease in the reduction current) seems to indicate an increasing concentration of

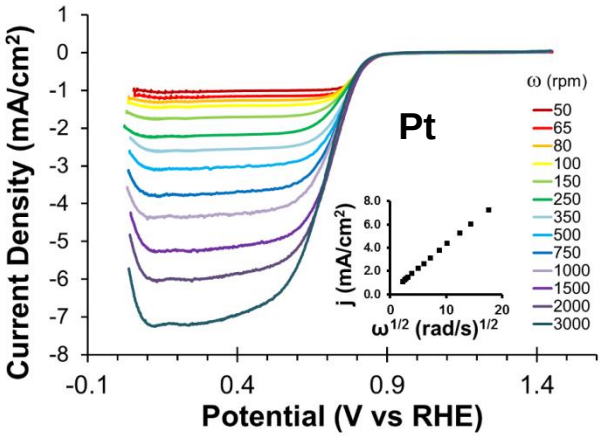

Figure 4.1. RDE negative-going sweeps of O_2-saturated 0.1 M $HClO_4$ at a Pt disk electrode, 20 mV/s, rotated between 50 and 3000 rpm. Inset: Levich plot sampled at E = +0.1 V.

H_2O_2 present in the solution. This is only seen as the experiment progresses, starting at 250 rpm, indicating, along with the Levich analysis, that although reduction to H_2O_2 is not the primary mechanism, it is a minor reaction occurring with the 4-electron

pathway, as also reported by Markovic.[17]

Limiting currents in studies of all four metals were lower in alkaline conditions

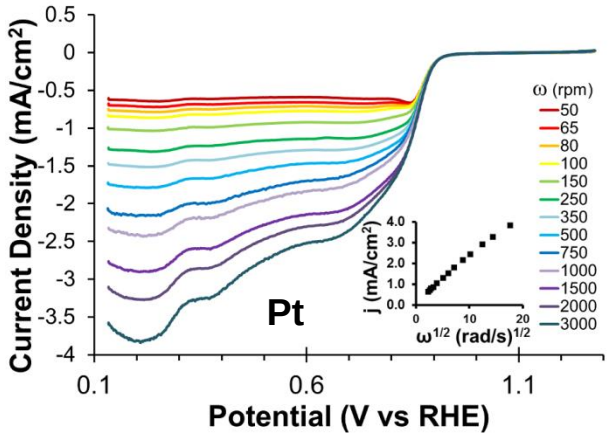

Figure 4.2. RDE negative-going sweeps of O_2-saturated 1.0 M NaOH at a Pt disk electrode, 20 mV/s, rotated between 50 and 3000 rpm. Inset: Levich plot sampled at E = +0.22 V.

than acidic conditions, due to O_2's lower diffusion coefficient in base than in acid. As in $HClO_4$, oxygen reduction in 1.0 M NaOH proceeds through both the 2- and 4-electron mechanisms, although, at comparable rates, leading to electron counts, calculated from Levich plot slopes, that vary from 2.9 to 3.3. These intermediate electron count values indicate that the reaction proceeds through both pathways. Previous work has shown mixed results, with some groups reporting that in alkaline conditions, Pt proceeds entirely through the 4-electron mechanism,[11,27] and some reporting that Pt proceeds through both mechanisms, changing with potential.[18,28] These studies, however, use either single-crystal[11,28] or nanoparticle Pt[18,27] as the electrocatalysts, and therefore may not fully represent the activity of bulk, polycrystalline Pt. Different faces of Pt may have unequal oxygen reduction activity,

with the Pt (111) face producing the most OH^- but also the most HO_2^-. The prevalence of particular faces on a particular polycrystalline sample may affect the resulting Levich slope, contributing to some of the variation in the data seen in the literature.

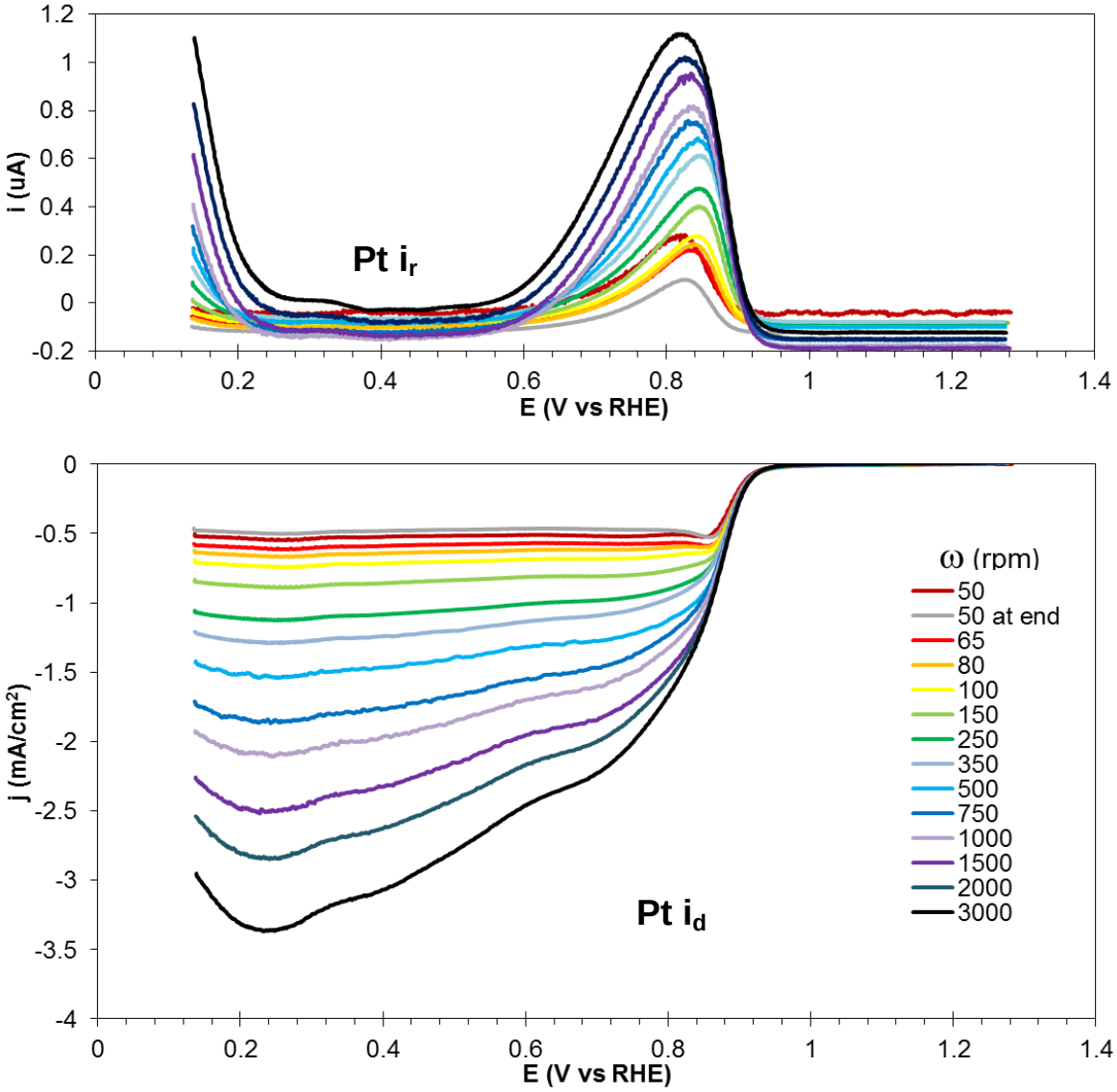

Figure 4.3. RRDE sweeps of O_2-saturated 1.0 M NaOH at a Pt/Pt ring-disk electrode, 20 mV/s, rotated between 50 and 3000 rpm. E_{ring} = 1.12 V

Additionally, the curvature evident at high rotation rates, as seen in the Levich plot in Fig. 4.2, probably caused by oxygen escape at high rotation rates, may contribute to

some variance in the data from the theoretical value. Even so, not all of the slope variations can be attributed to variance, as RRDE data show the clear production of HO_2^- at both low and very high overpotentials (Fig. 4.3).

While Pt has been the preferred ORR catalyst, Au has also been studied.[29] Despite its past use in fuel cells, likely because it is a corrosion-resistant metal and its

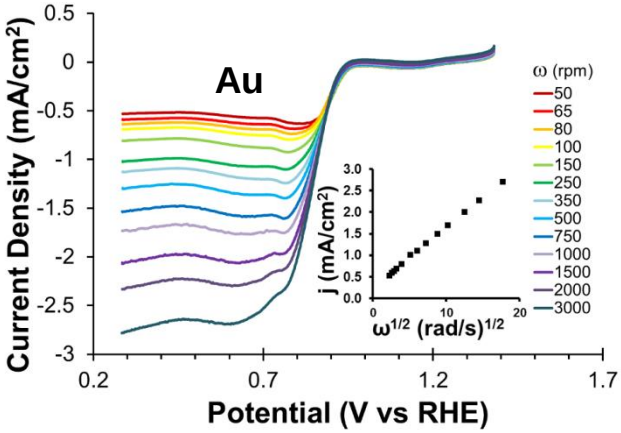

Figure 4.4. RDE negative-going sweeps of O_2-saturated 1.0 M NaOH at an Au disk electrode, 20 mV/s, rotated between 50 and 3000 rpm. Inset: Levich plot sampled at $E = +0.42$ V.

historically lower price relative to Pt, it has rarely been used as an electrocatalyst by itself in a fuel cell. Au's ORR onset potential is not as good as Pt and Pd,[11] but in the past, it has been less expensive than Pt, though that has changed in recent years. Although Au is corrosion-resistant and does reduce oxygen, it does so primarily through the 2-electron pathway,[11–13] meaning that it is less useful as an ORR electrocatalyst. Levich analysis of our RDE data indicate that Au proceeds through a 2-electron mechanism in both acidic and alkaline conditions, as shown in Fig 4.4 and 4.5.

An interesting result from these two RDE experiments is that the onset potential of oxygen reduction at Au does not follow a Nernstian pH shift. In Fig. 4.5,

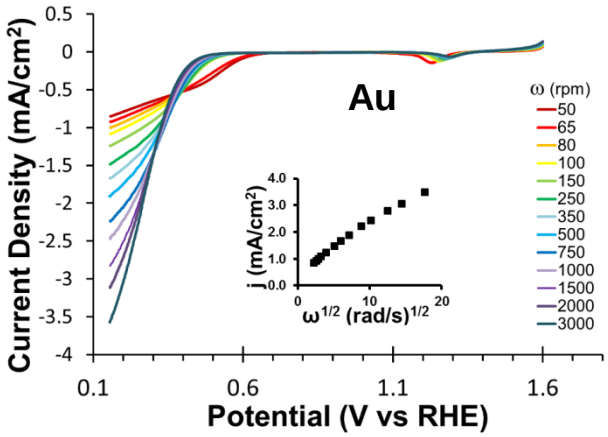

Figure 4.5. RDE negative-going sweeps of O_2-saturated 0.1 M $HClO_4$ at an Au disk electrode, 20 mV/s, rotated between 50 and 3000 rpm. Inset: Levich plot sampled at E = + 0.17 V.

the onset potential is 0.32 V after the initial two rotation rates, which are shifted about +140 mV of all the rest, which does not compare favorably to Pt. In alkaline conditions, however, as seen in Fig. 4.4, the onset potential is 0.96 V, 640 mV more positive, a large gain in potential, just by making the system more alkaline.

Pd has also been studied as a possible oxygen reduction catalyst. Lima and coworkers found that it has a comparable onset potential and limiting current to Pt in

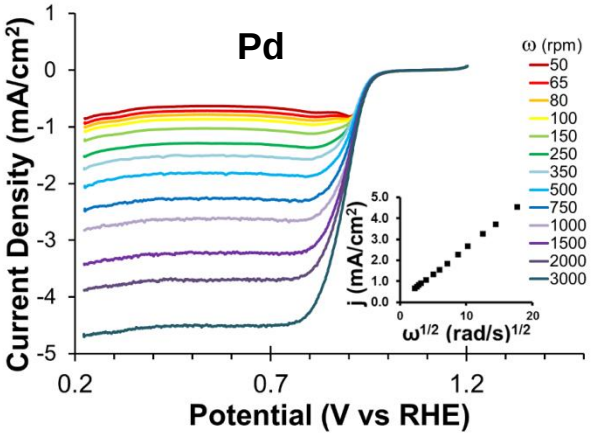

Figure 4.6. RDE negative-going sweeps of O_2-saturated 1.0 M NaOH at a Pd disk electrode, 20 mV/s, rotated between 50 and 3000 rpm. Inset: Levich plot sampled at E = 0.42 V

alkaline media.[11] Levich analysis shows that at pH 1 and 14, oxygen reduction at Pd proceeds primarily through the 4-electron pathway, but that under acidic conditions it does generate more H_2O_2, giving a Levich electron count of 3, whereas under alkaline

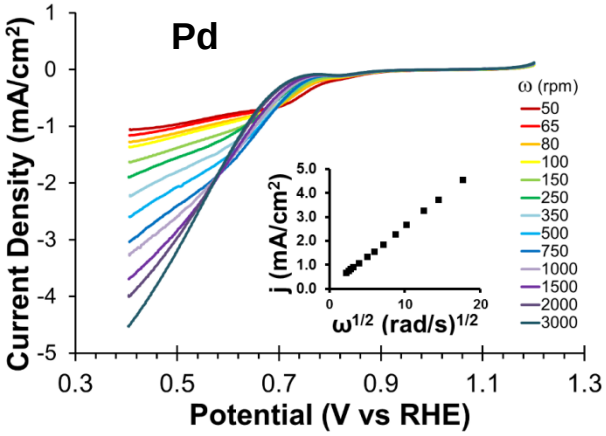

Figure 4.7. RDE negative-going sweeps of O_2-saturated 0.1 M $HClO_4$ at a Pd disk electrode, 20 mV/s, rotated between 50 and 3000 rpm. Inset: Levich plot sampled at E = + 0.46 V.

conditions it is between 3.7-4.0. In alkaline conditions, the kinetics of oxygen reduction are fast, and even at 3000 rpm, mass-transport limit is achieved as is seen in Fig. 4.6. In acidic conditions, however, the kinetics appear to be more sluggish, with a shallower slope, as shown in Fig 4.7, and with many of the faster rotation rates failing to reach mass-transport limit.

The onset potential of ORR on Pd follows a non-Nernstian shift of 150 mV from pH 1 to pH 14. At pH 1, the onset potential is+ 0.74 V, and at pH 14, the E_{onset} is +0.89 V, actually comparable to Pt under those conditions, though at pH 1, it is about 90 mV less. Lima and coworkers have shown that the onset potential of Pd is also comparable to Pt, around 0.9 V vs RHE .[11]

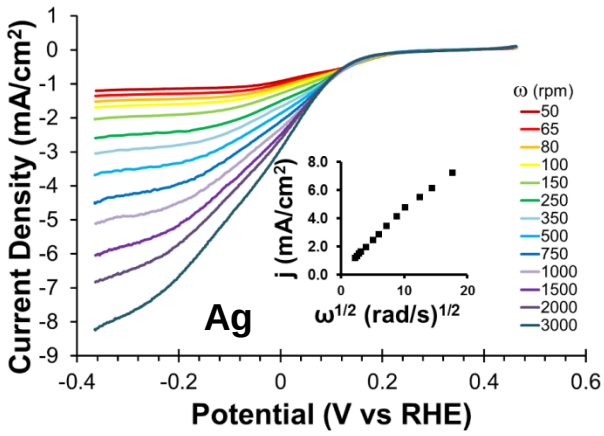

Figure 4.8. RDE negative-going cathodic sweeps of O_2-saturated 0.1 M $HClO_4$ at an Ag disk electrode, 20 mV/s, rotated between 50 and 3000 rpm. Inset: Levich plot sampled at *E* = - 0.24 V.

Ag has been studied as a possible oxygen reduction electrocatalyst, in particular because it is inexpensive relative to the other PGMs. Some work on Ag shows that it will catalyze oxygen reduction, but under acidic conditions, the

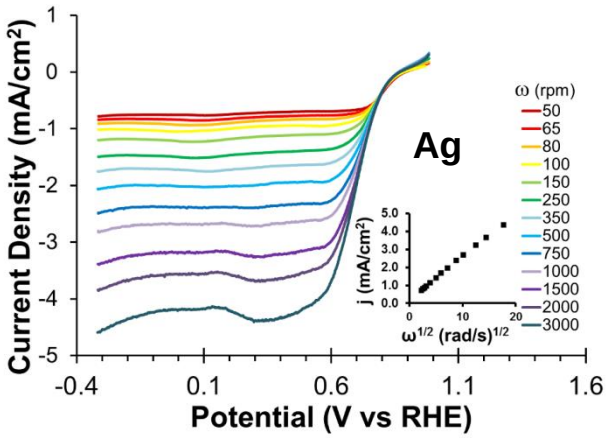

Figure 4.9. RDE negative-going sweeps of O_2-saturated 1.0 M NaOH at an Ag disk electrode, 20 mV/s, rotated between 50 ad 3000 rpm. Inset: Levich plot sampled at E = + 0.42 V.

potentials are not favorable.[8,23,30–32] This is consistent with our own work on bulk Ag, shown in Fig. 4.8. Although the voltammograms reach a transport limit, particularly at low rotation rates, the Levich plot shows definite curvature at higher rotation rates, and the E_{onset} is a terrible 0.16 V vs RHE. Similar to gold, however, silver also shows a large non-Nernstian shift: in alkaline medium, the onset potential is +0.82 V, a difference of 660 mV. Our own work on bulk, polycrystalline silver shows that it reduces oxygen under both acidic and alkaline conditions, and that in both reduction proceeds through the 4-electron pathway (Figs. 4.8 and 4.9). This has been reported in the literature, and is one of the reasons that silver is often touted as a potential ORR catalyst for alkaline fuel cells.[33]

4.3.2 Metacomparison of metals

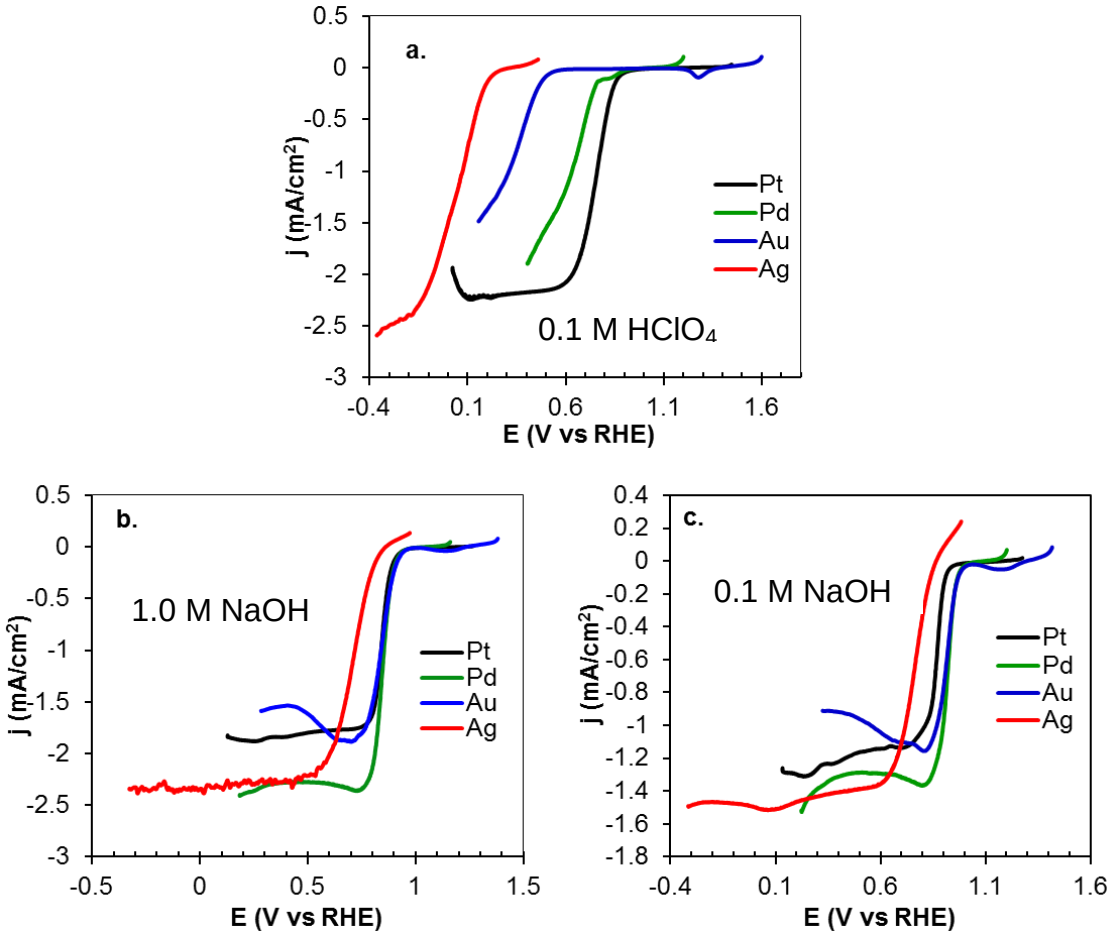

Figure 4.10. Metacomparison of each metal in (a) 0.1 M $HClO_4$, (b) 1.0 M NaOH, (c) 0.1 M NaOH. Rotation rate: 250 rpm, scan rate: 20 mV/s

In order to more easily note differences in the metals' catalytic activity, we can compare data at a single rotation rate so as to note differences in shape, limiting current, and onset potential. Fig. 4.10a shows each metal rotation rate of 250 rpm in 0.1 M $HClO_4$. The onset potentials of the four different metals have large differences, with almost a volt between the best onset potential—Pt—and the worst—Ag. Although Pt has the best onset potential, and by Levich analysis it does proceed

primarily through the 4-electron pathway, when compared to Ag, the limiting current is slightly lower. Not only that, despite the Levich analysis, there does appear to be some H_2O_2 generated at Pt, as shown by the slight positive increase in the current near 0.1 V. Under acidic conditions, however, Pt and Ag appear to reach transport-limit, despite Ag's terrible E_{onset}.

In 1 M NaOH, the situation changes, however. Fig. 4.10b again shows results for each metal at a rotation rate of 250 rpm. In alkaline conditions, all metals are able to reach mass-transport limit for the ORR. The onset potentials are also much closer together—varying only over a range of 150 mV. Au has the most positive E_{onset} potential, 70 mV more positive than Pd and Pt. Ag is the worst metal under these conditions, but considering its cost, it is only 70 mV worse than Pt, and is significantly lower in cost. Fig. 4.10c presents the data, but instead in 0.1 M NaOH. The electrochemistry is comparable to that in Fig. 4.10b in 1.0 M NaOH.

4.3.3 Reaction Phase Diagram

Thus far, much of the discussion in this chapter has focused on mechanistic differences among the catalysts—are they likelier to proceed via the 2 or 4 electron reduction pathways. Looking at separate RDE voltammograms for different metals on different plots does not facilitate a comparison of E_{onset} values, which is an important parameter for any potential ORR catalyst. Some of the catalysts exhibit significant E_{onset} shifts with pH, and they are plotted with respect to a pH normalized reference electrode in Fig. 4.11 (and shown tabulated in Table 4.1). At pH 1, all four catalysts are differentiated, with almost a 700 mV difference among them. Au and Ag, in

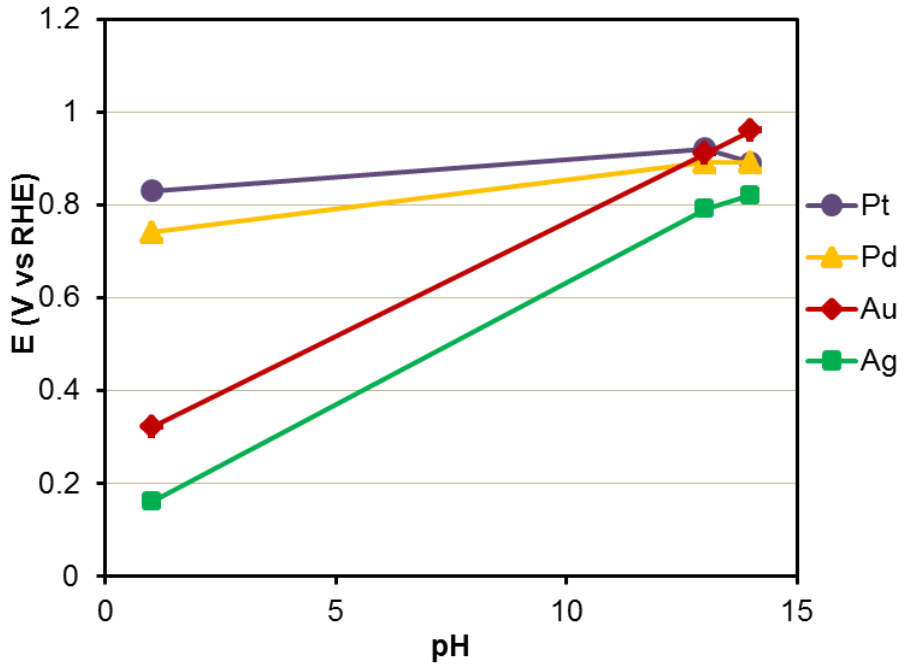

Figure 4.11. Experimental "reaction phase diagram" for the E_{onset} of each of the four metals. Values collected at 350 rpm, at the potential of 10% of the i_l.

particular, have particularly sluggish kinetics at acidic pHs. The E_{onset} at Ag may be correlated to the oxidation state of the surface of the electrode. The Pourbaix diagram for Ag shows that Ag oxidizes and even dissolves until around 0.43 V at pH 1.[22] Although this is more positive than the potential where ORR occurs, the surface may need to be sufficiently reduced before ORR can take place, if the oxide is inhibitory or inactive. At higher pHs, Ag is much more stable, forming an oxide only at high applied potentials, over 1.0 V. This improvement may also be related to the concentration of OH^-—and perhaps its adsorption—as there is a small difference between pH 13 and 14, where Ag is stable, and the only real difference is the concentration of OH^-.

Au, on the other hand, does not form an oxide under any "normal" aqueous acidic or alkaline conditions (with the notable exception of in the presence of aqua regia, which works to oxidize and then complex the Au),[22] but it still shows a large difference in the ORR activity from acidic to alkaline pH's. This difference may be caused by adsorption of OH^- at high pH having a beneficial effect on the catalysis, or the rate determining step of the reaction involving OH^-, so that having a high concentration of OH^- therefore has a beneficial effect on the reaction kinetics. The E_{onset} of both Pt and Pd depends much less on the pH, although they each exhibit a small benefit by going to more alkaline conditions.

Table 4.1. E_{onset} values for the four metals tested at different pH conditions. E_{onset} measured at 350 rpm. E_{onset} defined as the potential where 10% of the limiting current is achieved.

	pH 1	**pH 13**	**pH 14**
Pt	0.83	0.92	0.89
Au	0.32	0.91	0.96
Pd	0.74	0.89	0.89
Ag	0.16	0.79	0.82

4.4 Conclusion

Although under acidic conditions, Pt is clearly the best ORR catalyst with respect to its fast kinetics and reaction pathway, as the conditions shift to more alkaline pH's, Pt is no longer the clear choice for the "best" catalyst. Despite the fact that it still has fast kinetics, it produces more HO_2^- than Pd, which has similarly fast kinetics and costs less than Pt (as of this writing, Pd costs about 40% less). Ag, while a very poor catalyst under acidic conditions, improves dramatically under alkaline conditions, demonstrating why it has been suggested as an alkaline ORR catalyst for years. Au, which was the sole catalyst that produced only H_2O_2/HO_2^-, had a very good E_{onset} at very high pH, but because it only produces HO_2^- under these (and other) conditions, it is not a sensible or practical ORR catalyst.

4.5 References

(1) Colón-Mercado, H. R.; Kim, H.; Popov, B. N. *Electrochemistry Communications* **2004**, *6* (8), 795–799.

(2) Lima, F. H. B.; Salgado, J. R. C.; Gonzalez, E. R.; Ticianelli, E. A. *Journal of The Electrochemical Society* **2007**, *154* (4), A369.

(3) Oezaslan, M.; Hasche, F.; Strasser, P. *Journal of The Electrochemical Society* **2012**, *159* (4), B394–B405.

(4) Kostalik, H. A.; Clark, T. J.; Robertson, N. J.; Mutolo, P. F.; Longo, J. M.; Abruña, H. D.; Coates, G. W. *Macromolecules* **2010**, *43* (17), 7147–7150.

(5) Noonan, K. J. T.; Hugar, K. M.; Kostalik, H. A.; Lobkovsky, E. B.; Abruña, H. D.; Coates, G. W. *J. Am. Chem. Soc.* **2012**, *134* (44), 18161–18164.

(6) Hugar, K. M.; Kostalik, H. A.; Coates, G. W. *J. Am. Chem. Soc.* **2015**, *137* (27), 8730–8737.

(7) Varcoe, J. R.; Slade, R. C. T. *Fuel Cells* **2005**, *5* (2), 187–200.

(8) Sepa, D.; Vojnovic, M.; Damjanovic, A. *Electrochimica Acta* **1970**, *15* (8), 1355–1366.

(9) Koper, M. T. M. *Nat Chem* **2013**, *5* (4), 255–256.

(10) Stamenkovic, V.; Schmidt, T. J.; Ross, P. N.; Markovic, N. M. *J. Phys. Chem. B* **2002**, *106* (46), 11970–11979.

(11) Lima, F. H. B.; Zhang, J.; Shao, M. H.; Sasaki, K.; Vukmirovic, M. B.; Ticianelli, E. A.; Adzic, R. R. *Journal of Physical Chemistry C* **2007**, *111* (1), 404–410.

(12) Genshaw, M. A.; Damjanovic, A.; Bockris, J. O. . *Journal of Electroanalytical Chemistry and Interfacial Electrochemistry* **1967**, *15*, 163–172.

(13) Damjanovic, A.; Genshaw, M. A.; Bockris, J. O. . *Journal of Electroanalytical Chemistry and Interfacial Electrochemistry* **1967**, No. 15, 173–180.

(14) Bacon, F. T.; Fry, T. M. *Proc. R. Soc. Lond. A* **1973**, *334* (1599), 427–452.

(15) Warshay, M.; Prokopius, P. R. *The fuel cell in space: Yesterday, today and tomorrow*; 1989.

(16) Lu, Y. C.; Xu, Z.; Gasteiger, H. A.; Chen, S.; Hamad-Schifferli, K.; Shao-Horn, Y. *Journal of the American Chemical Society* **2010**, *132* (35), 12170–12171.

(17) Markovic, N.; Gasteiger, H.; Ross, P. N. *Journal of the electrochemical society* **1997**, *144* (5), 1591–1597.

(18) Ramaswamy, N.; Mukerjee, S. *J. Phys. Chem. C* **2011**, *115* (36), 18015–18026.

(19) Yang, Y.-F.; Zhou, Y.-H.; Cha, C.-S. *Electrochimica Acta* **1995**, *40* (16), 2579–2586.

(20) Jiang, L.; Hsu, A.; Chu, D.; Chen, R. *J. Electrochem. Soc.* **2009**, *156* (3), B370–B376.

(21) Kondo, S.; Nakamura, M.; Maki, N.; Hoshi, N. *J. Phys. Chem. C* **2009**, *113* (29), 12625–12628.

(22) Pourbaix, M. *Atlas of Electrochemical Equilibria in Aqueous Solutions*, 2nd ed.; National Association of Corrosion Engineers: Houston, Texas, 1974.

(23) Blizanac, B. B.; Ross, P. N.; Markovic, N. M. *Electrochimica Acta* **2007**, *52* (6), 2264–2271.

(24) Rahim, A.; Abdel Hameed, R. M.; Khalil, M. W. *Journal of power sources* **2004**, *134* (2), 160–169.

(25) Merle, G.; Wessling, M.; Nijmeijer, K. *Journal of Membrane Science* **2011**, *377* (1), 1–35.

(26) Arán-Ais, R. M.; Yu, Y.; Hovden, R.; Solla-Gullón, J.; Herrero, E.; Feliu, J. M.; Abruña, H. D. *J. Am. Chem. Soc.* **2015**, *137* (47), 14992–14998.

(27) Elezovic, N. R.; Babic, B. M.; Vracar, L. M.; Krstaiic, N. V. *J. Serb. Chem. Soc.* **2007**, *72* (7), 699–708.

(28) Gasteiger, H. A.; Ross, P. N. *J. Phys. Chem.* **1996**, *100* (16), 6715–6721.

(29) Zurilla, R. W.; Sen, R. K.; Yeager, E. .

(30) Blizanac, B. B.; Ross, P. N.; Marković, N. M. *The Journal of Physical Chemistry B* **2006**, *110* (10), 4735–4741.

(31) Maheswari, S.; Sridhar, P.; Pitchumani, S. *Electrocatalysis* **2012**, *3* (1), 13–21.

(32) Hansen, H. A.; Rossmeisl, J.; Nørskov, J. K. *Physical Chemistry Chemical Physics* **2008**, *10* (25), 3722.

(33) Spendelow, J. S.; Wieckowski, A. *Physical Chemistry Chemical Physics* **2007**, *9* (21), 2654.

CHAPTER 5

ELECTROCHEMICAL SCREENING OF METAL BINARY OXYGEN REDUCTION CATALYST FILMS

5.1 Abstract

In acidic fuel cells, Pt-containing compositions are the best oxygen reduction catalysts, due to their facile reaction kinetics and good stability under operating conditions. As more and better alkaline membranes are developed, however, alkaline fuel cells have become a potentially more viable alternative, and with it, the possibility of using non-Pt and even Pt-free oxygen reduction catalysts. In this chapter, we have explored the ORR activity in base of binary metal catalysts of Pd, Cu, Ag, Au, and Rh by depositing thin films onto glassy carbon electrodes and using them as normal rotating disk electrodes. All metals were deposited in equimolar ratios, and the best compositions were those containing Pd, in particular $Pd_{0.5}Cu_{0.5}$ and $Pd_{0.5}Au_{0.5}$

This work was done in collaboration with Andrés Molina-Villarino and Marc Murphy.

5.2 Introduction

As the demand for and cost of fossil fuels rises, people are increasingly turning to alternative sources of energy, particularly for the purpose of powering their automobiles. Fuel cell vehicles are a promising technology—in 2015 automobile manufacturers Hyundai and Toyota released their first fuel cell-powered vehicles, available for lease. Despite these releases, some unresolved issues that merit further

study remain. The cathode, in particular, where the oxygen reduction reaction (ORR) occurs, is particularly problematic, as it has sluggish reaction kinetics, leading to a decrease in the fuel cell's efficiency (increased overpotentials). Additionally, the cathode is held at oxidizing potentials, and as a result many non-noble metals will oxidize or even dissolve in that environment.

By moving from an acidic fuel cell system, or proton exchange membrane fuel cell (PEMFC), to an alkaline fuel cell (AFC) or anion exchange membrane fuel cell (AEMFC) system, some of these problems could be mitigated. Some metals exhibit a non-Nernstian shift in the onset of different reactions when moving from an acidic to an alkaline system, meaning that when the voltammograms are plotted against a pH-independent reference (such as RHE) , they do not remain constant as a function of pH, but instead shift, suggesting that a different mechanism might be operating.[1,2] For the ORR, a positive non-Nernstian shift would increase the efficiency of the a cell. Beyond having potentially higher efficiencies in alkaline systems, many metals exhibit improved stability in alkaline media. Pourbaix diagrams show that Ag and Cu both dissolve under acidic pHs but are much more stable in alkaline medium, with Cu forming the passivating Cu_2O. If the pH becomes too alkaline, however, Cu can dissolve.[3] Ag has been long proposed as a potential catalyst for alkaline ORR[4–6] Cu, on the other hand, has been combined with another metal (e.g. Pt) in some ORR work, and when used, its purpose has typically been to dissolve under reaction conditions, leaving behind a more active noble metal.[7–10] Work in the corrosion community, however, has shown that Cu has some activity for the ORR.[11,12] This could suggest that there is space in the alkaline ORR community for alkaline catalysts that are based

on non-Pt metals.

Because of the number of possible metals that can be used as ORR catalysts is so great, in addition to lacking a good predictor of catalytic activity, having a method that quickly screens different compositions can be beneficial. One approach is combinatorial, or high-throughput, screening. Much of the combinatorial electrocatalysis work has dealt with acidic systems, and some different approaches for sample (library) generation have been to ink-jet print catalysts[13–16] and to use physical vapor deposition (PVD) methods, such as sputtering, to deposit thin film composition libraries.[17–20] While these methods can simultaneously produce potentially hundreds of compositions in a given library, electrochemically analyzing the compositions has been challenging. Many of these methods have involved the use of a fluorescent marker such as quinine or fluorescein, that was sensitive to a localized change in pH to indicate active areas.[14,19,21] Others have involved the deposition of discrete spots of a certain composition, either by the previously-mentioned ink-jet synthesis, or by PVD with a shadow mask,[22] that can then be electrochemically evaluated individually.

These techniques have some drawbacks, however. The fluorescent markers used, in the mentioned studies, are not suitable for highly alkaline conditions, as the pK_a's of the fluorescent molecules are too low for the transition to be relevant for AFC's. Work focusing on alkaline combinatorial work of this nature has been at a pH value of up to 10.[23] Alkaline ORR work, however, is typically conducted in 0.1 M strong base (KOH or NaOH), yielding a pH of 13. The discrete combinations are also limited by their geometries. In other words, the compositions can only analyzed using quiescent solution methods, such as cyclic voltammetry, where limited mechanistic

information can be determined. Typically, hydrodynamic methods, such as rotating disk electrode voltammetry (RDE), are used for ORR because they provide much more mechanistic information. Although for H_2 oxidation (HOR) this only has a small effect on the results, for the ORR, which has two separate pathways, it is much more important. Not only can the ORR proceed through two different reaction pathways, the direct or 4-electron mechanism to produce HO^-, and the series or 2-electron mechanism to produce HO_2^- , but the HO_2^- produced is also deleterious to the fuel cell, where it can oxidize the membrane and lead to faster degradation and a decline in performance. For the ORR then, knowing the pathway is particularly important. Scanning electrochemical microscopy (SECM) can be used to determine this information while spatially resolving samples,[24] but, because of its high resolution and sequential nature, is less useful for screening many compositions quickly.

Work by Dahn, *et al*. circumvents the problem of geometry by changing the sample. Instead of depositing their catalyst compositions onto a wide, flat substrate such as a Si wafer or Toray conductive graphite paper,[16] they deposit metal catalysts onto 5 mm glassy carbon disks, a common electrode material.[25] Prior to deposition, they coat the glassy carbon substrate with a 50 nm-thick nanostructured thin film from 3M that is more resistant to oxidation than traditional carbon black supports.[22,25–27] Some of their catalysts were sputtered in a layered structure, where the metals were deposited in an alternating fashion, and some were co-sputtered. Their approach allowed them to study many different compositions in a high-throughput manner, while also being able to focus, with greater depth, on the compositions of interest. While this work covered a variety of metals (Pt, Co, Ni, Ir) in both acid and alkaline

conditions, all of it included Pt. Nevertheless, they also have published work on transition metal carbonitrides for oxygen reduction catalysts.[28]

Our work seeks to follow the example set by the Dahn group—to use sputter deposition to deposit thin films for screening of potential oxygen reduction catalysts—but instead of studying Pt_xM_{1-x} binaries, we have chosen to study compositions without platinum in alkaline medium. The use of alkaline medium greatly increases the number of stable metals, as discussed previously, which makes the use of a screening method helpful to narrow the field of possible binary candidates, while in this paper, we have only focused on 1:1 binaries, clearly more complex combinations can be studied. Promising combinations of metals can be selected from this work, and the composition space can be examined in greater depth in future studies. We aim to find alternatives to Pt-containing ORR catalysts in alkaline media.

5.3 Experimental

5.3.1 Sputtering Chamber Setup

Thin films were deposited in a custom-built sputter deposition chamber, as described earlier by Gregoire *et al.*[18] Inside the chamber, a 4 in. magnetron sputter gun (AJA, Inc.) was equipped with a Ti target, used for the deposition of uniform adhesion layers. There was also an array of three 2 in. magnetron sputter guns (Angstrom Sciences Onyx-2) that enabled a composition spread of about 1 at.%/mm as a result of their placement and 15° tilt.[18] A fourth, center gun, set just below the level of the other three guns, was not used in this work. A quartz crystal thickness monitor (Inficon) allowed for the measurement of the deposition rates for both the 4 in. gun, and also for the 2 in. guns, individually or together.

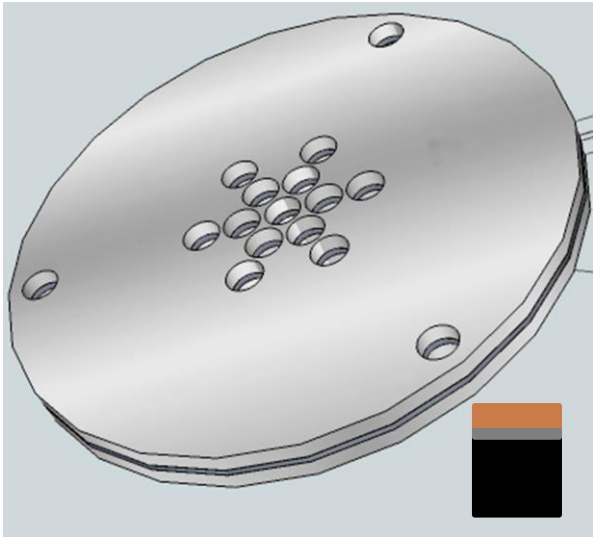

Figure 5.1. Diagram of the special RDE holder that fits into the aluminum disk. Inset: diagram of sputtered glassy carbon sample (not to scale), where black represents glassy carbon, silver is Ti, copper is the catalyst layer.

To deposit the metals on the glassy carbon samples used in this study, we used a special substrate holder (Fig. 5.1) consisting of two aluminum plates with sixteen holes (5 mm diameter), held together with screws, and with a Viton fluoroelastomer gasket to hold the glassy carbon disks securely in the holes. This holder screwed into the rotating aluminum disk in the chamber, and was held parallel to it and to the sputtering guns. The aluminum holder and ring allowed for the deposition of an adhesion layer and then the catalyst layer, without opening the chamber. Glassy carbon slugs were mounted in the holder so that they were flush with the surface of the holder to prevent shadowing effects during deposition.

Films were deposited on manually-polished 5 mm diameter glassy carbon slugs (described below) in Ar (5 mTorr or 0.67 Pa) at ambient temperature. Each glassy carbon slug was cleaned with isopropanol before placing in chamber, to remove any dust or residual oils that might have accumulated on the surface. Once under vacuum, a 12 nm Ti adhesion layer was deposited directly on the glassy carbon at a rate of 2 Å/s. On top of the adhesion layer, 50 nm of catalyst layer were then deposited, with each metal's deposition rate set to be 2 nmol/sec.

5.3.2 Electrochemistry

To prepare the glassy carbon electrode for sputtering, the glassy carbon slugs (5 mm, Sigradur G, HTW) were polished with polishing papers (Buehler, p 280-2500), to initially get an even surface, and then polished to a mirror finish with diamond paste and diamond paste extender (1μm particle size, Buehler, Buehler Metadi fluid) on polishing cloths **(**Buehler Microcloth**)**. After deposition, samples were stored in

deionized water to prevent contact with air and to act as a physical barrier. To use them for electrochemical testing, samples were removed from the water, dried gently, and the sides were wrapped with Teflon tape to form a tight seal and prevent leaks. The Teflon-wrapped samples were then inserted into an exchangeable rotating disk electrode (RDE) tip (Pine Research Instrumentation, E4TQ series tip and holder). A glass cap was then placed onto the electrode shaft and inserted into the rotator (Pine Research Instrumentation, AFMSR series) with a custom-built three-neck electrochemical cell designed specifically for RDE experiments. A bipotentiostat (Pine Research Instrumentation, AFRDE5) was used with a large-area Pt mesh counter electrode and a home-built Ag/AgCl reference electrode.

When testing samples, a NaOH solution (0.1 M, Malinckrodt AR) was used as the electrolyte. Before electrochemical testing, the cell and electrolyte solution were deoxygenated for 15 minutes with N_2 (Airgas, HP). For binary materials, a window-opening cyclic voltammogram (CV) was performed to establish a stable potential range before proceeding with electrochemical cleaning. Electrodes were cleaned electrochemically at 50 mV/s until their CVs remained constant, at which point the solution was oxygenated (Airgas, UHP) for 15 minutes while continuing electrochemical cycling. To perform the oxygen reduction experiments, rotation rates between 50-2000 rpm were used, and the potential was swept at 20 mVs^{-1}. In between each rotation rate, the solution was bubbled with O_2 for seven minutes to keep the solution saturated, particularly after high rotation rates that can agitate the surface of the solution more, leading to deoxygenation.

The Levich equation was used to analyze oxygen reduction data. For O_2, a D_O

of 1.93×10^{-5} cm^2s^{-1} was used, and the concentration was taken to be 1.25 mM. These values yield a value of n = 4 for bulk Pd, a material that is recognized as reducing O_2 through the direct mechanism in alkaline conditions. [29] Currents used for Levich analysis were taken from the mass-transport limited region of the voltammograms, though the exact potential varied among samples.

5.3.3 X-Ray Diffraction

Structural and texture information for each alloy thin film on glassy carbon were obtained through area XRD measurements using a Bruker AXS general area detector diffraction system (GADDS). A collimated Cu-kα (λ = 1.54059 nm) X-ray source was incident onto each sample at a fixed angle of 20°relative to the sample plane. The Hi-STAR area detector measures diffraction azimuthally, allowing for rapid identification of crystallographic texture, based on intensity variations along the diffraction arcs. The area detector was oriented to 2θ = 40°, and the detector-to-sample distance was measured to be 6.050 cm. The sample tilt angle φ was fixed to 0°.

5.3.4 X-Ray Photoelectron Spectroscopy

Surface compositions at the centers of each film, on the glassy carbon slugs, were measured using X-ray photoelectron spectroscopy (XPS). Survey scans were measured between 1100 and 0 eV under high vacuum (2×10^{-9} Torr) using an Al-Kα x-ray source. The survey spectra were quantitatively analyzed using CASA XPS software.

5.4 Results and Discussion

Although in proton-exchange membrane (PEM) fuel cells, platinum is the cathode catalyst of choice due to its fast kinetics and favorable mechanistic properties, in alkaline systems, the choice of an oxygen reduction catalyst is not so straightforward. The less corrosive alkaline conditions enables the use of less-noble metals than in PEM fuel cells, thereby, in principle, decreasing the cost of the membrane electrode assembly (MEA). Much of the work on alkaline ORR catalysts has dealt with catalysts containing Pt, often combined with other platinum-group metals (PGM) or other less-noble metals. Our work seeks to exploit other non-Pt metals as possible ORR catalysts to take advantage of the more favorable kinetics in alkaline medium and also the decreased cost associated with many other metals, relative to Pt.

For this study, we chose five metals— Au, Rh, Pd, Ag, and Cu—and tested binary compositions of each element in equimolar ratios. In order to be able to compare if the binary compositions were favorable, relative to their parent metals (with respect to both their catalytic behavior), we also made thin films of each individual metal to use as controls. The ORR data for these films are presented in Fig. 5.2. The films' behavior was, qualitatively, largely consistent with the bulk metals'

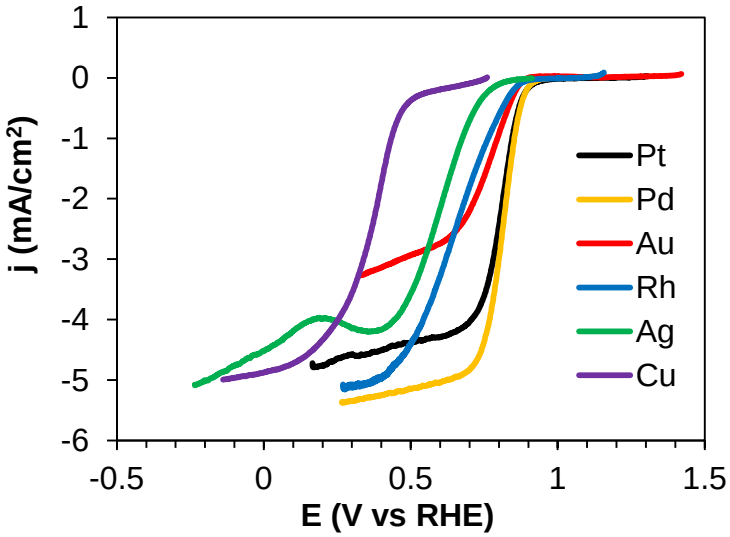

Figure 5.2. Metacomparison of RDE profiles for single metal thin films, 1500 rpm in 0.1 M NaOH. ν = 20 mV/s

electrochemical responses; although the limiting currents were consistently about 18% less than what would be expected for bulk materials. We saw this for all of the thin film samples that we tested, and further experimentation (Fig. 5.3) suggested it to be due to the wrapped PTFE tape, which covered ~0.2 mm of the outer edge of each electrode. Although we knew where this deviation originated, we were not able to retroactively determine the exposed area for each individual film. While the approximation allowed for the elucidation of trends, we have declined to draw any

a.

Electrode Geometric Area Calculation using Levich Equation				
#	i_l (A)	ω (rpm)	A (cm^2)	Area Loss (%)
1	-0.000050	350	0.15972	18.7
	-0.000073	750	0.16139	17.8
	-0.000103	1500	0.16107	18.0
2	-0.000050	350	0.16207	17.5
	-0.000102	1500	0.15814	19.5
3	-0.000045	350	0.14452	26.4
	-0.000065	750	0.14391	26.7
	-0.000091	1500	0.14237	27.5
	-0.000105	2000	0.14106	28.2

b.

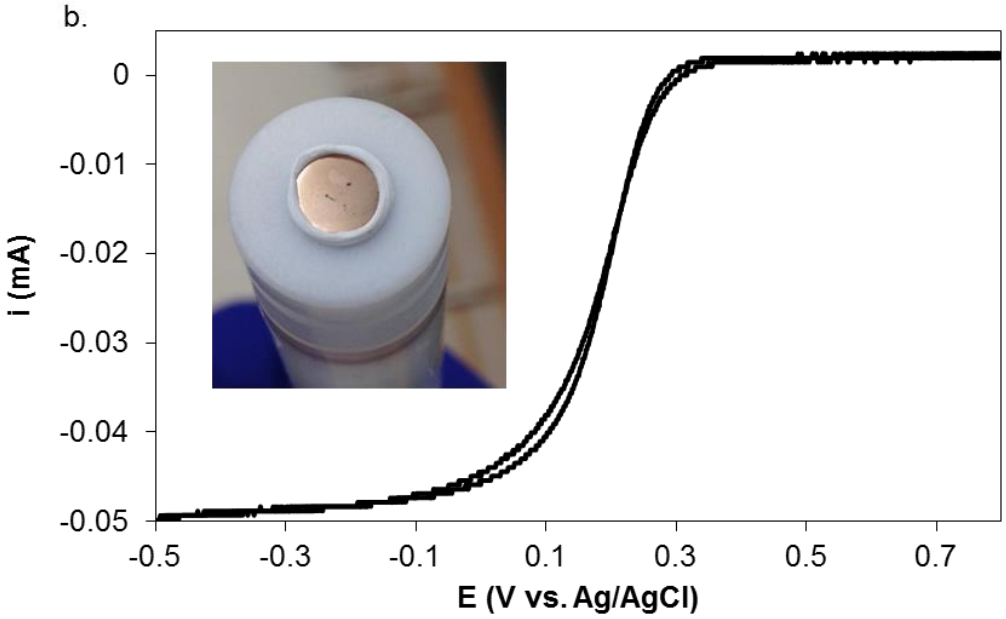

Figure 5.3 a.) Electrode geometric area calculation using Levich equation, using Teflon tape wrapped- glassy carbon electrode, b.) RDE at 350 rpm in 1 mM $K_3Fe(CN)_6$, 0.1 M KCl, ν = 20 mV/s. Inset figure is a sample photograph of a sputtered glassy carbon electrode wrapped in Teflon tape.

conclusions from small differences in i_l among samples. Catalytic activity differences among crystal faces are well known, e.g. for Pt particles,[30,31] and so having a ratio of crystal faces that deviated from purely polycrystalline (i.e. a textured film) could lead to further deviations from the expected limiting current.

Qualitatively, the behavior was analogous to bulk materials or nanoparticles. Au, for example, had a promising onset potential although slightly less than Pt, but with poor i_l, consistent with the production of HO_2^-, which matched literature data on Au.[29] Likewise**,** Rh had a favorable onset potential, and while the reduction barely reached a mass transport limit (due to issues with film delamination when approaching more reducing potentials due to H_2 absorption into the Rh lattice), the limiting current of Rh seemed to converge to a current indicative of the direct mechanism (n = 4 by Levich analysis), which has been previously reported.[32] Ag, which had a worse onset potential than Pd, Rh, and Pt by over 100 mV, is, however, vastly less expensive. Although there was a small plateau at intermediate potentials for Ag, this plateau was not present at lower rotation rates, and may have been caused by a transient species or by an alternative mechanism that became dominant at higher rotation rates. Even so, in the end, the limiting current did reach a value consistent with the direct mechanism. Similarly, Cu, while it had a much less favorable onset potential (here defined as the potential at 10% of the limiting current value) than Ag, also reached limiting currents indicative of the 4-electron mechanism, and is even less expensive than Ag.

By combining these metals in different ways, we hoped to achieve an optimal combination with three criteria: a.) good catalytic activity, as related to both kinetics (onset potential) and the mechanism; 2 vs 4 electrons, b.) the material would be able to

be synthesized as a single phase bulk material, and c.) cost. For these reasons, all five metals were be used in the binary compositions.

Before discussing all of the binary compositions together, we looked at the combinations with each metal individually. Figure 5.4 presents the ORR RDE profile for Au and of its binary compositions. $Au_{0.5}Cu_{0.5}$seems to benefit the most from the addition of Au with respect to onset potential. $Au_{0.5}Ag_{0.5}$ and $Au_{0.5}Rh_{0.5}$ seemed to benefit less, though the onset was more favorable than for simple Ag alone. The

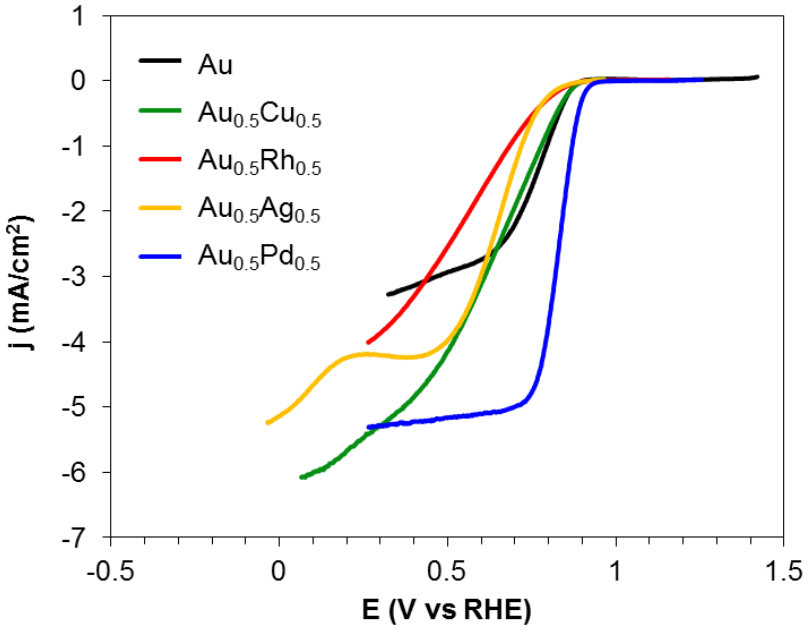

Figure 5.4. Metacomparison for $Au_{0.5}X_{0.5}$ films. 1500 rpm in 0.1 M NaOH. ν = 20 mV/s

limiting currents of $Au_{0.5}Cu_{0.5}$ and $Au_{0.5}Ag_{0.5}$ are most consistent with a 4-electron mechanism; however, the current from $Au_{0.5}Cu_{0.5}$ is about 10% above the theoretical value, likely due to a rough surface from sputtering. Although dissolution of Cu was another possible reason for the roughened surface, the E_{onset} of the ORR did not shift over the course of the experiment, which would suggest that under these conditions

the entire film is stable.(Fig. 5.5) $Au_{0.5}Ag_{0.5}$ seemed to go through a two-step mechanism at high rotation rates that may be attributed to catalytic contributions from both Ag and from Au. At more reducing potentials, however, even at high rotation rates, Levich analysis suggested the production of OH^-. $Au_{0.5}Rh_{0.5}$ performed the worst. It did not reach a transport limit, and it looked resistive, potentially due to poor adhesion in the film, although this behavior was repeatable for a second $Au_{0.5}Rh_{0.5}$ sample. This suggested that if this resistance was due to delamination, then $Au_{0.5}Rh_{0.5}$ films, in general, have poor adhesion. (Many other $Rh_{0.5}M_{0.5}$ films tested also had problems with delamination.)

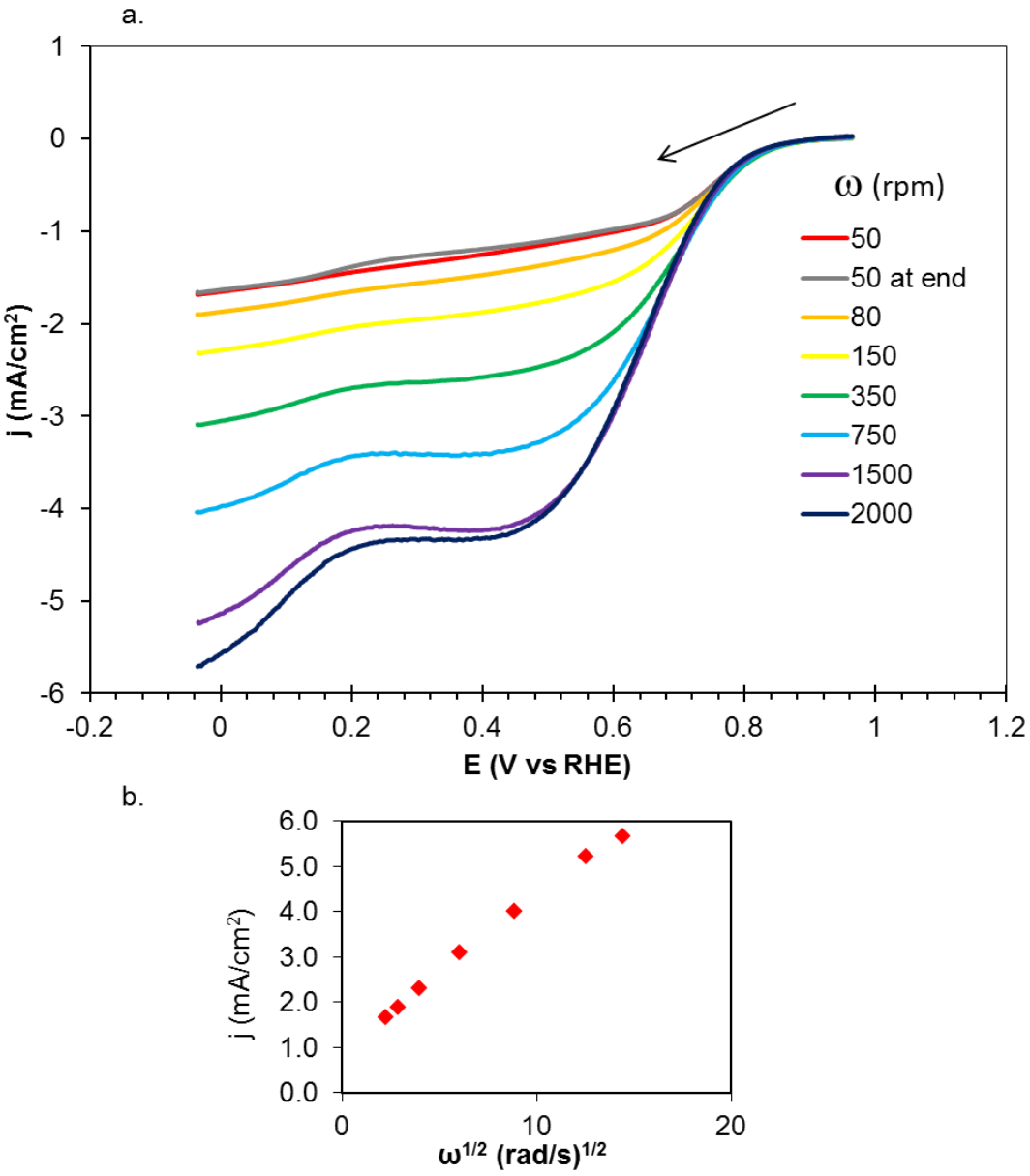

Figure 5.5 a.) The RDE profile of the oxygen reduction reaction at a $Ag_{0.5}Au_{0.5}$ film, ν= 20 mV/s, 0.1 M NaOH. b.) Levich plot obtained at 0.0 V vs RHE.

For compositions containing copper, all the binaries' onset potentials were better than Cu (Fig. 5.6), however, they still followed the trends found in the parent metals, with the order from best to worst being: $Cu_{0.5}Pd_{0.5}$ > $Cu_{0.5}Au_{0.5}$ > $Cu_{0.5}Rh_{0.5}$ > $Cu_{0.5}Ag_{0.5}$. Even so, the electrochemistry did not suggest that this was entirely caused by the leaching of Cu from the films. We still saw currents within the limits of what we would expect from other thin films, with the exception of $Cu_{0.5}Au_{0.5}$ as discussed previously. Even if all the Cu had leached from the film, leaving behind only Au, it would be unlikely that the current would have as large a magnitude as it did because of Au's catalytic properties, unless there was a strong effect from the underlying $Cu_{0.5}Au_{0.5}$. A second $Cu_{0.5}Au_{0.5}$ film did not show limiting currents as high as those shown in Fig. 5.6, which was further consistent with a rough film. $Cu_{0.5}Ag_{0.5}$ and

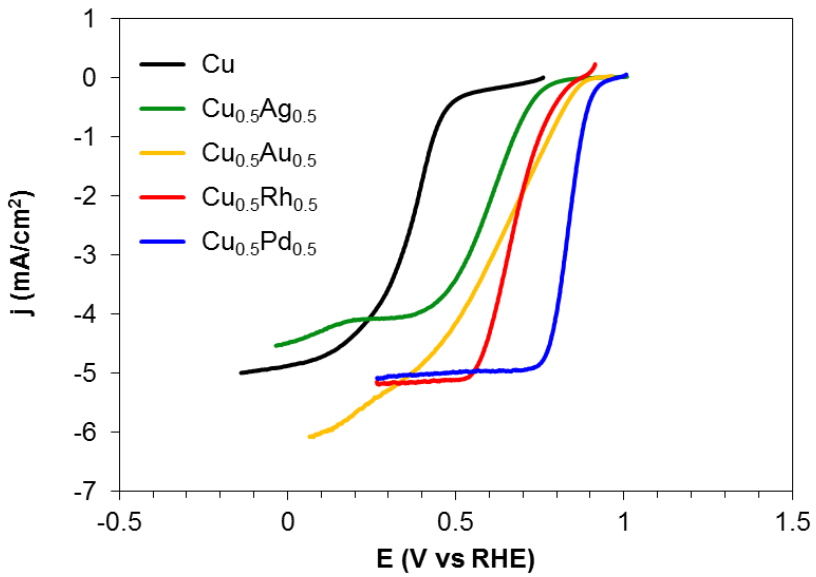

Figure 5.6. Metacomparison for $Cu_{0.5}X_{0.5}$ films. 1500 rpm in 0.1 M NaOH. ν = 20 mV/s

$Cu_{0.5}Rh_{0.5}$ attained limiting currents approximately that of 4-electron reductions.

Binaries containing Ag, shown in Fig. 5.7, had much a more uniform response than those based on Cu or Au, perhaps due to the poor solubility of most elements in Ag. The voltammetric profile of Ag was very similar to that of $Ag_{0.5}Cu_{0.5}$, with the E_{onset}'s being almost superimposable, which may have been caused by more active segregated Ag phases in the film. For these thin film systems, the differences among them were likely not significant. Their limiting currents also converged to the same value, although the shape of the voltammetry for the $Ag_{0.5}Cu_{0.5}$ sample was different than Ag. There were likely some changes in the film, either in the morphology or the surface stoichiometry (due to dissolution or diffusion of Cu in the film), as over the

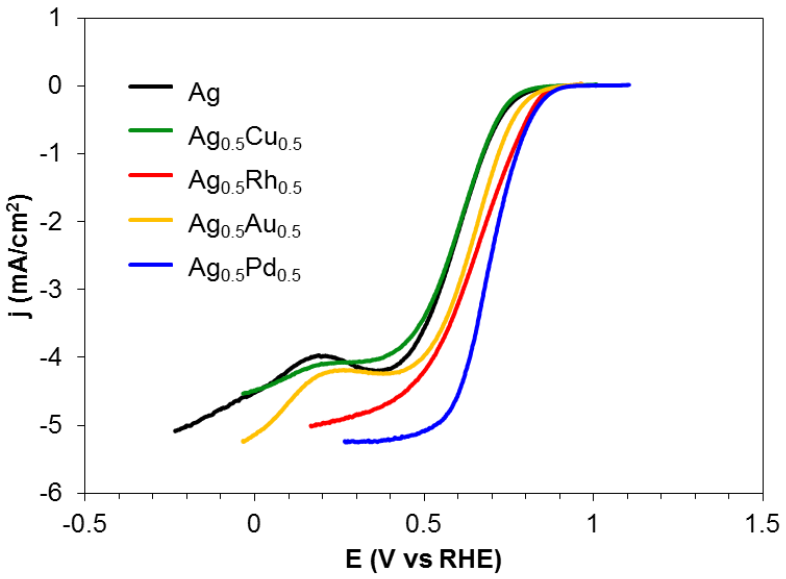

Figure 5.7. Metacomparison for $Ag_{0.5}X_{0.5}$ films. 1500 rpm in 0.1 M NaOH. ν = 20 mV/s

course of the experiment, the onset shifted to more negative potentials (Fig. 5.8), while the Levich plot also showed increasing nonlinearity as the rotation rate increased suggesting kinetic limitations. This seemed to be more consistent with passivation, as

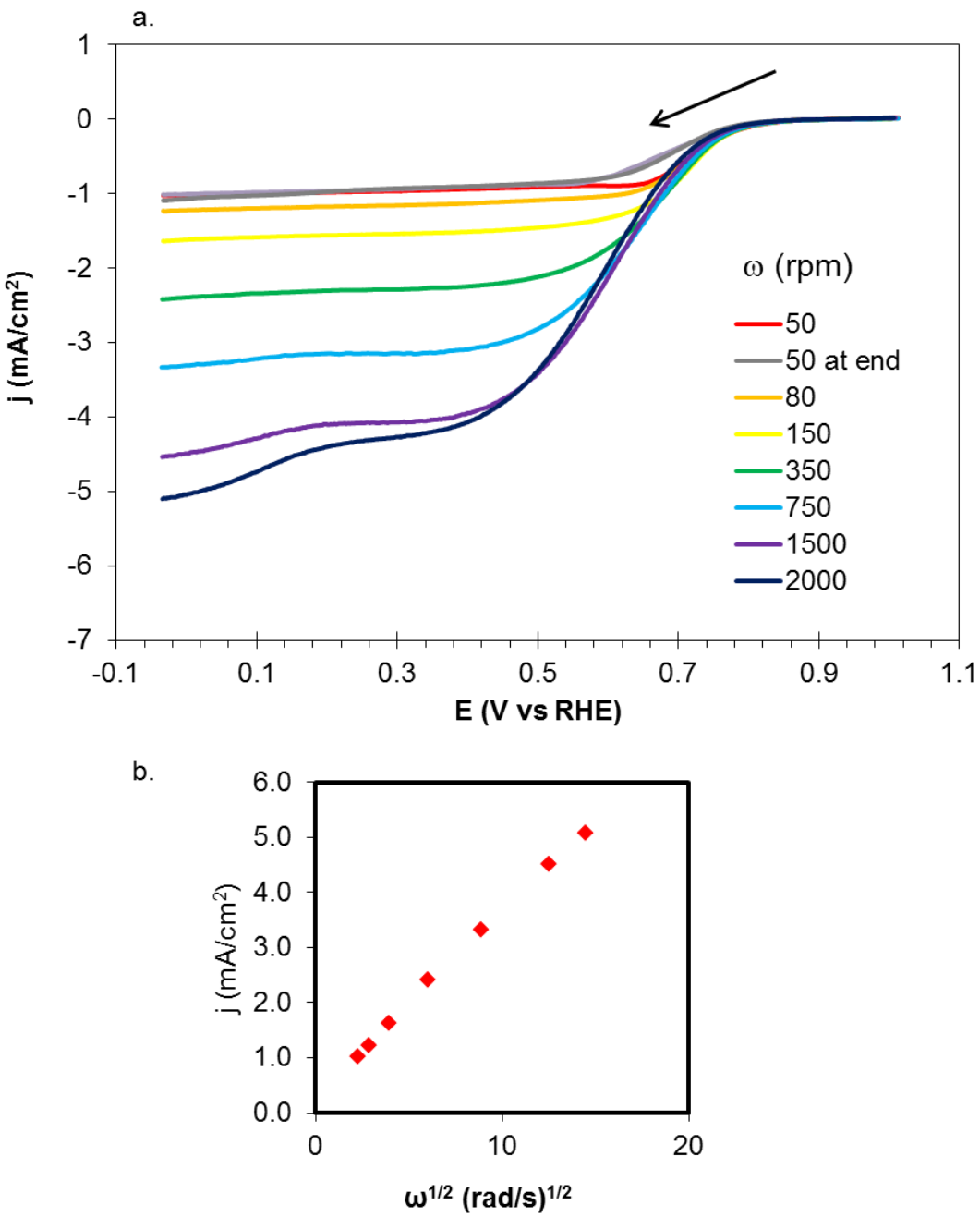

Figure 5.8 a.) The ORR voltammogram of $Ag_{0.5}Cu_{0.5}$. There was a shift in the onset to more negative potentials during the experiment, as the final rotation rate (50 at end) had shifted from the initial 50 rpm. ν= 20 mV/s, 0.1 M NaOH. b.) The Levich plot obtained at 0.0 V vs RHE

the currents decreased, while with dissolution even with the sluggish kinetics of the oxygen reduction reaction, we might expect the currents to be higher, as they were in $Au_{0.5}Cu_{0.5}$. We would like to note, however, that the shifts in the onset during the experiment were greater when samples sat for longer periods of time between

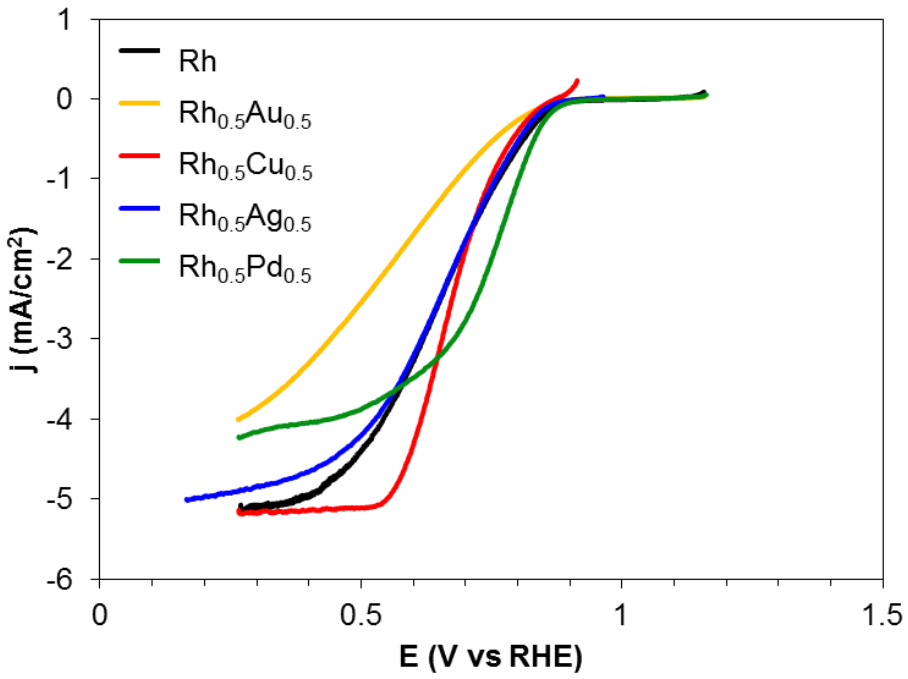

Figure 5.9 Metacomparison for $Rh_{0.5}X_{0.5}$ films. 1500 rpm in 0.1 M NaOH. ν = 20 mV/s

deposition and testing. Finally, although some of these compositions might be interesting because of their moderate cost as well as their reasonable onset potentials, it is worth mentioning that of these compositions, only $Ag_{0.5}Au_{0.5}$ and $Ag_{0.5}Pd_{0.5}$ form single phases as bulk materials, likely due to the large size of Ag atoms. In general, therefore, we concluded that, generally, Ag compositions were not practical catalysts.

All the Rh compositions had comparable onsets to the Rh film and to each other, as shown in Figure 5.9. With the exception of $Rh_{0.5}Au_{0.5}$, all the other

compositions reached very similar limiting currents. $Rh_{0.5}Au_{0.5}$ was noticeably less reversible than the other Rh compositions, although its current corresponded more closely with Au's. $Rh_{0.5}Au_{0.5}$ and Rh films had an almost indistinguishable electrochemical response with respect to the onset potential, as well as the slope/reversibility/kinetics. $Rh_{0.5}Cu_{0.5}$ had a similar onset but a steeper slope than

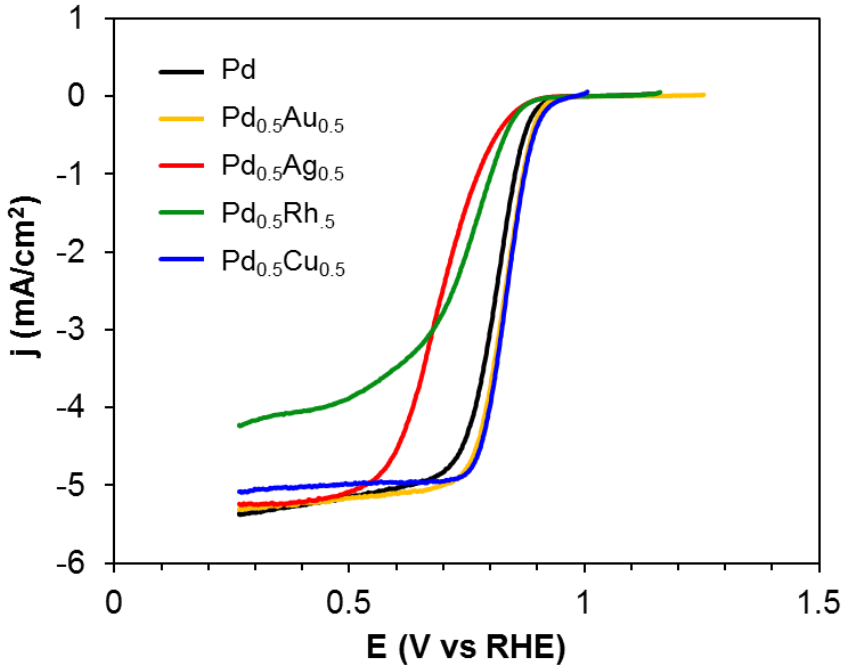

Figure 5.10 Metacomparison for $Pd_{0.5}X_{0.5}$ films. 1500 rpm in 0.1 M NaOH. ν = 20 mV/s

$Rh_{0.5}Ag_{0.5}$ and Rh, indicating better kinetics/reversibility. Unlike the Ag compositions, most of the Rh compositions (with the exception of $Rh_{0.5}Ag_{0.5}$) form a single phase in bulk.

Pd compositions were among the best catalysts we studied. ORR at $Pd_{0.5}Au_{0.5}$ and $Pd_{0.5}Cu_{0.5}$ had fast kinetics and E_{onset} values that actuallywere better than that of Pd. Fig. 5.10. The favorable E_{onset} was not unexpected for $Pd_{0.5}Au_{0.5}$, as both Pd and

Au have fairly close E_{onset} values. This behavior is especially notable for $Pd_{0.5}Cu_{0.5}$, where the binary composition performs better than the individual parent metals by 30-40 mV. Although there has been work on $Pd_{0.5}Cu_{0.5}$ as an acidic oxygen reduction catalyst, these catalysts typically rely on the dissolution of Cu by intentional prior de-alloying.[7,33] XPS data show that the composition after electrochemical

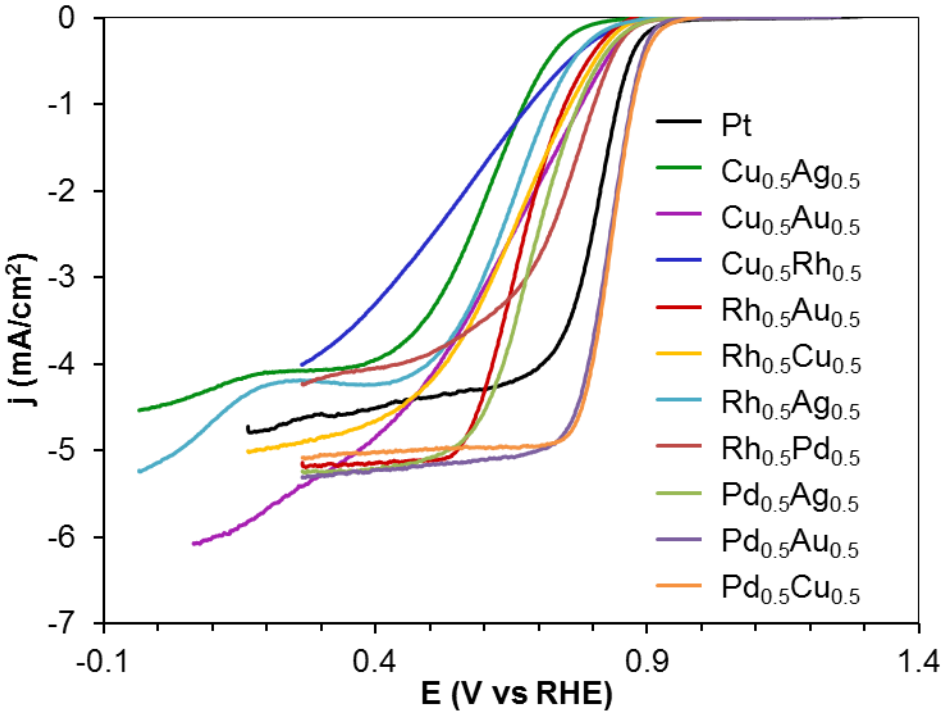

Figure 5.11. Metacomparison of all different compositions tested. 1500 rpm in 0.1 M NaOH. ν = 20 mV/s

experimentation is 85% Cu. This is different from $Au_{0.5}Cu_{0.5}$ and $Rh_{0.5}Cu_{0.5}$, which were also tested, and had Cu levels of 23% ± 8% and 19 ± 8%, respectively. The dissolution in these other compositions was most likely due to the high applied potential required to record the onset of oxygen reduction, as the Pourbaix diagrams shows it may dissolve under high potentials.[3] XPS data for the $Pd_{0.5}Cu_{0-.5}$ are discussed in greater detail in Chapter 6.

After examining each of the five sets of compositions, we were able to compare each individual composition to the others, as well as to Pt (Fig. 5.11). Only two compositions had an onset potential that was better than Pt's: $Cu_{0.5}Pd_{0.5}$ and $Pd_{0.5}Au_{0.5}$. The addition of Cu to Pd to yield the $Pd_{0.5}Cu_{0.5}$ composition also drastically lowered the cost, as the price of Cu was negligible relative to every other metal studied here, including Ag. Not only were its catalytic characteristics favorable, but it can form a single phase at room temperature,[34] making it a better candidate as a potential nanoparticle catalyst. Further studies will seek to establish the optimal ratio of Cu to Pd for these catalysts. $Pd_{0.5}Au_{0.5}$ performed well, but with Au's high cost, we considered it to be a less promising composition for further study. Some compositions containing Au ($Au_{0.5}Rh_{0.5}$, $Ag_{0.5}Au_{0.5}$) had smaller i_l values than most other compositions, but overall the limiting currents were comparable. Small differences in the limiting currents can be attributed to different coverage of the outer circumference of the electrode by the Teflon tape needed to keep the electrode mounted in its holder.

5.5 Conclusions

Stoichiometrically equal metal binary compositions Pd, Cu, Ag, Au, and Rh were sputter-deposited onto glassy carbon substrates. The substrates were not heated during deposition. The sputtered glassy carbon samples were inserted into a special electrode that allowed them to be used to perform rigorous rotating disk electrode voltammetry. The results of these experiments showed that the binary composition films generally had different electrocatalytic behavior than their parent metal films, indicating that the catalytic differences were not caused by dissolution of the less

noble metal, although dissolution or passivation of some metal likely occurred, particularly in the case of compositions containing Cu. $Cu_{0.5}Pd_{0.5}$, however, appeared to have better catalytic activity than Pd and will be an interesting composition space to explore in greater detail in future studies.

5.6 Acknowledgments

This material is based upon work supported as part of the Energy Materials Center at Cornell (EMC2), an Energy Frontier Research Center funded by the U.S. Department of Energy, Office of Science, Office of Basic Energy Sciences under Award Number DE-SC0001086. It was also funded by the NYSTAR grant. This work made use of the Cornell Center for Materials Research Shared Facilities which are supported through the NSF MRSEC program (DMR-1120296). A.Molina-Villarino was funded by the NIH-MARC Program, Grant #5T34GM007821-36.

5.7 References

(1) Yang, J.; Sebastian, P.; Duca, M.; Hoogenboom, T.; Koper, M. T. M. *Chem. Commun.* **2014**, *50* (17), 2148–2151.

(2) Van der Niet, M. J. T. C.; Garcia-Araez, N.; Hernández, J.; Feliu, J. M.; Koper, M. T. M. *Catal. Today* **2013**, *202*, 105–113.

(3) Pourbaix, M. *Atlas of Electrochemical Equilibria in Aqueous Solutions*, 2nd ed.; National Association of Corrosion Engineers: Houston, Texas, 1974.

(4) Sepa, D.; Vojnovic, M.; Damjanovic, A. *Electrochimica Acta* **1970**, *15* (8), 1355–1366.

(5) Wiberg, G. K. H.; Mayrhofer, K. J. J.; Arenz, M. *Fuel Cells* **2010**, *10* (4), 575–581.

(6) Blizanac, B. B.; Ross, P. N.; Marković, N. M. *J. Phys. Chem. B* **2006**, *110* (10), 4735–4741.

(7) Yang, R.; Bian, W.; Strasser, P.; Toney, M. F. *J. Power Sources* **2013**, *222*, 169–176.

(8) Guo, H.; Liu, X.; Bai, C.; Chen, Y.; Wang, L.; Zheng, M.; Dong, Q.; Peng, D.-L. *ChemSusChem* **2015**, *8* (3), 486–494.

(9) Zhang, N.; Chen, X.; Lu, Y.; An, L.; Li, X.; Xia, D.; Zhang, Z.; Li, J. *Small* **2014**, n/a – n/a.

(10) Zhang, C.; Sandorf, W.; Peng, Z. *ACS Catal.* **2015**, 2296–2300.

(11) King, F.; Quinn, M. .; Litke, C. . *J. Electroanal. Chem.* **1995**, *385* (1), 45–55.

(12) Vukmirovic, M. B.; Vasiljevic, N.; Dimitrov, N.; Sieradzki, K. *J. Electrochem. Soc.* **2003**, *150* (1), B10–B15.

(13) Rajalakshmi, N.; Dhathathreyan, K. S. *Chem. Eng. J.* **2007**, *129* (1–3), 31–40.

(14) Reddington, E.; Sapienza, A.; Gurau, B.; Viswanathan, R.; Sarangapani, S.; Smotkin, E. S.; Mallouk, T. E. *Science* **1998**, *280* (5370), 1735–1737.

(15) Liu, X.; Shen, Y.; Yang, R.; Zou, S.; Ji, X.; Shi, L.; Zhang, Y.; Liu, D.; Xiao, L.; Zheng, X.; Li, S.; Fan, J.; Stucky, G. D. *Nano Lett.* **2012**, *12* (11), 5733–5739.

(16) Almeida, T. S.; Van Wassen, A. R.; VanDover, R. B.; de Andrade, A. R.; Abruña, H. D. *J. Power Sources* **2015**, *284*, 623–630.

(17) Dahn, J. R.; Trussler, S.; Hatchard, T. D.; Bonakdarpour, A.; Mueller-Neuhaus, J. R.; Hewitt, K. C.; Fleischauer, M. *Chem. Mater.* **2002**, *14* (8), 3519–3523.

(18) Gregoire, J. M.; van Dover, R. B.; Jin, J.; DiSalvo, F. J.; Abruña, H. D. *Rev. Sci. Instrum.* **2007**, *78* (7), 072212–072212 – 6.

(19) Prochaska, M.; Jin, J.; Rochefort, D.; Zhuang, L.; DiSalvo, F. J.; Abruña, H. D.; van Dover, R. B. *Rev. Sci. Instrum.* **2006**, *77* (5), 054104–054104 – 8.

(20) Cooper, J. S.; McGinn, P. J. *Appl. Surf. Sci.* **2007**, *254* (3), 662–668.

(21) Yu, J.-S.; Kim, M.-S.; Kim, J. H. *Phys. Chem. Chem. Phys.* **2010**, *12* (46), 15274.

(22) Stevens, D. A.; Rouleau, J. M.; Mar, R. E.; Bonakdarpour, A.; Atanasoski, R. T.; Schmoeckel, A. K.; Debe, M. K.; Dahn, J. R. *J. Electrochem. Soc.* **2007**, *154* (6), B566.

(23) Stöwe, K.; Dogan, C.; Welsch, F.; Maier, W. F. *Z. Für Phys. Chem.* **2013**, *227* (5), 561–593.

(24) Fernández, J. L.; Walsh, D. A.; Bard, A. J. *J. Am. Chem. Soc.* **2005**, *127* (1), 357–365.

(25) Liu, G. C.-K.; Sanderson, R. J.; Vernstrom, G.; Stevens, D. A.; Atanasoski, R. T.; Debe, M. K.; Dahn, J. R. *J. Electrochem. Soc.* **2010**, *157* (2), B207.

(26) Debe, M. K.; Schmoeckel, A. K.; Vernstrom, G. D.; Atanasoski, R. *J. Power Sources* **2006**, *161* (2), 1002–1011.

(27) Debe, M. K.; Steinbach, A. J.; Vernstrom, G. D.; Hendricks, S. M.; Kurkowski, M. J.; Atanasoski, R. T.; Kadera, P.; Stevens, D. A.; Sanderson, R. J.; Marvel, E.; others. *J. Electrochem. Soc.* **2011**, *158*, B910.

(28) Easton, E. B.; Bonakdarpour, A.; Yang, R.; Stevens, D. A.; Dahn, J. R. *J. Electrochem. Soc.* **2008**, *155* (6), B547.

(29) Lima, F. H. B.; Zhang, J.; Shao, M. H.; Sasaki, K.; Vukmirovic, M. B.; Ticianelli, E. A.; Adzic, R. R. *J. Phys. Chem. C* **2007**, *111* (1), 404–410.

(30) Zhang, J.; Yang, H.; Fang, J.; Zou, S. *Nano Lett.* **2010**, *10* (2), 638–644.

(31) Bromberg, L.; Fayette, M.; Martens, B.; Luo, Z. P.; Wang, Y.; Xu, D.; Zhang, J.; Fang, J.; Dimitrov, N. *Electrocatalysis* **2012**, *4* (1), 24–36.

(32) Cao, D.; Wieckowski, A.; Inukai, J.; Alonso-Vante, N. *J. Electrochem. Soc.* **2006**, *153* (5), A869–A874.

(33) Oezaslan, M.; Hasche, F.; Strasser, P. *J. Electrochem. Soc.* **2012**, *159* (4), B444–B454.

(34) Li, M.; Du, Z.; Guo, C.; Li, C. *CALPHAD Comput Coupling Phase Diagr. Thermochem* **2008**, *32*, 439–446.

CHAPTER 6

COMPOSITIONALLY-DEPENDENT OXYGEN REDUCTION ACTIVITY OF $PD_{1-X}CU_X$ THIN FILMS IN ALKALINE MEDIA

This work was done in collaboration with Andrés Molina-Villarino.

6.1 Abstract

Previous work by our group identified the Pd-Cu composition space as potentially promising oxygen reduction reaction (ORR) catalysts. Co-sputtering was used to deposit metal thin films of $Pd_{1-x}Cu_x$ in 10 at.% increments onto glassy carbon electrodes. X-ray diffraction showed that all compositions formed solid solutions. These electrodes were then tested electrochemically in a Teflon rotating Change-Disk electrode holder to evaluate their catalytic activity for the ORR. We found that the ratio of Pd to Cu affected the catalytic activity, with the "peak" of the activity occurring around the composition $Pd_{0.5}Cu_{0.5}$, although notably, the addition of just 10% Pd to Cu improved the E_{onset} from Cu's 0.67 V to 0.86 V, an improvement of almost 200 mV. From cost and activity perspectives, therefore, there may be multiple catalytically interesting compositions. The improved onset potential seemed to correlate with a destabilization of the CuO formed at high potentials, as it seemed that the CuO had an inhibitory effect on the oxygen reduction. XPS of the compositions also showed stabilization of the Cu metal, particularly for $Pd_{0.5}Cu_{0.5}$. After

electrochemical experimentation, the surfaces of the non-equimolar electrodes more closely matched the bulk composition.

6.2 Introduction

In an attempt to mitigate the rising levels of CO_2 in the atmosphere, which can lead to increasingly warm global temperatures, people have tried to find alternative technologies to generate electricity or energy that are more efficient and generate less CO_2. Fuel cells are one such technology, generating electricity by redox reactions. The reaction at the cathode, the oxygen reduction reaction (ORR) is known for its slow kinetics, seen as a large overpotential—typically around 300 mV or more—which lowers the efficiency of the resulting fuel cell.[1] In addition, the ORR is ideally run at high applied potentials, which will oxidize or dissolve many metals under the acidic conditions common to proton exchange membrane (PEM) fuel cells. This leaves very noble—and expensive—metals such as Pt and Au as stable ORR catalysts under acidic conditions.

As better alkaline membranes have been developed,[2–4] alkaline fuel cells have become a more viable alternative to PEM fuel cells, and as such, the amount of research on alkaline electrocatalysis systems has increased. Alkaline conditions offer some advantages, perhaps chiefly among these being the improved stability afforded by alkaline pH's.[1] Previous work in our group focused on the oxygen reduction activity of a variety of binary metal compositions under alkaline conditions, using high-throughput methods: co-sputtering thin films onto glassy carbon electrodes that

were then tested electrochemically. The best of these compositions was $Pd_{0.5}Cu_{0.5}$, and as such, we follow up that work with a more in-depth study of the oxygen reduction catalysis in the composition space of Pd-Cu.

Pd-Cu compositions have been used for many applications other than alkaline ORR, including several different types of catalysis. PdCu has been used for oxygen reduction catalysts, but under acidic conditions.[5–7] Some of these studies have involved deliberately dealloying the Cu from the surface to create a Pd-rich shell,[8] analogous to similar PtCu systems.[9] Pd-Cu systems have also been used to catalyze fuel oxidations, including formic acid,[10] ethanol,[11–13] and methanol.[14–16] Beyond fuel oxidations, Pd-Cu has been used to catalyze nitrate ion reduction,[17] in catalytic converters,[18] and as a H_2-permeable membrane.[19,20]

6.3 Experimental

6.3.1 Sputtering Chamber Setup

The thin films used in these experiments were sputtered in a custom-built sputter deposition chamber, as described by Gregoire *et al.*[21] To deposit a uniform adhesion layer, the 4 in. magnetron sputter gun (AJA, Inc.) inside the chamber was equipped with a Ti target and deposited before the catalyst film during the same pumpdown. A composition spread of metals to be used in the catalyst films was deposited by an array of three 2 in. magnetron sputter guns (Angstrom Sciences Onyx-2). Because of their 15° tilt and arrangement 120° apart from each other, they gave a composition gradient of about 1 at.% mm^{-1}.[21] Although the chamber had a fourth gun

in the center, set just below the level of the other three guns, it was not used in this work. To monitor the deposition rates of the films, a quartz crystal thickness monitor (Inficon) was used for both the 4 in. gun, and also for the 2 in. guns, and could monitor the 2 in. guns individually or together.

A special substrate holder, as previously described,[22] was used to hold the glassy carbon substrates during deposition. Only one glassy carbon substrate was deposited at a time, although the holder allowed for up to sixteen. This holder allowed for co-sputtering of the target elements without shadowing effects, with the top of the electrodes flush with the holder. The holder did not allow for substrates to be heated during deposition, however.

Before placing the glassy carbon in the chamber, it was cleaned with isopropanol to remove any alumina powder, left over from manual polishing as described below, or residual oils and dust that might have accumulated on the surface. Once the substrates were in the chamber and under vacuum, a 12 nm Ti adhesion layer was then sputtered directly on the glassy carbon at a rate of 2 Å/s. On top of that, 50 nm of catalyst layer was then deposited, with the combined sputtering rates of the metals at 4 nmol/s. Ar (5 mTorr or 0.67 Pa at 75 sccm) was used as the sputtering gas for both the adhesion and catalyst layers.

6.3.2 Electrochemistry

As each glassy carbon electrode (5 mm, Sigradur G, HTW) was used several times, previously-deposited thin films needed to be removed with each new use. It was determined that the most efficient way to remove old thin films was by mechanical

polishing. To do this, each electrode was polished with polishing papers (Buehler, p 280-2500) appropriate to the degree of roughness already present on the electrode, initially on the virgin glassy carbon to get an even surface, and then polished to a mirror finish with diamond paste and diamond paste extender (1μm particle size, Buehler, Buehler Metadi fluid) on polishing cloths **(**Buehler Microcloth**)**. To use the deposited electrodes for electrochemical testing, a piece of Teflon tape was stretched thin and wrapped around the sides of the glassy carbon. The Teflon tape provided a tight seal to prevent leaks as well as to prevent the ejection of the electrode once it was inserted into an exchangeable rotating disk electrode (RDE) tip (Pine Research Instrumentation, E4TQ series tip and holder). To maintain an oxygen atmosphere, particularly during rotation, a glass cap was placed onto the electrode shaft and the rod was then inserted into the rotator (Pine Research Instrumentation, AFMSR series). The cap then fit into the top of the electrochemical cell, which was a custom-built three-neck electrochemical cell designed specifically for RDE experiments, which was used for all experiments. Pt mesh was used as a high-surface-area counter electrode along with a home-built Ag/AgCl reference electrode with a bipotentiostat (Pine Research Instrumentation, AFRDE5).

For electrochemical testing, NaOH solution (0.1 M, Malinckrodt AR) was used as the electrolyte. Before the oxygen reduction reaction experiment, to electrochemically clean the catalyst film, the cell and electrolyte solution were deoxygenated with N_2 (Airgas, high purity) for 15 minutes. A window-opening cyclic voltammogram (CV) was performed first, in which the negative stable potential was initially determined, followed by the positive potential, and subsequently the electrode

was cycled between those two potentials at 50 mV/s until the CV remained constant. The N_2 was then exchanged for O_2 (Airgas, ultra-high purity) for 15 minutes until the first rotation rate. Electrochemical cycling continued during oxygenation, and during each 7-minute O_2 purge between each rotation rate. Rotating disk experiments were performed using rotation rates between 50-2000 rpm and a scan rate of 20 mV/s.

To analyze the data collected in the rotating disk experiments, the Levich equation was used, particularly to determine the number of electrons involved in the reaction. The D_O for O_2 was taken to be 1.93×10^{-5} cm^2s^{-1}, and the value for its concentration was 1.25 mM. These values were determined by doing an oxygen reduction rotating disk experiment on bulk Pd, which gives a value of n = 4. Pd is known to reduce O_2 through the direct (4-e^- process) mechanism in alkaline media.[23] To perform Levich analysis, the potentials used were ones where the current reached the mass-transport limit.

6.3.3 X-Ray Diffraction

Although X-Ray diffraction (XRD) on the sputtered glassy carbon electrodes has been used in previous work, because of overlap with glassy carbon peaks **(**Fig. 6.1), neither Cu nor Pd peaks could be seen on the electrodes used for electrochemical analysis. A Si wafer (3" diameter, (100) p-doped, University Wafers) was sputtered with a 12 nm-thick Ti adhesion layer, and a 50 nm catalyst layer was deposited, just as described in the above section. With a 1 at.%/mm composition gradient, compositions were sampled every 1 cm, to mimic the discrete 10 at% increments at which the glassy carbon electrodes were deposited. Two other wafers allowed for determination at

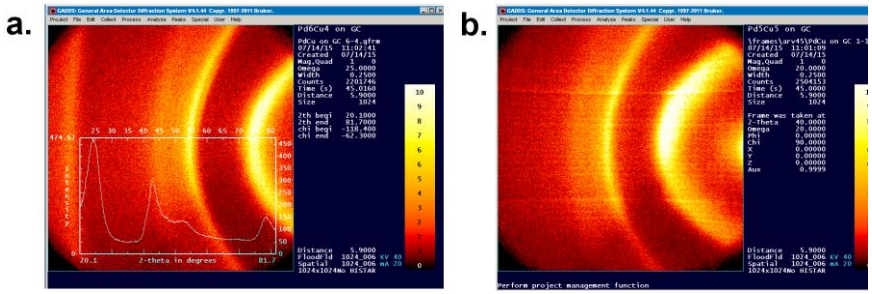

Figure 6.1. The 2D XRD patterns for a.) $Pd_{0.6}Cu_{0.4}$, shown with the integrated pattern, and b). $Pd_{0.5}Cu_{0.5}$. Peaks and rings seen were due to glassy carbon.

higher and lower at.% of Pd, as the wafer was not large enough to accommodate the entire composition range. A Rigaku SmartLab X-Ray Diffractometer was used to perform diffraction on the Si wafers. Initial 2D XRD was done using a Bruker General Area Detector Diffraction System (GADDS).

6.3.4 XPS

X-ray photoelectron spectroscopy (XPS) was used to ascertain surface compositions at the centers of each tested film on the glassy carbon electrode. Survey scans were acquired between 1100 and 0 eV under high vacuum (2×10^{-9} Torr) using an Al-Kα X-ray source. High resolution scans were measured only for Cu, over the energy range of 910 to 972 eV. Spectra were analyzed using CASA XPS software. The "before" measurements were performed before electrochemical testing, after storing the electrodes in air, and the "after" measurements were performed after electrochemically cycling for approximately 3 hours.

6.4 Results and Discussion

6.4.1 XRD

As mentioned in the Experimental section, XRD was performed on sputter-deposited Si wafers instead of the glassy carbon electrodes. Although glassy carbon was expected to be amorphous, we still saw clear, broad, and intense peaks at 24.5°, 42°, 53°, and 80° (see Fig. 6.1), which overlap with the (111) peaks of Cu and Pd. Even with a thicker metal film (300 nm or a factor of 6), the diffraction pattern changed very little, with just a very noisy shoulder on the edge of the glassy carbon peaks. We had to take into account, however, the presence of a Ti adhesion layer. Depositing fcc metals on a tetragonal Si lattice may have strained the crystal lattice, or it may have led to texturing in the films. However, with hcp Ti as the adhesion layer in both cases, the local environment was preserved between samples, and the surface for the catalyst deposition was therefore assumed to be consistent between the glassy carbon and Si samples, hopefully leading to the same structure in both cases.

XRD data (Fig. 6.2) showed that despite the ambient temperature deposition conditions, the films were still crystalline, which was unsurprising for metal thin films comprised of materials that all individually have an fcc structure. Three separate Pd-

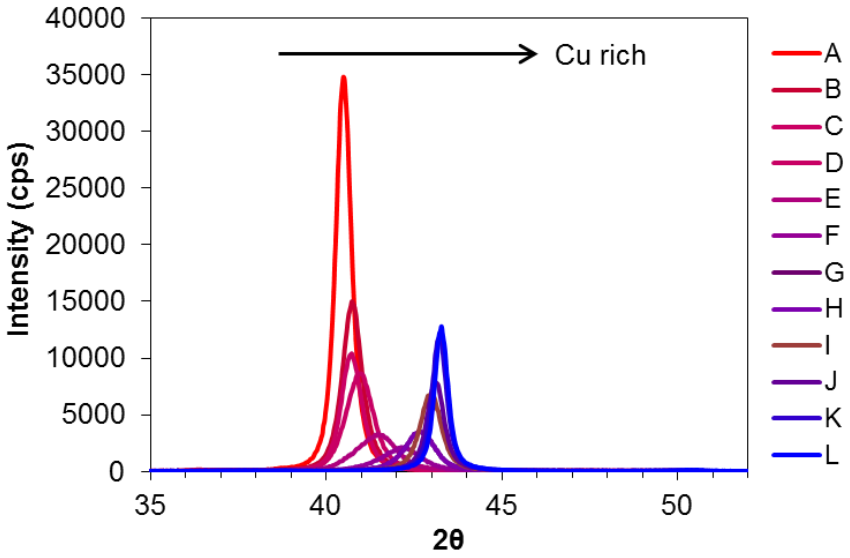

Figure 6.2. Grazing incidence XRD of $Pd_{1-x}Cu_x$ compositions. XRD was performed on three 3" Si wafers, deposited with compositions of $Pd_{0.5}Cu_{0.5}$, $Pd_{0.7}Cu_{0.3}$, $Pd_{0.3}Cu_{0.7}$ as the targeted composition.

Cu films were used to cover the entirety of the composition space, with different target compositions at the center ($Pd_{0.7}Cu_{0.3}$, $Pd_{0.5}Cu_{0.5}$, and $Pd_{0.3}Cu_{0.7}$). The films were a solid solution over the entire composition space, with the (111) peak shifting from the Pd peak at 40.15° to the Cu peak at 43.35°.[24] However, both the very Cu- and Pd-rich compositions were about 0.2° off from the single metal peak, most likely due to a small percentage of the less concentrated element at those locations on the wafer. The phase diagram for Cu-Pd is complicated, with several different ordered phases formed at relatively low temperatures, (most occupying non-fcc structures) and solid structure

forming at high temperature.[25] While the thin films may not have followed the low-temperature portion of the phase diagram to produce the various ordered phases, the alloys they formed should still be able to be generated as nanoparticles using a high-temperature quench. As such, this was determined to be a viable system for oxygen reduction catalysis.

6.4.2 Oxygen Reduction Activity

The ability to rapidly probe an entire composition space was, undoubtedly, one of the main strengths of this approach. We were able to evaluate the electrochemical and catalytic behavior of nine different Pd-Cu compositions in an effort to determine which one exhibited the optimal catalytic behavior. The optimal electrocatalytic behavior can be defined or identified in different ways. First, one could employ the onset potential, defined in this work as the potential where 10% of the i_l current is reached. Fig. 6.3 shows the onset potential for Pd_xCu_{1-x} compositions, where $0 \leq x \leq 1$. The rotation rate used for this figure was 350 rpm, because which was an intermediate rotation rate between 50 and 2000 rpm.

Fig. 6.3 presents the catalytic activity (in terms of E_{onset}) as a function of the amount of Pd in the Cu-Pd binary film. Cu metal, while capable of reducing oxygen, did not do so efficiently, requiring a large, 500 mV, overpotential. Of all the compositions in this study, Cu performed the worst, when evaluated with respect to its E_{onset}. Figure 6.3 exhibited a small peak in $E_{onset,}$ between 40-60% Pd. The best single-

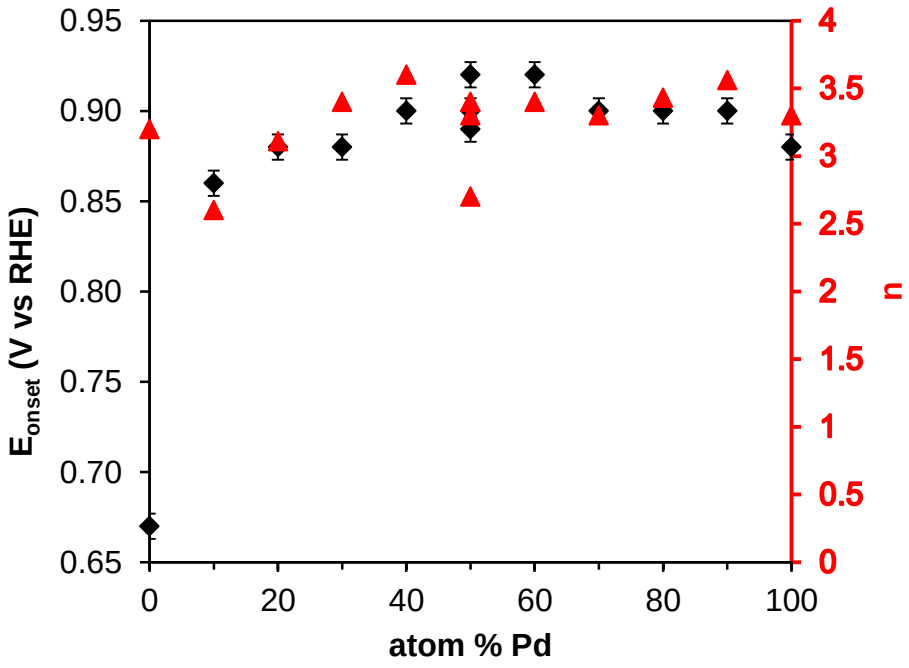

Figure 6.3. The variation in E_{onset} as a function of Pd content. Each point was measured where ω = 350 rpm, ν = 20 mV/s, 0.1 M NaOH. Error bars come from repeat experiments conducted on $Pd_{0.5}Cu_{0.5}$.

trial compositions were $Pd_{0.5}Cu_{0.5}$ and $Pd_{0.6}Cu_{0.4}$. However, repeated experiments on $Pd_{0.5}Cu_{0.5}$ showed that there was some variance in the data, as subsequent samples (freshly sputtered) did not show an activity that was quite as good, although it was still comparable (~30 mV). The variance in the data was small (7 mV), and from those three repeated experiments, the results were applied to the rest of the compositions.

A second way to evaluate electrocatalytic performance was based on the mechanism of the reaction, in terms of the number of electrons involved in the reaction (n), as calculated from the Levich equation. In an ideal system, n should be 4, indicating that the reaction proceeds entirely through the direct, or 4-e^- mechanism, which, under alkaline conditions, yilds OH^- . The 2-e^- mechanism involves the generation of the oxidizing HO_2^- . Because of the effects of wrapping the electrodes with Teflon tape described in the Experimental section, the exact geometric surface area exposed to the solution (and therefore involved in the electrochemistry) was not precisely known, as it was different in each case. Therefore, we can only look for broad trends in the data.

With two exceptions, all of the electron counts fell between 3-3.6, which was consistent with the behavior of the parent metal thin films, which both perform 4-e^- reductions. The parent thin films had a 15-20% less current than those same metals in bulk (the binary thin films also showed these lower currents). These lower currents were consistent with about a 15-20% decrease in the surface area of the electrode, which was borne out by control experiments that we carried out with $K_3Fe(CN)_6$. $K_3Fe(CN)_6$ has a well-known D_O, an easily-controlled concentration, and a known n-value, which allowed us to precisely calculate the geometric area of the electrode, unlike the ORR experiments, where these parameters are not precisely known. These experiments gave a variety of coverages from 18-27% of the electrode covered by tape. The two outliers, $Pd_{0.1}Cu_{0.9}$ and one of the trials of $Pd_{0.5}Cu_{0.5}$ would be consistent with about 27% of the electrode being covered by Teflon tape. Although this seems high, in relation to the others, considering the more normal electron counts of the other

two $Pd_{0.5}Cu_{0.5}$, this seemed to be the likeliest situation, in addition to the control experiment that did have higher Teflon tape coverage than the other two trials (Table 6.1).

Table 6.1. Average area loss by Teflon tape coverage for three different RDE $K_3Fe(CN)_6$ experiments.

Trial Number	Area Loss (average)
1	18.1
2	18.5
3	27.2

A third way to evaluate the best catalyst was average cost. Clearly, as the Pd content in the catalysts increased, so did the cost. Hence this did not correspond to a linear increase in the catalytic activity, as one would expect if Pd were the sole contributor to the activity of the binary catalyst. For the broad "peak" of activity, at 40-60% Pd, the best catlyst would be the most Cu-rich, as the cost of Cu is negligible when compared to Pd or even most other platinum group metals, including Ag.

Aside from the "peak", though, there was a second interesting composition in Figure 6.3. Notably, when cost was considered, the most Cu-rich composition ($Pd_{0.1}Cu_{0.9}$) became more interesting than it would otherwise appear. By adding just 10% Pd to Cu, there was an improvement in the E_{onset} of about 200 mV. While this behavior was not as favorable as any of the other Pd-Cu compositions, but it was only 20 mV less than pure Pdwith respect to its E_{onset}, at essentially 10% of the cost. Although this composition ,may not be useful for all applications, such as those where space, rather than cost, is the most critical factor, it might be attractive for stationary

power generation, where the fuel cell stack is not as spatially limited.

6.4.3 Cyclic Voltammetry

The cyclic voltammetric responses of the different Pd-Cu compositions varied

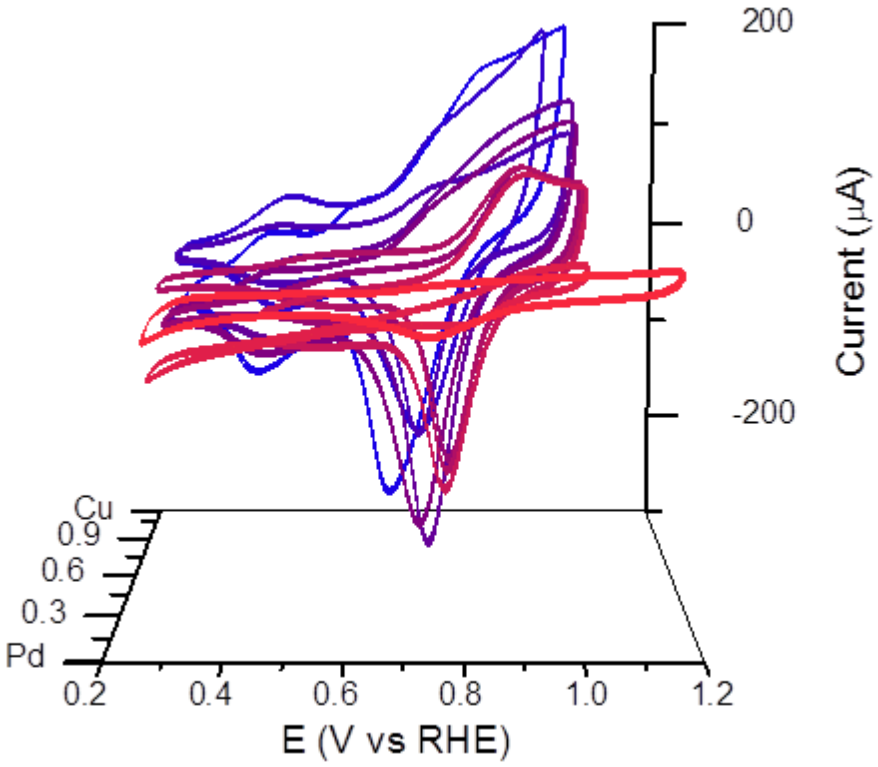

Figure 6.4. The cyclic voltammetry for each thin film composition studied, including the CV of Pd and Cu films. ν = 50 mV/s, 0.1 M NaOH

as the ratios of the two elements varied, as shown in Figure 6.4. As the amount of Cu in the composition increased, the current passed increased, perhaps due to higher electrochemical surface area. This larger electrochemical surface area (ECSA) did not translate, however, to a correspondingly higher current in the RDE. This demonstrates

that the increased current in the CV's, but not in the RDE, was due to ECSA differences.

Beyond just surface area differences, however, we did see shifts in the redox peaks. The Cu CV had an irreversible oxidation, with only a very small oxide reduction peak relative to the oxide formation peak. The CV of a bulk Cu copper electrode (Fig. 6.5) was more reversible than the thin film, at least with respect to the oxidation and reduction currents, even though the peak separation does not show

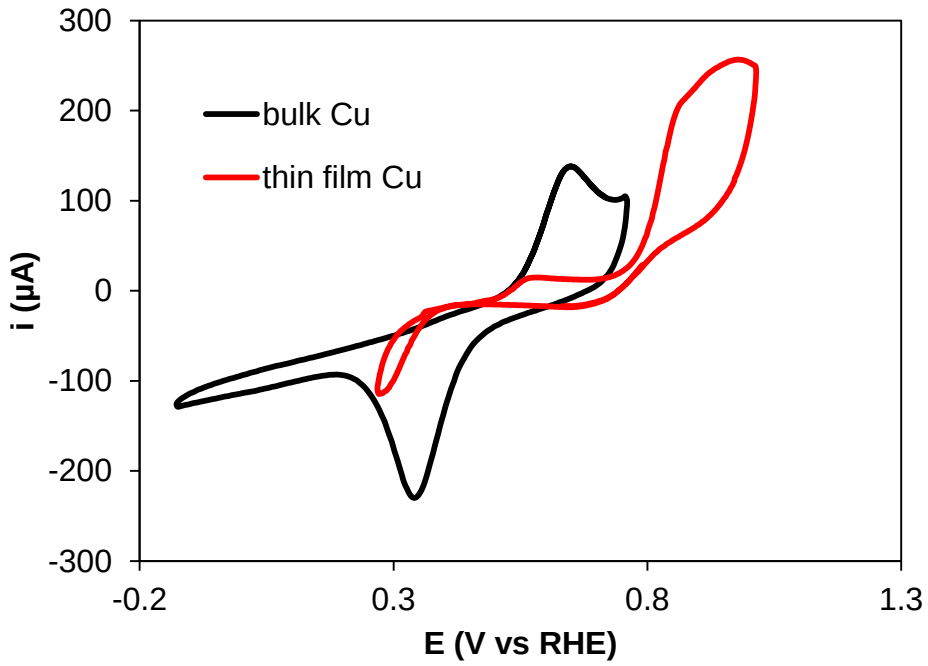

Figure 6.5. The CV of bulk Cu and thin film Cu in 0.1 M NaOH. ν = 100 mV/s for bulk, 50 mV/s for thin film.

electrochemical reversibility. The thin film electrode was also taken to more oxidizing potentials, which may account for its increased irreversibility. The surface area of the thin film electrode appeared to be much larger than the bulk electrode, since when the

current was integrated over the same potential region of each CV (Fig. 6.5), the charge was about double (-6.0 mC) that of the bulk (-3.2 mC), again indicating that the Cu films were likely rougher. The extended positive potential range used in Fig.6.4 for the thin film, relative to the bulk, was so as to allow a to more ready comparison to the other $Pd_{1-x}Cu_x$ CVs. The other Cu-rich binary compositions also showed similar Cu

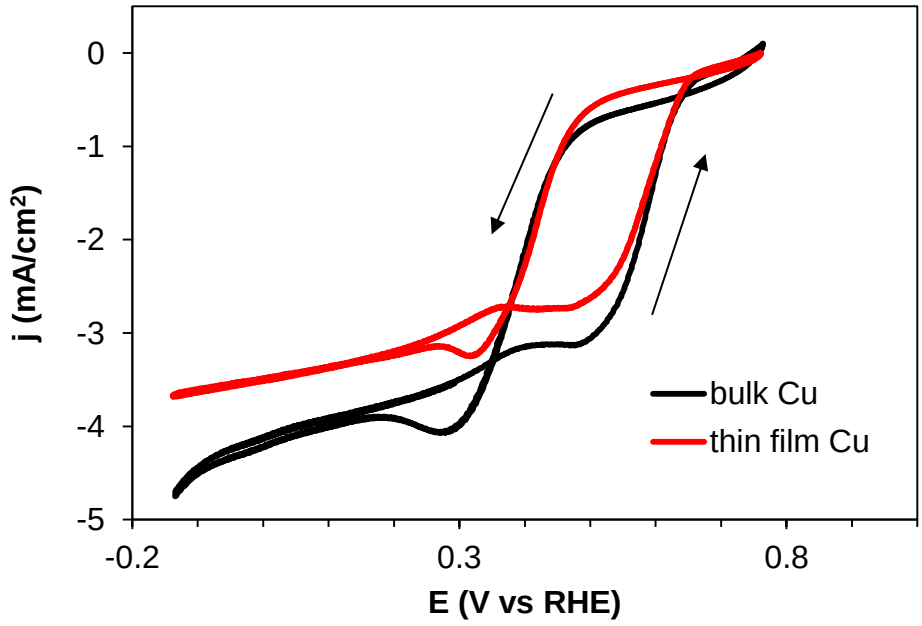

Figure 6.6. RDE voltammograms for bulk and thin film Cu. ν = 20 mV/s, ω = 150 rpm, 0.1 M NaOH.

oxidation peaks, which did not increase in current over the course of electrochemical cleaning and cycling, indicating that the surface area was not necessarily increasing as the potential was cycled.

A notable difference between the Cu-rich compositions and the Cu film was the Cu reduction peak. Even the binary compositions with 80-90% Cu had much larger CuO reduction peaks, suggesting that the CuO under these conditions may have

been destabilized relative to Cu metal because of the addition of small amounts of Pd. The shift in the ORR E_{onset} could be correlated with the E_{onset} for oxide reduction. It may be possible that this relationship correlated with the increase in catalytic activity that we saw with the addition of just 10% Pd. This was consistent with the ORR behavior of both bulk and thin film Cu, which, in each case, exhibited hysteresis between the positive- and negative-sweeping scans, shown in Fig. 6.6, with the positive-sweep showing a considerably improved E_{onset} due to the reduced Cu surface. This may be similar to some work on Pt binaries showing that the improvement in the E_{onset} of the binaries (such as Pt_3Ni) may be attributed to inhibition of Pt-OH_{ads} formation, which can block the more active free Pt sites.[26,27]

6.4.4 XPS

With any of these compositions, but particularly with the Cu-rich ones, durability and ageing of the catalyst were particularly important. Traditionally, when Cu has been used for ORR catalysts under acidic conditions, it has been used as a comparatively inexpensive sacrificial element,[8,28] because, according to its Pourbaix diagram, under low pH conditions, essentially any applied oxidizing potential will cause the Cu to dissolve.[29] Under alkaline conditions, however, the same Pourbaix diagram showed a different story. At pH 13, the conditions used in this experiment, and for potentials, from 0 to approximately 0.5 V vs RHE, Cu exists as a neutral species. At higher applied potentials, instead of dissolving to Cu^{2+}, it is first oxidized to Cu_2O and then CuO. At sufficiently positive potentials, at pH 13 (E > 0.75 V vs RHE), very small concentrations of $HCuO_2^-$ would probably be generated, according

to the Pourbaix diagram. The oxidation to $HCuO_2^-$ may be kinetically limited, however, resulting in limited generation.

Although the thin films used in these experiments were not ideal to assess catalyst durability, we were able to draw some conclusions about it using XPS. We performed XPS measurements on three different $Pd_{1-x}Cu_x$ compositions: $Pd_{0.9}Cu_{0.1}$, $Pd_{0.5}Cu_{0.5}$, and $Pd_{0.1}Cu_{0.9}$ and recorded their measured elemental ratios before and after electrochemical cycling (Table 6.2). The oxidation state of the Cu in these

Table 6.2. Surface compositions of thin films, as measured by XPS.

	$Pd_{0.9}Cu_{0.1}$	**$Pd_{0.1}Cu_{0.9}$**	**$Pd_{0.5}Cu_{0.5}$**
Before	74% Pd, 26%Cu 37% Cu^0, 63 % Cu^{II}	27 % Pd, 73 % Cu 58 % Cu^0, 42 % Cu^{II}	56 % Pd, 44 % Cu 64% Cu^0, 36% Cu^{II}
After	92% Pd, 8% Cu 62% Cu^0, 38% Cu^{II}	7% Pd, 93% Cu 15% Cu^0, 85% Cu^{II}	15% Pd, 85% Cu 88% Cu^0, 12% Cu^{II}

compositions was also measured using high-resolution XPS. Initially, the ratio of Pd to Cu for the equimolar composition was fairly close to the intended composition, although after electrochemical cycling the surface became considerably enriched in Cu, contrary to our expectations that the Cu would dissolve somewhat. Cu does have a higher mobility than Pd, however, so it was perhaps not surprising that Cu moved to the surface. Notably, when compared to the other compositions tested, the Cu both before and after electrochemical cycling had a greater ratio of reduced Cu^0 than Cu^{II}, consistent with the CV data that showed that the addition of Pd stabilized the Cu metal, and that CuO was a poison to ORR activity.

The high and low Pd compositions showed slightly different results. Instead of the initial composition aligning closely with the target composition, they were each off by about 20%. These two samples had been sitting for a few months after deposition before their initial XPS data were recorded, so there may have been appreciable diffusion in the films during that time. There is also literature precedent for the formation of these compositions at surfaces, as well. This was particularly true in the case of the intended $Pd_{0.1}Cu_{0.9}$, which has been reported to form different surface structures and compositions than those in the bulk, notably the composition $PdCu_3$, which roughly matches the stoichiometry of the $Pd_{0.1}Cu_{0.9}$ composition.[30–32] Although initial compositions of the films differed from the targeted composition significantly, after electrochemical experimentation, they shifted much closer to the original intended composition, within a few percent, showing that the initial surface composition did not afford any special electrochemical stability. The most Cu-rich composition did have the most oxidized Cu (which was also the only composition to increase its proportion of oxidized Cu after electrochemical cycling), and the most Pd-rich was intermediate between the equimolar and the Cu-rich, also similar to the ORR activity, where the most Pd-rich material did not have the highest E_{onset}.

6.5 Conclusion

From previous work in our group, we identified that Pd-Cu was a promising oxygen reduction (ORR) catalyst selected from many combinations of platinum group metals. In order to screen the catalyst compositions more efficiently, we co-sputtered

metal thin films with the composition of $Pd_{1-x}Cu_x$ in 10 at.% increments onto glassy carbon electrodes with Ti adhesion layers. All nine compositions with different stoichiometries were shown to be solid solutions using grazing-incidence XRD. The oxygen reduction activities of the sputtered electrodes were evaluated electrochemically in a Teflon Change-Disk electrode, and we found that composition affected the catalytic activity, leading to a "peak" in the E_{onset} at a composition of $Pd_{0.5}Cu_{0.5.}$ Also notable was the fact that the addition of 10% Pd to Cu decreased the overpotential of a pure Cu film by around 200 mV. The improvement in the E_{onset} could be attributed to an improvement in the stability of reduced Cu in the alloy, relative to a pure Cu film, as seen in the cyclic voltammetry profile. XPS did not show that appreciable amounts of Cu dissolved over the course of the experiments, with even the $Pd_{0.5}Cu_{0.5}$ surface becoming enriched in Cu after cycling. Similar to the CV data, the XPS also showed stabilization of the Cu metal for this composition. After electrochemical experimentation, the surfaces of the non-equimolar electrodes more closely matched the bulk composition.

6.6 Acknowledgements

This work made use of the Cornell Center for Materials Research Shared Facilities which are supported through the NSF MRSEC program (DMR-1120296). James Pastore assisted with the generation of Figure 6.4. Jonathan Shu assisted with the XPS. Funding for A. R. Van Wassen was provided through by NYSTAR.

6.7 References

(1) Spendelow, J. S.; Wieckowski, A. *Phys. Chem. Chem. Phys.* **2007**, *9* (21), 2654.

(2) Kostalik, H. A.; Clark, T. J.; Robertson, N. J.; Mutolo, P. F.; Longo, J. M.; Abruña, H. D.; Coates, G. W. *Macromolecules* **2010**, *43* (17), 7147–7150.

(3) Noonan, K. J. T.; Hugar, K. M.; Kostalik, H. A.; Lobkovsky, E. B.; Abruña, H. D.; Coates, G. W. *J. Am. Chem. Soc.* **2012**, *134* (44), 18161–18164.

(4) Hugar, K. M.; Kostalik, H. A.; Coates, G. W. *J. Am. Chem. Soc.* **2015**, *137* (27), 8730–8737.

(5) Fouda-Onana, F.; Bah, S.; Savadogo, O. *J. Electroanal. Chem.* **2009**, *636* (1–2), 1–9.

(6) Kariuki, N. N.; Wang, X.; Mawdsley, J. R.; Ferrandon, M. S.; Niyogi, S. G.; Vaughey, J. T.; Myers, D. J. *Chem. Mater.* **2010**, *22* (14), 4144–4152.

(7) Shao, M.; Liu, P.; Zhang, J.; Adzic, R. *J. Phys. Chem. B* **2007**, *111* (24), 6772–6775.

(8) Yang, R.; Bian, W.; Strasser, P.; Toney, M. F. *J. Power Sources* **2013**, *222*, 169–176.

(9) Oezaslan, M.; Hasche, F.; Strasser, P. *J. Electrochem. Soc.* **2012**, *159* (4), B394–B405.

(10) Wu, D.; Dai, C.; Li, S.; Cheng, D. *Chem. Lett.* **2015**, *44* (8), 1101–1103.

(11) Hu, C.; Zhai, X.; Zhao, Y.; Bian, K.; Zhang, J.; Qu, L.; Zhang, H.; Luo, H. *Nanoscale* **2014**, *6* (5), 2768–2775.

(12) Cai, J.; Zeng, Y.; Guo, Y. *J. Power Sources* **2014**, *270*, 257–261.

(13) Carrera-Cerritos, R.; Fuentes-Ramírez, R.; Cuevas-Muñiz, F. M.; Ledesma-García, J.; Arriaga, L. G. *J. Power Sources*.

(14) Wang, R.; Zhang, Z.; Wang, H.; Lei, Z. *Electrochem. Commun.* **2009**, *11* (5), 1089–1091.

(15) Wang, R.; Li, H.; Feng, H.; Wang, H.; Lei, Z. *J. Power Sources* **2010**, *195* (4), 1099–1102.

(16) Wang, H.; Wang, R.; Li, H.; Wang, Q.; Kang, J.; Lei, Z. *Int. J. Hydrog. Energy* **2011**, *36* (1), 839–848.

(17) Anastasopoulos, A.; Hannah, L.; Hayden, B. E. *J. Catal.* **2013**, *305*, 27–35.

(18) A, H. J. D.; W, L. F.; E, S. R. Supported copper oxide and palladium catalyst composition. US3224981 A, December 21, 1965.

(19) Yuan, L.; Goldbach, A.; Xu, H. *J. Phys. Chem. B* **2007**, *111* (37), 10952–10958.

(20) Decaux, C.; Ngameni, R.; Solas, D.; Grigoriev, S.; Millet, P. *Int. J. Hydrog. Energy* **2010**, *35* (10), 4883–4892.

(21) Gregoire, J. M.; van Dover, R. B.; Jin, J.; DiSalvo, F. J.; Abruña, H. D. *Rev. Sci. Instrum.* **2007**, *78* (7), 072212–072212 – 6.

(22) Van Wassen, A. R.; Murphy, M. J.; Mollina-Villarino, A.; van Dover, R. B.; Abruña, H. D. .

(23) Lima, F. H. B.; Zhang, J.; Shao, M. H.; Sasaki, K.; Vukmirovic, M. B.; Ticianelli, E. A.; Adzic, R. R. *J. Phys. Chem. C* **2007**, *111* (1), 404–410.

(24) Swanson, H. National Bureau of Standards, 1953; Vol. 539, pp 1–95.

(25) Li, M.; Du, Z.; Guo, C.; Li, C. *CALPHAD Comput Coupling Phase Diagr. Thermochem* **2008**, *32*, 439–446.

(26) Stamenković, V.; Schmidt, T. J.; Ross, P. N.; Marković, N. M. *J. Electroanal. Chem.* **2003**, *554–555*, 191–199.

(27) Stamenković, V.; Schmidt, T. J.; Ross, P. N.; Marković, N. M. *J. Phys. Chem. B* **2002**, *106* (46), 11970–11979.

(28) Wang, D.; Yu, Y.; Xin, H. L.; Hovden, R.; Ercius, P.; Mundy, J. A.; Chen, H.; Richard, J. H.; Muller, D. A.; DiSalvo, F. J.; Abruña, H. D. *Nano Lett.* **2012**, *12* (10), 5230–5238.

(29) Pourbaix, M. *Atlas of Electrochemical Equilibria in Aqueous Solutions*, 2nd ed.; National Association of Corrosion Engineers: Houston, Texas, 1974.

(30) Priyadarshini, D.; Kondratyuk, P.; Picard, Y. N.; Morreale, B. D.; Gellman, A. J.; Miller, J. B. *J. Phys. Chem. C* **2011**, *115* (20), 10155–10163.

(31) Bardi, U. *Rep Prog Phys* **1994**, *57*, 939–987.

(32) Løvvik, O. M. *Surf. Sci.* **2005**, *583* (1), 100–106.

CHAPTER 7

FUTURE DIRECTIONS

Although I believe that all of the projects presented in the previous chapters have reached a logical conclusion, I do believe that there are some different or new directions that future students could take them. Some are entirely new directions or materials, using similar techniques or ideas, and some are exploring a material presented in my thesis in greater depth.

7.1 Future Directions for the Nitride Project

7.1.1 Future Directions for the Ta-Ti-Al-N System

As the work in Chapter 3 showed, the Ta-Ti-Al-N composition spread has good stability under acidic conditions, although none of the compositions tested showed any co-catalytic activity, the good stability still makes this an interesting system for catalyst supports.

As a thin film, however, despite 3M's nanostructured thin film, it is unlikely to be used in its current form. Nanoparticles, therefore, are the next logical direction for this project, in particular, Ti-rich compositions. Ryo Wakabayashi has actually continued this work, and these results can be found in his publications and his dissertation. Otherwise, this portion of the project on Ta-Ti-Al-N has reached its conclusion.

7.1.2 Future Directions for Other Nitride Compositions

Although most of the nitride composition spreads that we tested had modest electrochemical (and electrical conductivity) properties, one of the composition libraries—Cr-Ti-Nb-N—had good conductivity as measured by cp-AFM, and had stable electrochemical behavior. In particular, the Cr- and Ti- rich regions exhibited superior electrochemical stability. If we were to continue this project, or to return to it in the future, these would be good systems to study. A new, similar composition could be made with a greater proportion of Cr and Ti in the center of the wafer. An attractive option would be to make these materials as nanoparticles, directly, or explore them as thin films. From Ryo Wakabayashi's nanoparticle electrochemistry data, there was good agreement between the electrochemical behavior of the thin films and the nanoparticles.

If new compositions are desired, the focus should be on Ti-rich compositions. Cr also seems to aid with conductivity and electrochemical stability. Nb and Al, on the other hand, seemed to be more detrimental than beneficial.

7.2 Future Directions for the Oxygen Reduction Project

7.2.1 Additional Metals of Interest for Future ORR Catalysts

Although non-noble transition metals have been used in ORR catalysts before, they are often used as elements that will leach out easily and leave behind the more-

noble metal. Under alkaline conditions, again, they typically have much better stability, as discussed in previous chapters. It is my opinion that there are numerous transition metals that have been traditionally disregarded by electrochemists for these applications because they were assumed to be inactive and/or unstable. Going to alkaline conditions change that. Fe, in particular, has been overlooked by the ORR community, but has been reported to exhibit ORR activity.[1,2] This has also been seen—controversially—by researchers who have looked for metal contamination in allegedly active graphene ORR catalysts.[3] These materials often involve Fe, or Cu, somewhere in their synthesis, but researchers typically do not do any type of elemental analysis, such as XPS, to search for these metals.

I would have liked to sputter Fe in my binary systems, but using DC magnetron sputtering to deposit Fe is difficult. Fe-containing nanoparticles, therefore, may be a more sensible choice for nanoparticles. I also did not explore the more traditional system, Ni, in very much depth because initial data showed that Ni had no rotation-rate dependent ORR current.

7.2.2 Continuation of the Pd-Cu Work

The $Pd_{1-x}Cu_x$ work was probably the most promising system that I identified and studied in my graduate career. It was the "best" catalyst that I identified in my work, with many interesting compositions within the composition space for potentially varied applications. As a result, then, and similar to the nitride work, I believe that the next logical steps would be to make nanoparticles of some of these compositions,

focusing, in particular, on $Pd_{0.5}Cu_{0.5}$ because of its superior catalytic activity, but also on $Pd_{0.1}Cu_{0.9}$. Its activity may be less than that of the best $Pd_{1-x}Cu_x$ in the composition space, but it is also about 10% of the cost of pure Pd, and about 20% of the cost of $Pd_{0.5}Cu_{0.5}$. In fact, Mr. Yao Yan has imitated such studies.

One of the key questions to be considered for future work on this project is the importance of the specific phase prepared, especially for nanoparticles. All of the phases that I sputtered were shown to be alloy cubic phases with the same structure as both fcc Pd and Cu. There are several ordered phases in the bulk phase diagrams, as mentioned in Chapter 6. Most of these phases have different structures that are not even cubic. Whether the structure and phase are key aspects for catalytic activity was not a research question that was (or could be) explored by my thin film system, however if they were of interest, they could be explored with nanoparticles.

We also would benefit from the confirmation that the nanoparticles have comparable electrocatalytic activity to the thin films. Stability of these particles and their performance in a fuel cell (for example will they have the same problems with oxidation of the carbon black catalyst supports as Pt catalysts) will also be helpful. This project has numerous potential directions that can be explored and which have not even been mentioned here.

7.3 Future Directions for Other Combinatorial Fuel Cell Projects

When I began graduate school in 2011, good alkaline exchange membranes were relatively new, and so the field for alkaline catalysts for AEMFC was relatively

new. Alkaline ORR catalysts, in particular, were the focus of a great deal of this work because in PEMFC, the ORR is far more inefficient than the hydrogen oxidation reaction. As AEMFCs have become more viable, though, the field of alkaline ORR has become more crowded.

Anode catalysts, be they for the hydrogen oxidation reaction or methanol or another fuel, however, have remained relatively unexplored. I believe that the use of Tubby, or more generally, combinatorial techniques or sputtering, will be an efficient and attractive way to screen for new catalysts. Fuel oxidation does not necessarily require hydrodynamic methods like RDE to assess their catalysis. Because of this the "Mini-Cell" could be used to more quickly assess full composition spreads rather than with discrete electrodes. The experiments would also be less time-consuming than doing the full complement of rotation rates. As for materials to use in them, that can be determined by future graduate students, but as with the rest of my work, I advocate for looking at materials without Pt (or comparably expensive elements like Ir or Rh). I believe that this will help to differentiate their work from the rest of the field, but also is a great way to take full advantage of the combinatorial methods.

7.4 References

(1) Jovancicevic, V.; Bockris, J. O. *J. Electrochem. Soc.* **1986**, *133* (9), 1797–1807.

(2) Miller, H. A.; Bevilacqua, M.; Filippi, J.; Lavacchi, A.; Marchionni, A.; Marelli, M.; Moneti, S.; Oberhauser, W.; Vesselli, E.; Innocenti, M.; Vizza, F. *J. Mater. Chem. A* **2013**, *1* (42), 13337–13347.

(3) Wang, L.; Ambrosi, A.; Pumera, M. *Angew. Chem. Int. Ed.* **2013**, *52* (51), 13818–13821.